Dielectric Spectroscopy Studies of Low-Disorder and Low-Dimensional Materials

Thesis submitted by

Pragya Tripathi

Supervisors:

Dr. Roberto Macovez

Prof. Dr. Josep Lluis Tamarit Mur

Group of Characterization of Materials

Barcelona September, 2016

PhD Programme in Computational and applied Physics

Departament de Física

UNIVERSITAT POLITÈCNICA
DE CATALUNYA
BARCELONATECH

Problems are not stop signs,

They are guide lines

Robert H. Schuller

ABSTRACT

In this thesis we employ dielectric spectroscopy (in different implementations) to study the dielectric properties of different materials ranging from completely disordered supercooled liquids to low-disorder solids with only ratcheting reorientational motions, to low-dimensional systems such as thin films or needle-like crystals. The probed material properties include the electrical conductivity, the space-charge processes due to sample heterogeneities, molecular dynamics, hydrogen-bond dynamics, and phase-transition temperature and kinetics. To study materials in thin film form, we implement silicon-based interdigital electrode devices, which we calibrate to obtain their equivalent capacity in vacuum. We also probe two-dimensional samples obtained by intercalating (sandwiching) organic molecules between parallel graphite oxide sheets.

We study both organic and hybrid (organic-inorganic) films, and compared the results with the bulk counterpart of the same materials. Rhodamine films are deposited by two different procedures starting from rhodamine 6G chloride: solution-deposited films are ionic and ordered, while vacuum-deposited films consist of a different, neutral species, namely rhodamine19, due to decomposition of rhodamine 6G upon sublimation. Both types of films display variable-range hopping electronic conduction, and a conductivity-induced space-charge relaxation. Solution deposited films display a dipolar relaxation, absent in rhodamine 19 films. We assign the dipolar relaxation to some intramolecular motion involving the charged nitrogen of the Rhodamine and the chlorine counter-ion. We also performed studies on hybrid films of cadmium iodide covalently attached to ethylamine (CdI_2EA), deposited by the Langmuir-Blodgett process. Bulk CdI_2EA material has a solid-to-solid (structural) phase transition, which in the Langmuir-Blodgett films occurs 5 degrees higher in temperature. The films displayed a dielectric relaxation dynamics absent in the bulk, and which is either due to the existence of

molecular motions in the looser structure of the film, or to the motion of teh surfactant covalently attached to CdI_2EA for Langmuir-Blodgett film deposition.

Another example of low-dimensional material is biclotymol, whose supercooled liquid form crystallizes into a metastable solid phase which consists of one-dimensional needle-like crystallites. The crystallization kinetics of bicotymol is a textbook example of the Avrami law with exponent $n = 2$ resulting from a temperature independent nucleation rate of the crystallites followed by unidimensional growth. The instability of the supercooled liquid phase may be related to the existence of fast secondary relaxation dynamics.

The last two chapters of the thesis focus on ethane derivatives with distinct side groups, namely tetrachloroethane and ethanolamine. The solid phase of tetrachloroethane displays three distinct relaxation processes. We carry out molecular dynamic simulations to identify the three processes: the slowest is a cooperative reorientational dynamics whereby the molecules rotate by passing through an intermediate equivalent state; such collective relaxation is accompanied by a “precursor” single-molecule relaxation. The third process is a non-cooperative ratcheting motion between the equilibrium orientation and a high-energy orientation.

In ethanolamine we observe the existence of a metastable solid phase besides the known stable one. A very prominent relaxation process is observed in both solid phases and in the liquid. The ubiquity of this relaxation indicates that it is related to local fluctuations of the hydrogen-bond network between the molecules. The same relaxation is also present when ethanolamine is sandwiched between graphite oxide sheets, but it is slower and characterized by a broader distribution of relaxation times due to the interaction with the graphite oxide matrix.

Contents

1. **Introduction** 1

2. **Techniques and Data analysis**

2.1. Differential scanning calorimetry 9

2.2. X-ray Diffraction 10

2.3. Broad band Dielectric Spectroscopy 12

2.4. Analysis of dielectric spectra 15

2.5. Relaxation processes and models 16

2.5.1. Debye Model 20

2.5.2. Cole-Cole and Cole-Davidson Model 21

2.5.3. Havriliak-Negami Model 23

2.6. Kohlrausch-Williams-Watts function 24

2.7. Temperature dependence of the relaxation behavior 25

2.8. Analysis of conductivity effect in the loss spectra 28

3. **Experimental Implementations of Broad Band Dielectric Spectroscopy** 33

3.1. Measuring powder samples 35

3.2. Measuring Liquid samples 36

3.3. Measuring Thin films 38

3.4. Fabrication of Interdigital Electrodes 39

3.5. Calibration of Interdigital Electrodes 42

3.6. Comparison of the Empty Chip with Bulk Glycerol and with a Drop of Glycerol onto an IDE Device 44

4. Dielectric Studies of Organic and Hybrid Thin Films deposited by Three Different Techniques

4.1. Introduction **47**

4.2. Experimental Details **51**

4.3.Dielectric Relaxations in Rh6G and Rh19 Films **53**

4.4.Conductivity Properties of Rh6G and Rh19 Films **58**

4.5.Preliminary Characterization of Bulk CdI_2EA by DSC and XRD **62**

4.6.BDS Study of bulk CdI_2EA and Langmuir-Blodgett films of ODA-CdI_2EA **64**

4.7. Conclusions **71**

5. Collective relaxation dynamics and crystallization kinetics of Amorphous Biclotymol antiseptic

5.1.Introduction **79**

5.2.Experimental Details **81**

5.3.Primary and Secondary Relaxation Behavior **82**

5.4. Analysis of the crystallization Kinetics **88**

5.5.Conclusions **99**

6. Rotational relaxations in solid (1,1,2,2)Tetrachloroethane

6.1.Introduction **105**

6.2.Differential scanning calorimetry (DSC) analysis **107**

6.3.Experimental Details **108**

6.4.Results and Discussion **109**

6.4.1. Broad band dielectric spectroscopy results

6.4.2. Molecular simulations results **117**

6.5. Conclusions **123**

7. Dielectric studies of pure Ethnolamine and Ethnolamine Intercalated in Graphite Oxide

7.1. Introduction **129**

7.2. Experimental Methods **131**

7.3.DSC and XRD Results on pure Ethnolamine **132**

7.4.BDS Results on pure Ethnolamine **136**

7.4.1. Phase behavior and dc conductivity of pure EAM **136**

7.4.2. Dielectric losses in pure Ethnolamine **140**

7.5.BDS Results on pure EAM-intercalated GO **143**

7.6. Conclusions **145**

8. Conclusions **149**

9. List of Publication **153**

CHAPTER 1

Introduction

Material science and technology plays a crucial role for high-tech industries. While the major exploitation of material science is in thin-film electronics **[1]**, it also has numerous and growing applications in communications, photonics and optical electronics, coatings of all kinds, and in energy generation and conservation strategies. A great many sophisticated analytical instruments and techniques exist, largely developed to characterize thin films and surfaces.The thin film form of a material often has properties significantly different from bulk due to its confined or interfacial character.

Materials are usually in solid form, with their constituents particles (ions, atoms or molecules) closely packed together. The forces between particles are strong so that they cannot move freely but can only vibrate. As a result, a solid has a stable, definite shape, and a definite volume (solids can only change their shape by application of large forces, as when broken or cut).Solids transform into liquids by melting, and liquids transform into solids by freezing. Solids can also change directly into gases through the process of sublimation, and gases can likewise change directly into solids through condensation, as during vapour deposition of films.

In crystalline (ordered) solids, the constituent particles are packed in a regularly ordered, repeating pattern. The same substance can have more than one crystal structure (or solid phase). Materials can also be non-crystalline (amorphous), a prominent example being glasses. The fundamental difference between amorphous and crystalline states is the lack of order in the former. In perfect atomic crystals, atoms are arranged in a defined pattern that repeats periodically in three dimensions to an infinite extent. In amorphous state long-range order is absent and there is no periodicity as present in crystals. Figure 1.1 shows a scheme of the organized pattern in crystalline systems, which is absent in amorphous ones. Glasses and other

amorphous solids without long-range order are not thermally equilibrium ground states.

Amorphous (disordered) materials are not something new. They are well known and have been used by human beings for thousands of years. Although the best example of amorphous solid is window glass made by silica, the amorphous**[2]** or glassy behavior can be found for much wider group of materials like ceramics, polymers, metals,as well as in soft matter and biological systems. Food and pharmaceutical drugs are sometimes prepared in amorphous state during the manufacturing process.

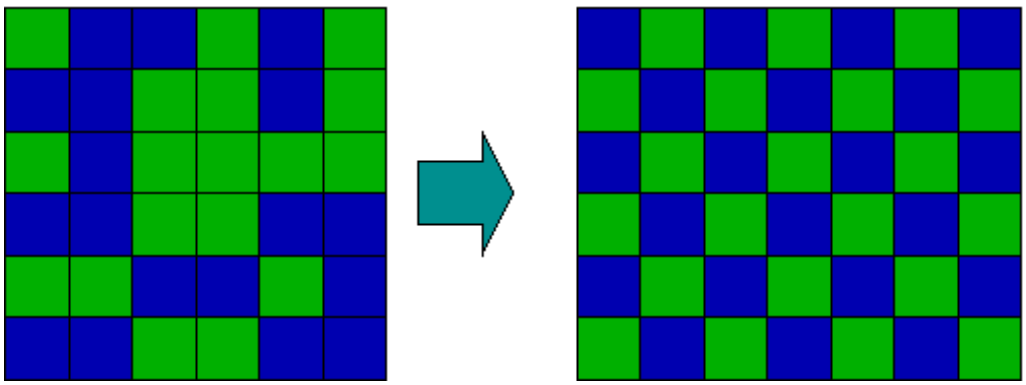

(a) Amorphous (disorder) **(b) Crystalline (ordered)**

Figure (1.1): Schematic 2D representation of thedisordered arrangement of amorphous systems (a) and ofthe (long-range) order pattern for crystals (b)

A glass is a non-crystalline **[3]** solid material that exhibits a glass transition when heated towards the liquid state. The glass state can be achieved by quenching a liquid from high temperature to low temperature. It can be made of quite different classes of materials: inorganic networks (such as window glass), metallic alloys, ionic melts, aqueous solutions, molecular liquids, and polymers.

From the point of view of X-ray diffraction,**[4]** sharp Bragg peaks **[5]**are observed in crystalline samples, while in amorphous systems only broad, structure less features are observed (see Figure 1.2). However, this does not mean complete lack of order, because amorphous materials can still display medium-range (for distances

of the order of 5-20 Å in atomic glasses) or short-range ordering (for distances of a few Å). In amorphous solids the degree of local order might actually be very high.

The amorphous state is thermodynamically unstable(i.e., it possesses a greater free energy than the crystalline counterpart).As a result, amorphous materials tend to revert to the thermodynamically more stable crystalline form. What determines whether a glass remains such for short or very long periods of time, is the time scale (kinetics) of this transition, which depends mainly on temperature (and can depend on humidity conditions or other environmental properties).

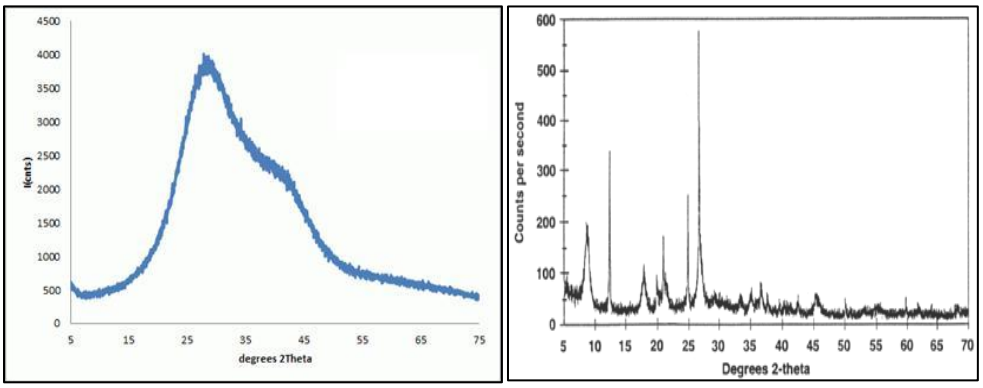

(a) Amorphous **(b) Crystalline**

Figure (1.2): Typical x-ray diffraction patterns of amorphous and crystalline solids

During the formation of structural glass (i.e., a glass characterized by both orientational and translational disorder, see Figure 1.3) the cooling rate plays a significant role, affecting in particular the glass transition temperature, T_g. The glass transition is thus not a true thermodynamic phase transformation but rather a kinetic process, although a lively discussion still exists.**[6,7]** Generally, T_g decreases with decreasing cooling rate, and depends on the technique used to measure it and on thermal history.

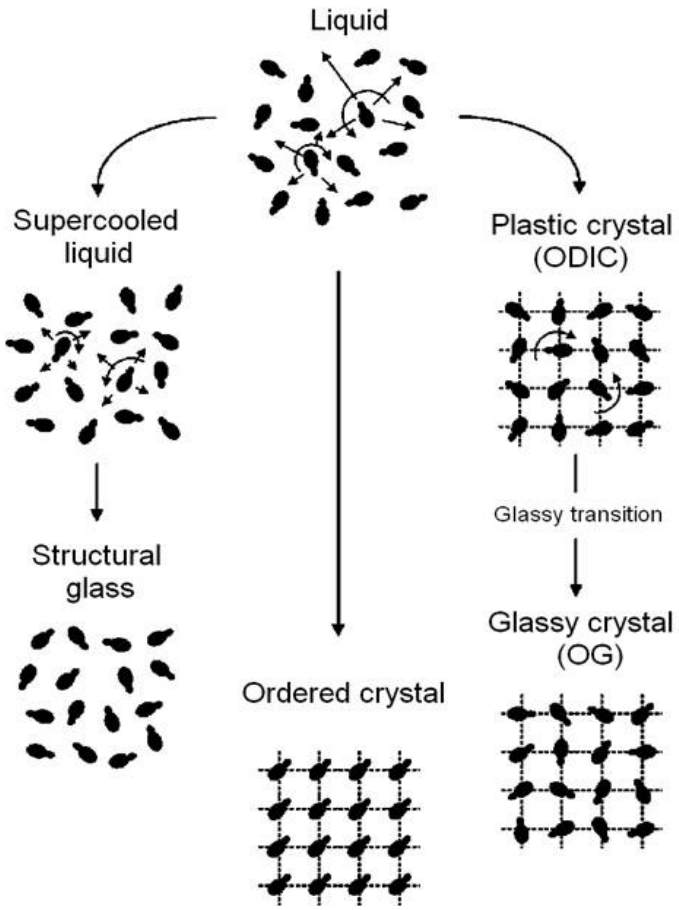

Figure (1.3): Schematic representation of the possible transitions from the liquid state of non-spherical molecules into a structural glass (SG), an ordered crystal or an orientational glassy phase (OG)

Another type of glassy behavior arises when the solid displays only orientational disorder, rather than a full structural disorder. This gives rise to a characteristic state, called "plastic crystal"**[8]**, intermediate between the fully crystalline (translationally and orientationally ordered) state and the liquid phase. The molecular compounds which display a plastic crystalline state are called orientationally disordered crystals (ODIC) or plastic crystals (Figure 1.3). In this phase, the centres of mass of the molecules form a regular crystalline lattice but the

molecular orientations are dynamically disordered. This orientational disorder can freeze yielding a glassy crystal or orientational glass (OG) **[9].**

Low-dimensional disordered systems have been a central theme of recent developments in condensed matter physics. The term low-dimensional systems refers to those systems which contain at least one dimension that is intermediate between those characteristic of atoms/molecules and those of the bulk material. Examples include thin films, nanowires, nanotubes, quantum dots, etc. Due to their limited size (at least in one direction), the properties of low-dimensional systems can be very different to those of their molecular and bulk counterparts. Very well-known examples of low dimensional materials are thin films, which as mentioned have numerous electronic and optoelectronic applications (e.g. in solar cells, light emitting devices, optical switching devices, and thermoelectric devices). In addition to their applied interest, thin films allow the development and study of materials with new and unique properties due to their very high surface area to volume ratio. In addition, the dimensional constraint on the system can give rise to quantum size effects, which can significantly change the material's behavior.

The aim of this thesis is to study the effect of low dimensionality on the electric and dielectric response of materials. In particular, we apply dielectric spectroscopy, a well-known tool to study the conduction and molecular dynamics properties of glass-forming systems, to molecular materials in low-dimensional form or displaying a low degree of disorder. One focus of interest is on the two-dimensional (2D) form of molecular materials. We study three different thin films (two organic and one hybrid organic-inorganic), as well as the effect of confinement of a small-molecule organic material inbetween 2D-sheets of graphene oxide. In the case of thin films, for example, electronic conduction properties are expected to be different from those of their bulk counterparts, due either to different structural properties or to interfacial or confinement effects.In dipolar materials, whose dielectric constant depends on the reorientation of molecular dipoles under an applied field, the dielectric properties can be modified in thin-film form due to the impact of the low-dimensionality on the molecular dipole dynamics. The interest in the molecular

dynamics of 2D materials lies both in reaching a fundamental understanding of the low dimensionality on the dynamic properties, and also in the fact that the fabrication of electronic devices requires the use of thinfilms that are in some cases amorphous, for example polymeric films for lithography, and glassy oxides and nitrides as memory elements and insulators. The quality of the devices depends on the structures of these materials, which in turn affect the molecular mobility and dynamics. Apart from 2D structures, we also study the properties of a metastable glass former that crystallizes into one-dimensional (1D) needle-like crystallites**[10]**, and an orientationally disordered crystal (ODIC) that displays a very low degree of disorder, with the constituent molecules undergoing ratcheting motions between only two allowed orientations.

Chapter 3 of this thesis introduces the details of the implementation of dielectric spectroscopy **[11]** for thin-film samples, which is based on interdigital electrodes deposited on standard silicon wafers. In Chapter 4 we apply this tool to films deposited by three different methods, and which are either all-organic or hybrid organic-inorganic. Interesting results are obtained by comparing the thin-film results with those that we acquired on their bulk counterparts by conventional dielectric spectroscopy.

In Chapter 5 we study the molecular dynamics and crystallization kinetics of an amorphous pharmaceutical compound, namely Biclotymol. The pharmaceutical industry is interested in developing amorphous solid pharmaceuticals that are stable in the amorphous form, for oral delivery of water-insoluble compounds.In fact, about 40% of the existing drugs and 70% of the drugs that are being developed now a days have very poor solubility in water (and thus low bioavailability) in the crystal form, while pharmaceutical compounds in the amorphous state have improved solubility and thus dissolve more rapidly than their crystalline counterparts. The stability of an amorphous pharmaceutical against crystallization is thus a major concern. Motivated by this, we have studied in Chapter 5 the crystallization kinetics of the Biclotymol drug, whose crystallization from thesupercooled liquid state is determined by the extent of molecular dynamics. The interest from a low-

dimensionality perspective lies in the fact that Biclotymol does not crystallize from the supercooled state into its stable, 3D crystal structure, but rather into metastable, needle-like (1D) crystallites. The crystallization kinetics**[12]** of Biclotymol is a textbook-like example of Avrami-law nucleation and growth of a low-dimensional crystalline phase.

Chapter 6 presents the results on the solid phase of a small ethane derivative, namely tetracloroethane. This solid phase exhibits a very special and restricted dynamical disorder, where the molecules exhibit only short-lived orientation jumps out of their equilibrium orientations. Despite the very low degree of disorder, three distinct molecular dynamics processes are observed and identified.

Finally,Chapter 7 deals withthe small organic compound ethanolamine, which is liquid at room temperature and crystallizes in a stable hydrogen-bonded structure at lower temperature.We find that a metastable solid phase also exists, which is formed by rapid cooling the liquid phase and which recrystallizes in the stable crystal upon reheating. A clear relaxation dynamics is observed in all three phases. This relaxation appears to be present also when ethanolamine is intercalated between 2D sheets of graphite oxide. The ubiquity of this relaxation strongly suggests that it is due to local dynamic fluctuations of the hydrogen bond network, present in all phases.Under 2D confinement, this dynamics is slower and displays a larger distribution of characteristic times, as it may be expected.

Together, this thesis constitutes an example of non-conventional application of dielectric spectroscopy to low-dimensional and low-disorder materials. The results show the versatility of this experimental technique, and at the same time the need of complementary tools to reach a full understanding of the experimental results. These tools may range from comparison with the bulk counterpart of a thin-film material, to x-ray diffraction or nuclear magnetic resonance, or to molecular dynamics simulations.

Bibliography:

[1] The Materials Science of Thin Films (2010)

[2] R. Zallen 'The physics of amorphous solids', Wiley (1998)

[3] S.Napolitano, M.Wubbenhorst, J. Phys-Condens. Matter19, 205121 (2007)

[4] He, B. B.; Two-Dimmensional X-ray Diffraction, Wiley & Sons, New Jersey (2009)

[5]http://frontpage.okstate.edu/nanotech/Assignments/Readings/XRD/XRD-Basics.pdf

[6] S. Albert et al. Science, VOL 352 ISSUE 6291,1308 10 JUNE (2016)

[7] A- Droz-Rzoska et al. PHYSICAL REVIEW E 82, 031501 (2010).

[8] J. Timmermans J. Phys. Chem. Biol., vol. 35, p. 331, (1938).

[9] K. Binder and A. Young Phys. Rev. B, vol. 29, p. 2864, (1984).

[10] J.Russo,H.Tanaka,'The microscopic pathway to crystallization in supercooled liquids' submitted to ***Nature,*** private communication

[11] F.Kremer,A.Schonhals, Broadband Dielectric Spectroscopy, Springer-Verlag BerlinHeidelberg New York (2002)

[12] B.Wunderlich,Macromolecular Physics. Crystal Nucleation, Growth, Annealing ;Academic Press: London, (1976); Vol. 2.

Chapter 2

Techniques and Data analysis

The main experimental technique that I employed in my PhD Research is broadband dielectric spectroscopy, complemented by differential scanning calorimetry and X-ray powder diffraction to support dielectric findings.

2.1. Differential scanning calorimetry

Differential scanning calorimetry (DSC) **[1]** monitors heat effects associated with phase transitions or chemical reactions as a function of temperature. In DSC the difference in heat flow to the sample and to a reference at the same temperature is recorded as a function of temperature. The reference is an inert material such as alumina, or just an empty aluminum pan. The temperature of both the sample and reference are increased at a constant rate. Since the DSC measurement is normally done at constant (atmospheric) pressure, the flow of heat is equivalent to enthalpy changes, that is, $\left(\frac{dq}{dt}\right) = \frac{dH}{dt}$, where dH/dt is the heat flow measured in cal s^{-1}. The heat flow difference between the sample and the reference is:

$$\Delta\left(\frac{dH}{dt}\right) = \left(\frac{dH}{dt}\right)_{sample} - \left(\frac{dH}{dt}\right)_{reference} \quad (1)$$

It can be either positive or negative. In an endothermic process, as are most phase transitions on heating, heat is absorbed and therefore, heat flow to the sample is higher than to the reference. Hence Δ(dH/dt) is positive. In an exothermic process, such as crystallization, some cross-linking processes, oxidation reactions, and some decomposition reactions, the opposite is true and Δ(dH/dt) is negative.

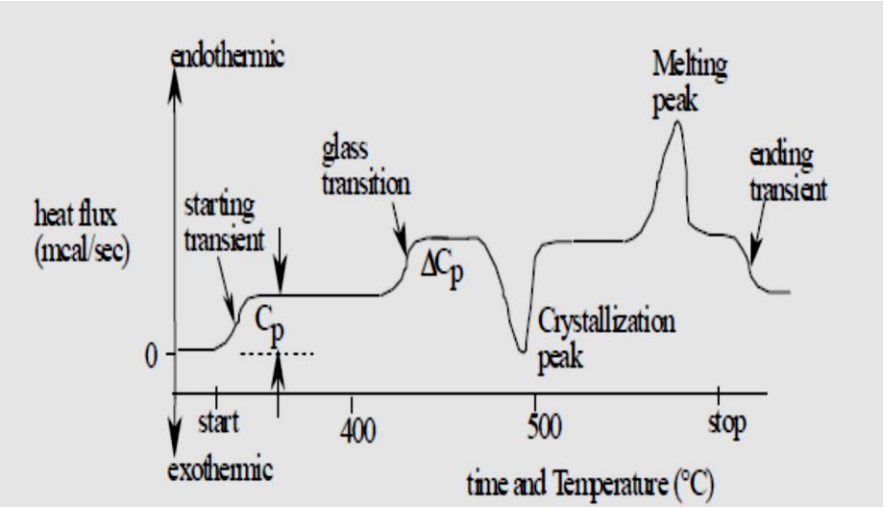

Figure(2.1): DSC scan of sample with exothermic and endothermic peaks including glass transition

Figure (2.1) shows the result of a typical DSC scan on a glass-forming material. The heat capacity of the sample can be calculated from the vertical shift in the baseline at the starting transient. The glass transition causes a further baseline shift. Crystallization is atypical exothermic process and melting is a typical endothermic process. In this thesis, the DSC experiments were performed with a Q100 analyzer from TA instruments equipped with a refrigerated cooling system yielding an operating range from 183 to 823 K. Typical cooling/heating rates used in this thesis were ranged between2 and 10 K/min. The sample atmosphere during DSC experiments is controlled by connecting purge gases (nitrogen or helium) to the setup and a mass flow controller is used to control the flow rate of the gas.

2.2. X-ray Diffraction

X-ray diffraction is a powerful, non-destructive technique by which X-rays of wavelength are diffracted by a sample. The diffraction pattern allows in principle a full characterization of the sample's crystalline structure. X-ray diffraction can be used to provide information on the atomic arrangement in materials with long range order, short range order or not ordered at all. The X-rays are generated by a cathode ray tube,

filtered to obtain monochromatic radiation and collimated to achieve a beam with a well-defined direction, which impinges on the sample. The analysis of X-ray diffraction peaks in single-crystalline materials and polycrystalline powders is based on Bragg's law **[2],** which states that X-rays reflected from adjacent periodic atomic planes separated by a distance *d* of a crystal, interfere constructively when the path difference between them is an integer n multiple of the wavelength λ. The reflected X-rays make an angle of 2θ with the direction of the incident beam. The condition for diffraction can be written as:

$$n\lambda = 2d\sin\theta \qquad (2)$$

The schematic illustration of Bragg's law is presented in Figure (2.2).

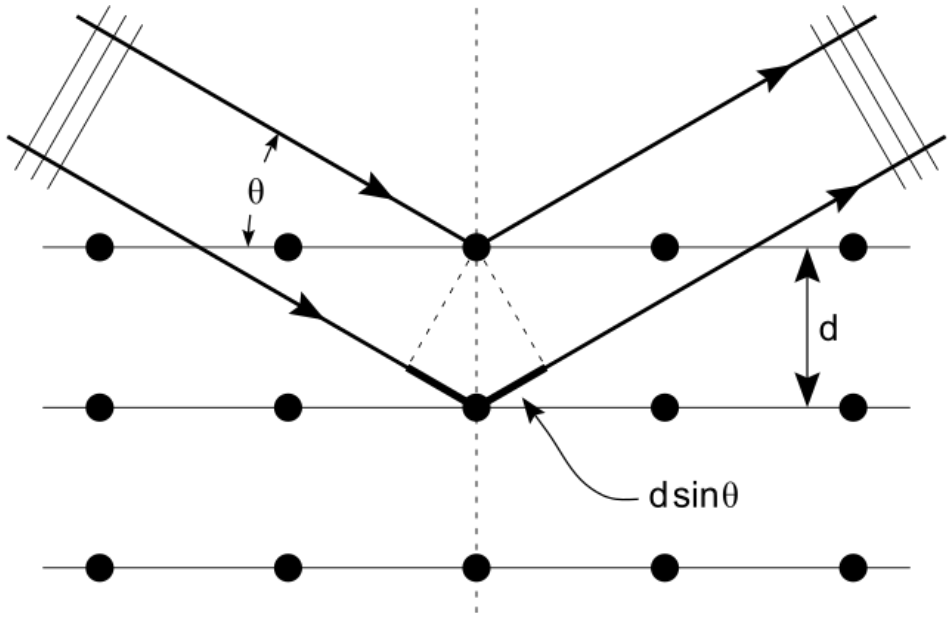

Figure (2.2): Diffraction of X-rays by planes of atoms

Diffraction patterns of crystalline solids reveal presence of sharp peaks corresponding to various crystal planes based on Bragg's law. In a polycrystalline powder sample, the diffraction pattern consists instead of a series of diffraction cones, since the powder

contains crystallites with random orientations. Hence a one-dimensional angular scan is sufficient to record the complete pattern. In fact, for any sets of planes with spacing *d* there will be always few crystallites whose planes satisfy the Bragg reflection law in a given direction forming an angle 2θ with the impinging X-rays. When a powder diffraction pattern is recorded, it thus shows scattering peaks corresponding to the various d spacing's of the crystal lattice. As amorphous solids do not have long range order, there do not exhibit any sharp Bragg peak, but rather, the scattered X-rays form typically one or to two smooth bump-like features with a very broad distribution in the 2θ range.

The high-resolution X-ray powder diffraction profiles used in this work were recorded by means of a vertically mounted INEL cylindrical position sensitive detector (CPS120). The detector was used in the Debye-Scherrergeometry (transmission mode), enabling simultaneous recording of the profiles over a 2θ range between 40 to1200 (angular step ca 0.0290(2θ)). Monochromatic Cu Kα 1 radiation (λ= = 1.54059A0) was selected with an asymmetrically focusing curved quartz monochromator. The generator power has commonly set to 35 kV and 35 mA. External calibration was applied to convert the measured 4096 channels to 2θdegrees, using a cubic spline fitting **[3]** of the diffraction pattern of the cubic phase of $Na_2Ca_2Al_2F_4$. Temperature control is achieved with a liquid nitrogen 700 series Cryostream Cooler from Oxford Cryosystems operating from 500K to 90 K with a temperature accuracy of 0.1 K. The powder or liquid sample is placed into 0.5 mm-diameter Lindemann capillary at room temperature and is continuously rotated perpendicularly to the X-ray beam during data collection to minimize possible effects of preferred orientations. The peak positions are determined by pseudo –Voigt fits performed with dedicated software and in some cases Rietveld refinement is applied.

2.3. Broad Band Dielectric Spectroscopy

The main technique is used in this thesis is broadband dielectric spectroscopy, also known as impedance spectroscopy. Dielectric spectroscopy **[3-6]** is one of the most powerful tool which enables to investigate microscopic dynamic behavior of the

molecules in broad range of frequency (10^{-3}Hz to 10^{12}Hz). The sample (liquid or solid) is mounted between external electrodes connected to the appropriate analyzer which measures the complex impedance of the sample. The distance between the electrodes is adjusted by spacers (thin silica needles with diameter of 50 or 100 μm) in case of liquids, while solid powders are pressed into pellets sandwiched between the electrodes, so that the inter-electrode distance is the thickness of the pellet. In the simplest version of the technique, a sinusoidal voltage $V^*(\omega) = V_0 exp(i\omega t)$is applied to the capacitor filled with sample, causing a current $I^*(\omega)$at the same frequency in the sample. In addition to the intensity of the current, the system measures also the phase shift between the current and voltage, so that a complex impedance is experimentally obtained as Z* = V*/I*. The complex impedance of a capacitor element is

$$Z^*(\omega) = \frac{1}{i\omega C^*(\omega)} \quad (3)$$

where C*(ω)denotes (complex) capacitance. Defining the complex dielectric function $\varepsilon^*(\omega)$of the material by $C^*(\omega) = \varepsilon^*(\omega)C_0$, where C_0 is the capacitance of the empty capacitor, one can extract the dielectric function of the sample as:**[4]**

$$\varepsilon^*(\omega) = \frac{1}{i\omega Z^*(\omega)C_0} \quad (4)$$

The complex dielectric function contains information about polarization, conduction, and molecular dynamic processes in the sample, as discussed in the next Section. Different ways of implementing BDS exist (for example for thin-film samples), which are discussed in detail in Chapter 3.

Dielectric permittivity data are usually measured in the frequency domain at different sample temperatures. The BDS measurement in this thesis were carried out in low frequency range (10^2 to 10^7Hz) using Novocontrol Alpha Analyzer and in the high frequency range (10^6 to10^9 Hz) by an Agilent HP4291 impedance analyzer. For

measurements in the high-frequency range (10^6 Hz to 10^9Hz) a coaxial reflection technique has been used.

The drawing of a typical full setup is shown in figure 2.3.

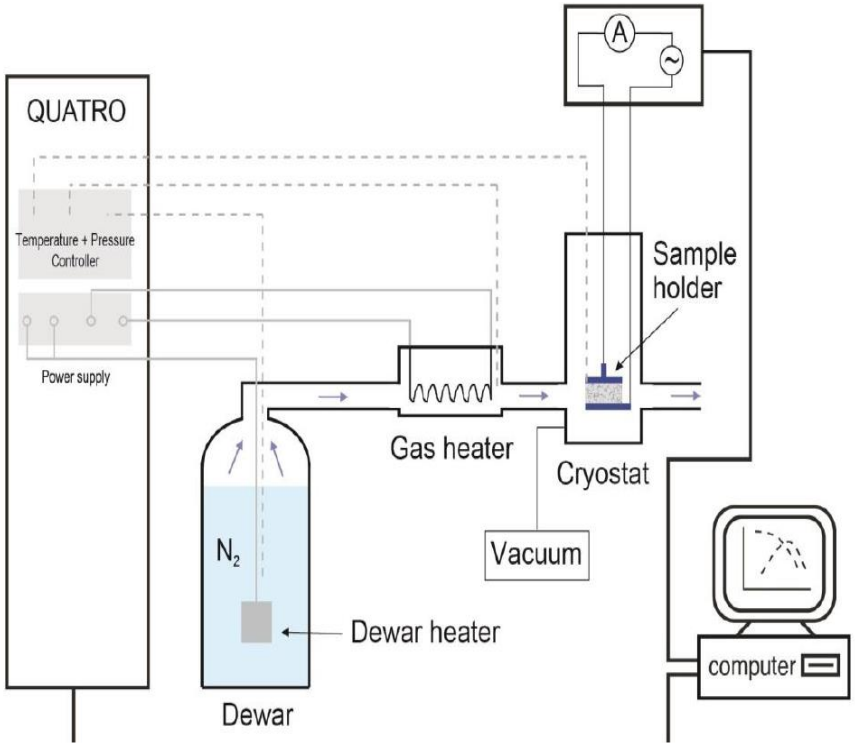

Figure (2.3): Schematic representation of the experimental setup of a temperature dependent broadband measurement

The setup consists of sample holder, cryostat, a liquid nitrogen dewar with pressure sensor, two heating units (dewar and gas heaters) three temperature controllers (for the dewar, gas and sample temperature) and a vacuum pump. The sample holder is placed inside the cryostat where temperature of the sample is varied by the flow of cold nitrogen gas which passes through the gas heaters inserted between the dewar and the cryostat. A PT-100 platinum resistor sensor is used to measure the sample temperature, by placing it in thermal contact with one of the capacitor plates. The temperature range of the system can vary between 116 and 773K with a precision of 0.1K.

2.4. Analysis of Dielectric Spectra

BDS measures the complex dielectric function $\varepsilon^*(\omega) = \varepsilon'(\omega) - i\varepsilon''(\omega)$ of a material. To analyze the dielectric response of sample, mostly the imaginary part $\varepsilon''(\omega)$, called loss spectrum, is taken into consideration. $\varepsilon''(\omega)$ is termed dielectric loss because it is a measure of the field energy dissipated in the sample (of course, there is no loss of energy, but the dissipation leads to a heating of the sample). It contains both a dc conductivity contribution and a number of so-called loss features, which appear in the form of very broad peaks in the loss spectrum, and which correspond to different types of relaxation processes. Relaxation processes may stem from specific molecular dynamics mechanism present in the material. The real part of the complex dielectric function exhibits a step-like decrease in correspondence to each relaxation process recorded in the loss spectrum.

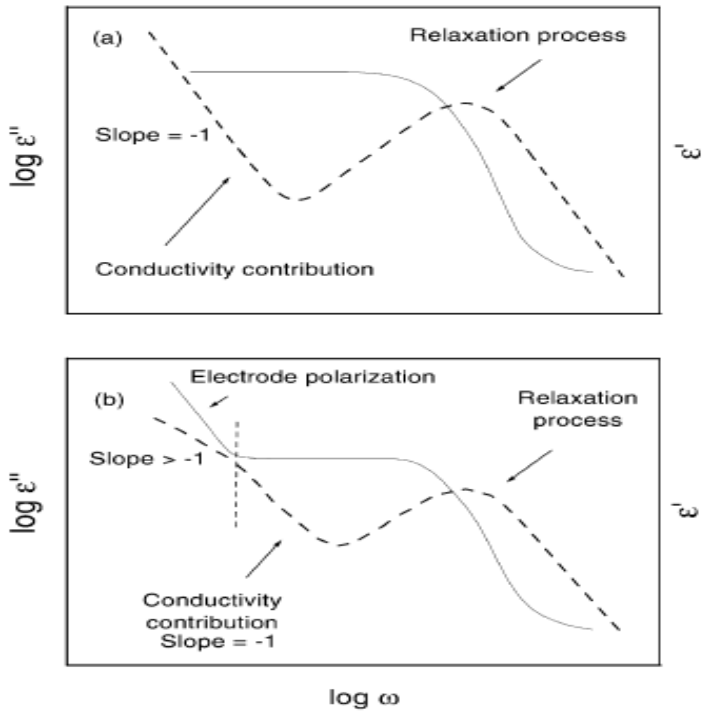

Figure (2.4): Representation of typical dielectric spectra, both in real and imaginary parts of the complex dielectric function. Compared to panel (a), panel (b) shows the case of a sample exhibiting a pronounced electrode polarization effect

In figure 2.4(a), the dashed lines represent the imaginary (loss) spectra, where a relaxation process is visible, and continuous line represents the real part of permittivity. The steep increase of the loss spectrum at low frequency is due to the dc conductivity contribution (Joule loss).

In figure 2.4 (b) the spectrum contains an additional feature called electrode polarization, and arises due to accumulation of charges at the interface between the sample and the electrodes. This polarization effect arises at very low frequency and also gives a step-like increase in real part of permittivity.

The reason why a peaked feature appears in the loss spectrum when a dynamic process is present can be explained by the fluctuation-dissipation theorem. According to this theorem **[9]**, any dynamic process (that is, any time dependent fluctuation of particles within the sample) will lead to an enhancement of the loss when the field frequency matches the frequency of this fluctuation. There are various types of dynamics that can be observed by means of BDS, which are discussed in the next Section.

2.5. Relaxation Processes and Models

Different dynamic processes may be observed by BDS. Some of them stem from molecular dynamics, while other stem from conductivity effects. For example, both cooperative and local whole-molecule dynamic processes can be observed, as well as internal dynamics of individual molecules. As for conduction-related processes, in heterogeneous or phase-separated samples a space-charge relaxation is observed, which stems from accumulation of charge carriers at the interface between the different phases, as in the electrode polarization effects. Space-charge relaxations are however also observed in more homogeneous systems, where they stem from local polarization effects, for example at grain or domain boundaries in polycrystalline powders/films.

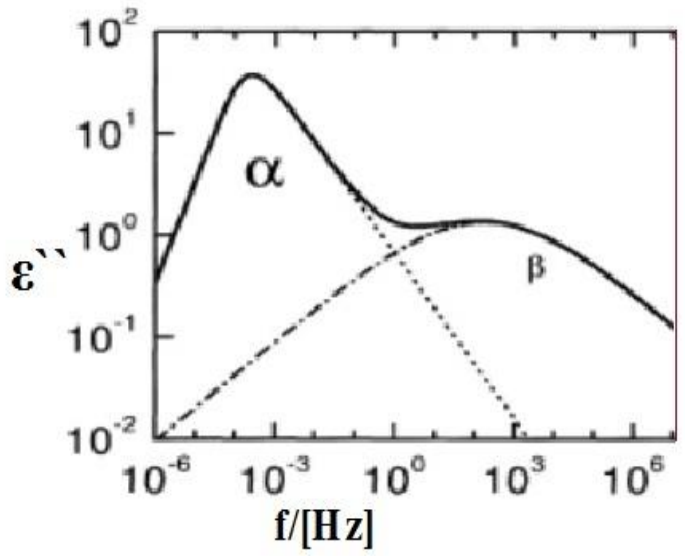

Figure2.5: Scheme of dielectric loss feature of typically dynamically disordered material, two loss feature are shown: primary, α relaxation and secondary β relaxation

Figure 2.5 shows a typical loss spectrum of a glass-forming material, where two distinct relaxation dynamics can be identified. The so-called primary relaxation process (α process), commonly found in glass forming systems, corresponds to the structural cooperative rearrangement of the molecules, and is closely associated with the glass transition temperature. It is the most prominent feature observed in glass forming liquids cooled fast enough to avoid their crystallization. The α relaxation commonly displays strong non-Debye profile of the relaxation function (see below).With decreasing temperature both the relaxation time of the α relaxation and the viscosity increase strongly, exhibiting a dramatic increase close to the glass transition temperature, which can be at least approximately described by the empirical Vogel-Fulcher-Tammann equation (explained in section 2.7).

Many glass-forming systems show additional relaxation processes beyond the α process called secondary relaxations (and labeled as β or γ, δ, etc.) with an Arrhenius-type temperature dependence (see section 2.7). The intensity (strength) of secondary relaxations is usually smaller than α process, and the frequency higher, as visible in figure 2.5. Secondary relaxations can correspond, for example, to intramolecular (non-

cooperative) motions (e.g. of mobile side groups or subunits of a larger molecule). Another type of secondary relaxation, called Johari-Goldstein relaxation process **[4],** does not involve an intramolecular motion but rather a non-cooperative motion of the entire molecule, possibly related to the existence of local heterogeneities with high molecular mobility. Another interpretation of Johari-Goldstein process is based on the so-called Coupling Model **[4]**, which states that the secondary relaxation is actually a "precursor" relaxation of collective α process. In such case, the relaxation time of the α process is related to that of the β relaxation as:

$$\tau_{JG} = t_c^n (\tau_\alpha)^{1-n} \quad (5)$$

Here, t_c is the crossover time and n is equal to $1 - \beta_{kww}$, where β_{kww} is the exponent of the stretched Kohlrausch correlation function describing the α loss feature in the time domain (see section 2.6).

To analyze the relaxation processes in more detail, the measured loss spectra are usually fitted using different model functions named Debye, Cole-Cole, Cole-Davidson, Havriliak-Negami. These model functions are all more or less phenomenological, but they allow extracting the frequency position or time of relaxation process, and also provide quantitative information about its intensity (the so-called relaxation strength, Δε) and on the asymmetry and shape of the relaxation feature.

Another contribution to the dielectric loss comes from the dc conductivity and from conductivity related loss features. In disordered systems the charge transport takes place due to hopping conduction. The motion of charge in these systems gives rise to a weak and broad relaxation process. This is shown in figure 2.6, where a broad dielectric loss is detected at higher frequency, while at low frequency a linear background is visible, which is due to the dc conductivity contribution. That this is the case is best visualized in the conductivity spectra$\sigma'(f)$, defined as $\sigma'(f) = 2\pi f \varepsilon_0 \varepsilon''(f)$. An example is displayed in Figure 2.7, where the dc conductivity shows up as a horizontal plateau at low or intermediate frequency in the conductivity spectra.

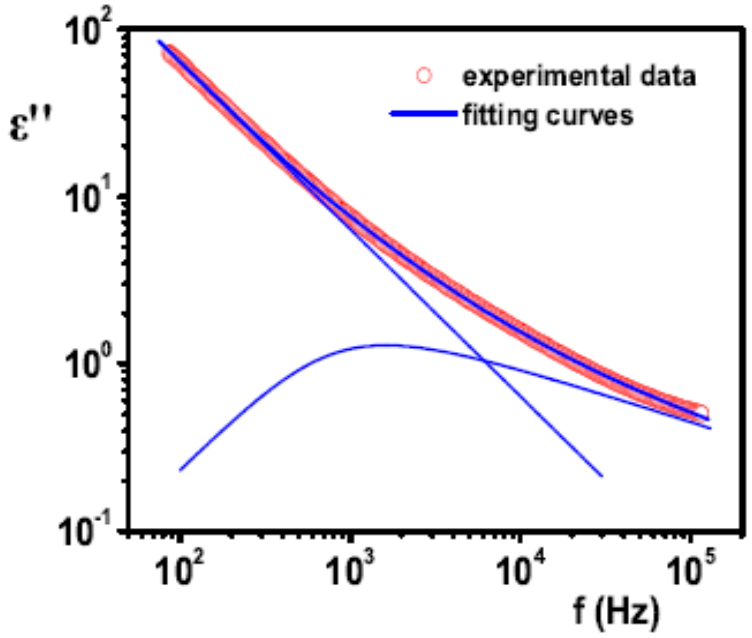

Figure (2.6): Experimental spectrum displaying a broad conductivity-related dielectric loss feature on top of a dc conductivity background at low frequency.Solid lines represent the two separate components.

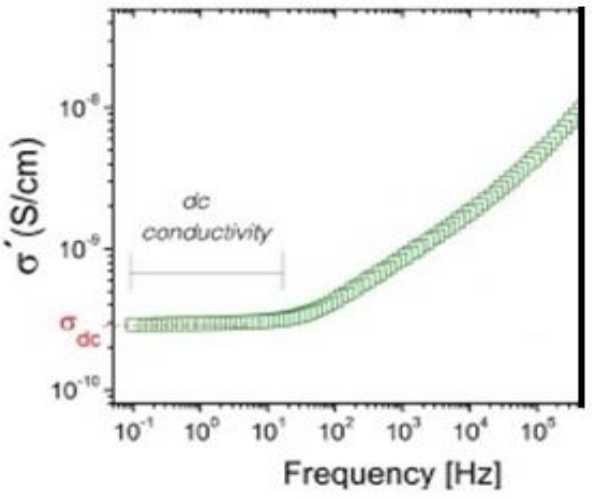

Figure2.7: Example of dc conductivity plateau at low frequency region

2.5.1. Debye Model

Debye proposed that relaxation for a dipolar system in non - equilibrium takes place with a rate that increases linearly with the distance from equilibrium. This behavior can be described with the following first order **[7]** differential equation:

$$\frac{dP(t)}{dt} = -\frac{P(t)}{\tau_D} \quad , \tag{6}$$

Where τ_D is a characteristic relaxation time. Equation (6) leads to an exponential decay of the correlation decay function:

$$\emptyset(t) = \exp\left(-\frac{t}{\tau_D}\right) \tag{7}$$

The Debye function for the frequency dependence of loss feature ε*(ω) is given by **[8]**:

$$\varepsilon^*(\omega) = \varepsilon_\infty + \frac{\Delta\varepsilon}{1+i\omega\tau_D} \tag{8}$$

The real and imaginary part of the complex permittivity can be separated from equation (8) as:

$$\varepsilon' = \varepsilon_\infty + \frac{\Delta\varepsilon}{1+(\omega\tau_D)^2} \tag{9}$$

$$\varepsilon'' = \Delta\varepsilon\frac{\omega\tau_D}{1+(\omega\tau_D)^2} \tag{10}$$

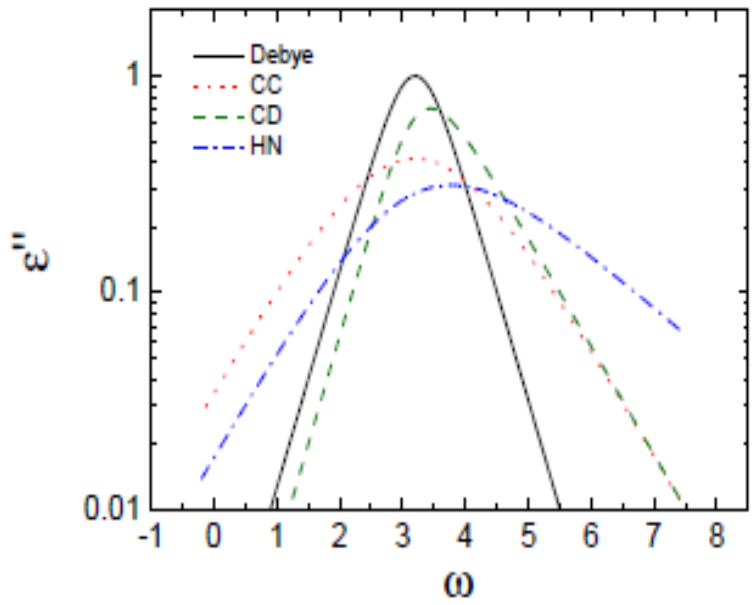

Figure (2.8): Imaginary part of the dielectric permittivity for Debye, Cole-Cole (CC), Cole-Davidson (CD) and Havriliak-Negami (H-N) equations

Derived within certain models for molecular reorientation, e.g., isotropic rotational diffusion **[4]**, the Debye relaxation is not really suited to describe the dielectric response of all kinds of systems. Other semi-empirical expressions have been introduced to add additional cases in which the experimental half-width is much broader than that predicted by the Debye equation. This broadening can be described by other, more phenomenological equations, such as the Cole-Cole or Cole-Davidson functions (Figure 2.8) **[8]**.

2.5.2. The Cole-Cole and Cole-Davidson functions

In most cases the experimental half-width is much broader than predicted by the Debye equation. This broadening can be described by the Cole-Cole (CC) function (Figure 2.8) **[8]**:

$$\varepsilon_{CC}(\omega) = \varepsilon_{\infty} + \frac{\varepsilon_s - \varepsilon_{\infty}}{1+(i\omega\tau_{CC})^{\beta}} \qquad (11)$$

The real and imaginary part of the complex permittivity can be separated from equation (11) as:

$$\varepsilon'(\omega) = \varepsilon_\infty + \frac{\Delta\epsilon(1+\omega\tau_{CC})^\beta \cos(\alpha\pi/2)}{1+2(\omega\tau_{CC})^\beta \cos(\alpha\pi/2)+(\omega\tau_{CC})^{2\beta}} \quad (12)$$

$$\varepsilon'' = \Delta\varepsilon \frac{(\omega\tau_{CC})^\beta \sin(\alpha\pi/2)}{1+2(\omega\tau_{CC})^\beta \cos(\alpha\pi/2)+(\omega\tau_{CC})^{2\beta}} \quad (13)$$

where $0 < \beta \leq 1$ leads to a symmetrical broadening of the relaxation function. For $\beta = 1$ the Debye function is obtained. The position of the maximal loss is related to the Cole-Cole relaxation time by the relation $\omega_{max} = 1/\tau_{CC}$. Many experimental results, especially on liquids or molecular glass forming materials, show that the complex permittivity function can have an asymmetric broadening (Figure 2.8). This behavior is better described by the Cole-Davidson equation, introduced in 1950 by Davidson and Cole **[9]:**

$$\varepsilon_{CD}(\omega) = \varepsilon_\infty + \frac{(\varepsilon_S - \varepsilon_\infty)}{(1+i\omega\tau_{CD})^\gamma} \quad (14)$$

and it can be separated in the real and imaginary part as follow:

$$\varepsilon'(\omega) = \varepsilon_\infty + \Delta\varepsilon\cos(\emptyset)^\gamma \cos(\beta\emptyset) \quad (15)$$

$$\varepsilon'' = \Delta\varepsilon\cos(\emptyset)^\gamma \sin(\beta\emptyset) \quad (16)$$

with $\tan\phi = \omega_{CD}$ and $0 < \gamma \leq 1$. The CD function gives an asymmetrically broadened peak for the imaginary part ε"(ω) with a power-law proportional with ω on the low frequency side and another proportional with $\omega^{-\gamma}$ on the high frequency side. Again, for $\gamma = 1$ the Debye function is obtained. For an asymmetric model function the Cole-Davidson time parameter τ_{CD} of the model does not coincide with the relaxation time

related to the maximal loss. The relation between these two quantities depends on the shape parameter γ as follows:

$$\omega_{max} = \frac{1}{\tau_{CD}} tan\left[\frac{\pi}{2\beta+2}\right] \quad (17)$$

2.5.3. The Havriliak-Negami function

A more general function to model the relaxation response is the Havriliak-Negami (HN) function defined as **[10, 11]:**

$$\varepsilon_{HN}(\omega) = \varepsilon_\infty + \frac{(\varepsilon_s - \varepsilon_\infty)}{[1+(i\omega\tau_{HN})^\beta]^\gamma} \quad (18)$$

where β and γ are the shape parameters with values between 0 and 1 (see Figure 2.8). The separation of the real and imaginary part of the complex permittivity gives rather complex expressions:

$$\varepsilon' = \varepsilon_\infty + \Delta\varepsilon\left[1 + 2(\omega\tau_{HN})^\beta \cos\left(\frac{\beta\pi}{2}\right)(\omega\tau_{HN})^{2\beta}\right]^{-\gamma/2} \cos\left[\gamma \arctan\left(\frac{\sin(\beta\pi/2)}{(\omega\tau_{HN})^{-\beta}+\cos(\gamma\pi/2)}\right)\right] \quad (19)$$

$$\varepsilon'' = \Delta\varepsilon\left[1 + 2(\omega\tau_{HN})^\beta \cos\left(\frac{\beta\pi}{2}\right)(\omega\tau_{HN})^{2\beta}\right]^{-\gamma/2} \sin\left[\gamma \arctan\left(\frac{\sin(\beta\pi/2)}{(\omega\tau_{HN})^{-\beta}+\cos(\gamma\pi/2)}\right)\right] \quad (20)$$

It is worth noticing that the HN function is a combination of the CC (γ = 1) and CD (β = 1) functions and it reduces to the Debye behavior for β= γ = 1. The frequency of maximal loss depends on the β, γ and τ_{HN} parameters and is given by:

$$\omega_{max} = \frac{1}{\tau_{HN}}\left[\sin\frac{\beta\pi}{2\gamma+2}\right]^{1/\beta}\left[\sin\frac{\beta\gamma\pi}{2\gamma+2}\right]^{-1/\beta} \quad (21)$$

Usually, only the HN function is able to describe the experimental data in the whole frequency range of BDS. This means that for a complete description of the frequency behavior of a relaxation region, at least a set of four parameters is needed. If several

relaxation processes are observed in the measured frequency window, a combination of several HN function scan be used to describe and separate the different processes. Provided that the different relaxation regions are independent and hence that the contribution of each process to the complex dielectric function is additive, the total dielectric function will be given by $\sum_k \varepsilon^*_{HN,k}(\omega_i)$ where k runsover all the relaxation processes.

2.6. The Kohlrausch-Williams-Watts function

Dielectric measurements can be performed either directly in the time domain (with the transient currents method) **[18, 19]** or in the frequency domain (with the broadband dielectric spectroscopy). In many cases the non-Debye relaxation behavior can be described, in the time domain, by the empirical Kohlrausch-Williams-Watts (KWW) function **[4]**.

In the time domain, the decay function (t) is more stretched (broader) than the simple exponential function that would correspond to a Debye process. To model this non-exponential character it is possible to use the KWW function, introduced by Kohlrausch in 1847 **[12]** and modified by Williams and Watts to describe relaxation processes in polymers **[13].** The KWW equation for the permittivity in the time domain is:

$$\varepsilon_{KWW}(t) = \varepsilon_\infty + \Delta\varepsilon\left[1 - exp\left(-\frac{t}{\tau_{KWW}}\right)^{\beta_{KWW}}\right] \quad (22)$$

Here, β_{KWW} is the so-called stretching exponent which has values between 0 and 1. The KWW function has no analytic Fourier transform in the frequency domain. There exists however an approximate connection between the H-N function and the KWW expression. In particular, it has been shown that approximate relations hold between the HN shape parameters β and γ and the stretching parameter β_{KWW}, as well as between the corresponding relaxation times. The two relationships are **[17]:**

$$\beta_{KWW} = (\beta\gamma)^{1/1.23} \quad (23)$$

$$ln\left(\frac{\tau_{HN}}{\tau_{KWW}}\right) = 2.6(1-\beta_{KWW})^{1/2}\exp(-3\beta_{KWW}) \quad (24)$$

2.7. Temperature Dependence of the Relaxation Behavior

Upon decreasing the temperature, the relaxation time of any dynamic process increases (or equivalently, its frequency decreases). In structural glass formers, for example, the frequency of the cooperative molecular motions exhibits a dramatic slow-down upon approaching the glass transition temperature. The Arrhenius activation model is the simplest one that can be applied to describe the temperature dependence of relaxation times. The Arrhenius temperature behavior of relaxation time is given by **[7,8]**:

$$\tau = \tau_0 \, exp\left({E_a}/{k_B T}\right) \quad (25)$$

Here E_a is the temperature-independent activation energy for the relaxation process, which represents the energy barrier for the process to occur**,** k_B is the Boltzmann's constant, and τ_0 is the relaxation time in the high-temperature limit where co-operativity is lowest.(Figure 2.9) **[4,18]**

In most cases the experimentally measured temperature dependence of molecular motions cannot be described satisfactory by simple Arrhenius equation, but the Vogel-Fulcher-Tamman equation **[19-26]**(VFT) should be used instead. This equation is given by: **[79, 80, 81]**

$$\tau_\alpha = \tau_0 \, exp\left[\frac{B}{T-T_{VF}}\right] \quad (26)$$

Here T_{VF} (Vogel– Fulcher temperature) and B are phenomenological parameters. If T_{VF} = 0 K, the VFT equation reduces to the Arrhenius expression**[18]** and the constant B to $B = E_a/ k_B$.

In Eq. (2.26), the factor B is sometimes written as $B = DT_{VF}$, where D is called 'strength coefficient'.

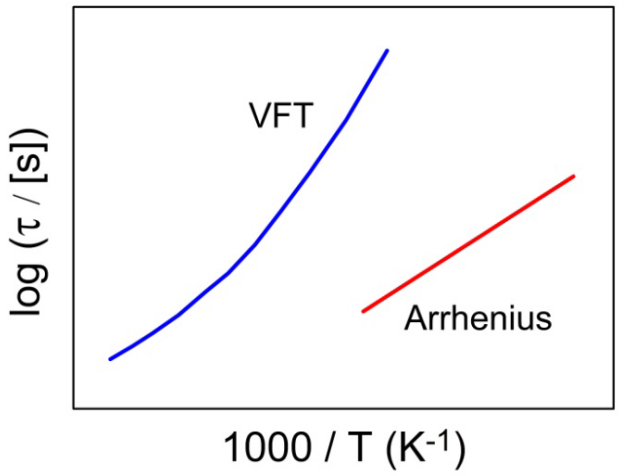

Figure (2.9): Arrhenius plot of two relaxation processes with two different temperature dependences. The relaxation process at longer times (blue curve) is described by a Vogel-Fulcher-Tammann behavior (Eq. 2.26) and the process at shorter relaxation times (red line) follows an Arrhenius dependence (Eq. 2.25)

The VFT function is very useful to describe the temperature dependence of structural relaxation times in glass-forming materials.

Extrapolation of the VTF fit to 100 seconds is a usual way of estimation the glass transition temperature (T_g) from dielectric measurements. A standard scheme for characterization of glass-forming liquids is based on the concept of 'kinetic fragility', which is a measure of the non-Arrhenius character of the temperature dependence of the cooperative relaxation times **[27]**(when the temperature dependence of structural relaxation times in the supercooled liquid is Arrhenius -like, the material is a 'strong' glass-former, otherwise it is termed 'fragile').

The fragility concept is usually demonstrated on so-called Angell plot **[27]**, showing the logarithm of the structural relaxation time as a function of inverse temperature normalized to unity at T_g (Figure 2.10).

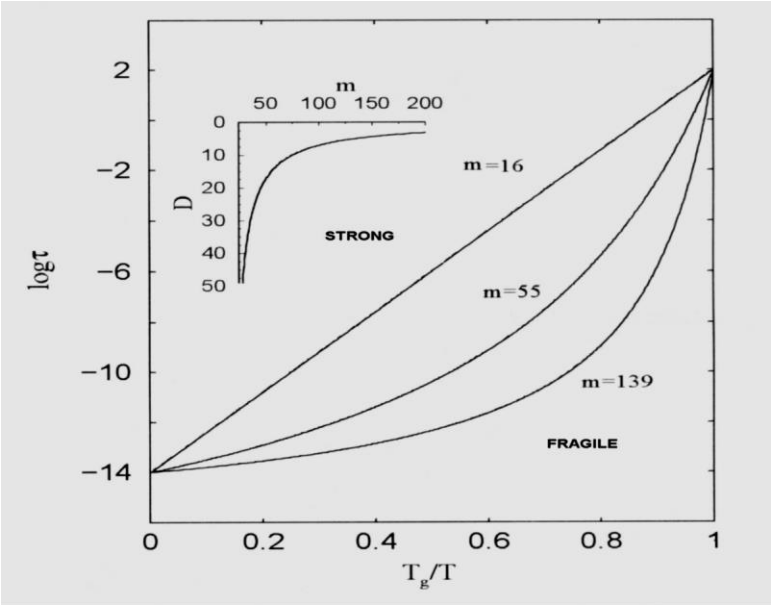

Figure (2.10): Temperature dependence (normalized to T_g) of the logarithmic relaxation time. This graphical representation, called Angell plot, is used to classify supercooled liquids as strong or fragile according to their deviation from the Arrhenius-like behaviour. The inset exhibits the strength coeffcient D as a function of the fragility parameter m.

The most common measure of fragility is the 'steepness index', defined in the following way:

$$m = \left(\frac{d\log\tau(T)}{dTg/T}\right)\text{at } T=T_g \qquad (27)$$

The minimal and maximal constraints of the fragility are m_{min}= 16 (strong liquids) and m_{max}= 200 (fragile liquids). By analyzing the temperature behavior of structural relaxation times for more than 70 compounds Angell and co-workers **[28]** found that in the vast majority of cases, viscous liquids show faster than predicted from Arrhenius relation change in their relaxation times (or viscosities) upon cooling toward the glass transition, with $m \sim 80$ being atypical value for fragile glass-formers.

Another possible measure of fragility is the 'strength parameter' D. Small values of D (D <10) are typical for fragile systems, whereas larger ones are common for strong systems (D>10).

2.8. Analysis of conductivity effects in the loss spectra

As mentioned above, the dc conductivity of a sample is visible in the low frequency region of dielectric loss spectra as a steep increase with decreasing frequency, or equivalently as a horizontal plateau in the real part of the ac conductivity $\sigma'(f)$. The complex ac conductivity is related to the complex permittivity by the relation **[4]**:

$$\sigma^* = i\omega\varepsilon_0\varepsilon^* \qquad (28)$$

where ε_0 is the permittivity of free space.

In disordered systems, charge transport takes place due to hopping conduction. There exist several theories of hopping conduction, such as variable range hopping, phonon-assisted hopping, or nearest neighbor hopping.

The dc conductivity σ_{dc} of a given sample is calculated as the plateau value of $\sigma'(f)$ at low frequency, as clearly visible for example in the series of spectra shown in Figure 2.11.

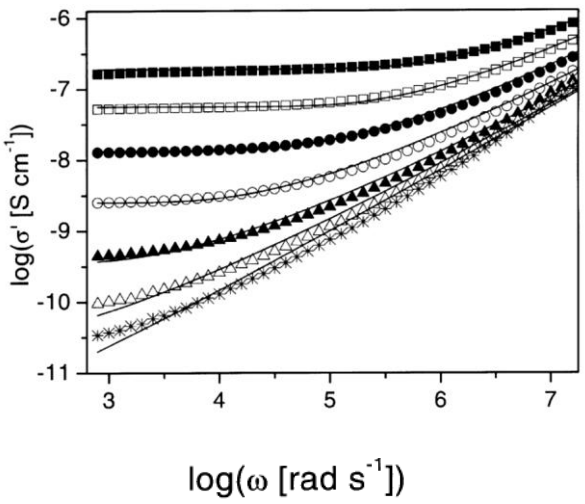

Figure (2.11): real part of the complex conductivity spectra of a disordered conductor, as a function of frequency, at different temperatures.

For further analysis, the extrapolated values of $\sigma_{dc}$are usually plotted as a function of temperature as an Arrhenius plot, which is the plot of the logarithm of σ_{dc} as a function of the inverse temperature (1000/T) **[29]**. This procedure allows analyzing directly the temperature –activated behavior of conduction. In the case of electronic hopping, the Arrhenius plot usually displays a power law dependence of the type $Log(\sigma_{dc}) = A - B/T^n$**[29]**, where the exponent n lies between 0< n ≤1. Such analysis is useful to reveal the nature of charge species participating in conduction.

The conduction properties of a sample can also be analyzed in terms of the imaginary modulus spectra, where the complex modulus is defined as $M^* = 1/\varepsilon^*$.

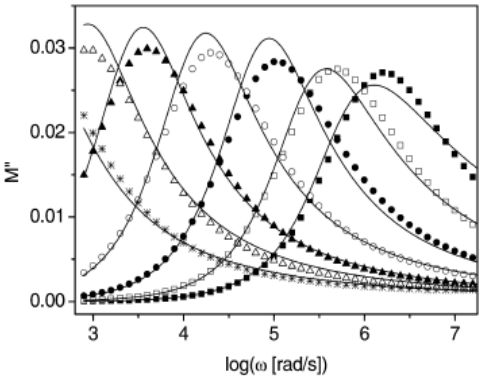

Figure (2.12): modulus spectra corresponding to the data of Figure 2.11

As shown in figure 2.12, a peak is visible in the modulus representation in correspondence to the dc conductivity plateau. The characteristic frequency of this feature, usually termed "conductivity relaxation", can be obtained as the spectral position of the modulus maximum by fitting the spectrum with an appropriate model function (HN, Cole-Davidson, Debye) in the modulus representation.

Finally, as mentioned at the beginning of Section 2.5, a broad space-charge feature is sometimes present in the permittivity spectra, or as bump or high-frequency increase in the conductivity spectra (see figures 2.7 and 2.11). By fitting such loss feature one can obtain the space-charge relaxation frequency f_{sc} and strength $\Delta\varepsilon_{sc}$ of the process. By

plotting the dc conductivity σ_{dc} *vs* $2\pi\Delta\varepsilon\varepsilon_0 f_{sc}$, a linear correlation should result, with slope close to unity so that $\sigma_{dc} \approx 2\pi\Delta\varepsilon\varepsilon_0 f_{sc}$. This last relationship is known as Barton-Nakajima-Namikawa (BNN) **[4]** condition, and signifies that the mechanism driving conduction is basically the same at all temperature range, and that the relaxation feature is indeed a space-charge relaxation.

Bibliography:

[1] J.C.Phillips, M.F.Thorpe, Phase Transitions and Self-Organization in Electronic and Molecular Networks, Fundamental materials research, Kluwer academic Publishers new York, boston, Dordrecht, London, Moscow (2002)

[2] M.Evain, P.Deniard, A.Jouanneaux, and R.BrecJ.Appl. Cryst.,vol. 26, p. 563, (1993)

[3] P.Lunkenheimer, U.Schneider, R.Brand, and A.Loidl Contemporany Physics, vol. 41, p. 15, (2000)

[4] F.Kremer and A.Schonhals, Broadband Dielectric Spectroscopy. Berlin: Springer, (2002)

[5] P. Lunkenheimer and A. Loidl Chem. Phys., vol. 284, p. 205, (2002)

[6] http://www.novocontrol.de/.

[7] P Debye, Polar Molecules. New York: Chem. Catalog., (1929)

[8] H.Frohlich, Theory of Dielectrics. London: Oxford Univ. Press,(1958)

[9] K.S. Cole and R. H. Cole J. Chem. Phys., vol. 9, p. 341, (1941)

[10] D.W.Davidson and R.H.Cole J. Chem. Phys., vol. 18, p. 1417,(1950)

[11] S.Havrilliak and S.NegamiJ.Polym.Sci C, vol. 16, p. 99, (1966)

[12] S.Havrilliak and S.Negami Polymer, vol. 8, p. 161, (1967)

[13] R. KohlrauschPogg. Ann. Phys., vol. 12(3), p. 393, (1847)

[14] G.Williams and W. D. C. Trans. Faraday Soc., vol. 66, p. 80, (1970)

[15] A.Alvarez, A.Alegria, and J. Colmenero Phys. Rev. B, vol. 44,p. 7306, (1991)

[16] P. Hedvig Dielectric Spectroscopic of Polymers. Bristol: Hilger, (1977)

[17] N.G. McCrum, B.E.Read, and G.Williams, Anelastic and DielectricEffects in Polymeric Solids. London: Wiley, (1967)

[18] C.J.F Bottcher Theory of electric polarization, vol.I Dielectrics in static fields. Amsterdam, Oxford , New York: Elsevier, (1973)

[19] H. Vogel Phys. Z., vol. 22, p. 645, (1921)

[20] G. S. Fulcher J. Am. Ceram. Soc., vol. 8, p. 339, (1925)

[21] G. Tammann and W. Hesse Z. Anorg.Allg. Chem., vol. 156, p. 245,926 (1984)

[22] E. J. Donth, The Glass Transition: Relaxation Dynamics in Liquidsand Disordered Materials. Berlin: Springer, (2001).

[23] J.C. Dyre Rev. Mod.Phys., vol. 78, p. 953, (2006)

[24] C.A. Angell Proc. Natl. Acad. Sci., vol. 92, p. 6675, (1995)

[25] G.FloudasProg. Polym.Sci., vol. 29, p. 1143, (2004)

[26] C.M.Roland, S.Hensel-Bielowka, M.Paluch, and R. CasaliniProg. Prog.Phys., vol. 68, p. 1405, (2005)

[27] Angell, C.A., Strong and fragile liquids, Relaxations in Complex Systems, edited by K.L. Ngai and G. B. Wright (U.S. GPO, Washington, D.C) pp. 3-11, (1985)

[28] Bóhmer, R.; Ngai, K. L.; Angel, C. A.; Plazek, D. J.; J. Chem. Phys., 99, 5899,(1993)

[29] Roberto Macovez, ManeshZachariah, Michela Romanini, Panagiota Zygouri, DimitriosGournis, JosepLluísTamarit, J. Phys. Chem. C, 118 (23), pp 12170–12175,(2014)

Chapter 3

Experimental Implementations of broad band dielectric spectroscopy

The simplest way to perform dielectric spectroscopy measurements is by sandwiching a sample (liquid or solid) between two metallic electrode plates, to form a parallel-plate capacitor (Figure 3.1). A generator applies a voltage $V(\omega)$ at frequency $\omega/2\pi$ to one of the capacitor plates. The sample current $I(\omega)$ is determined at the other capacitor electrode by means of a vector current meter that measures, in addition to the current amplitude I_0, also the phase shift φ of the current with respect to voltage.

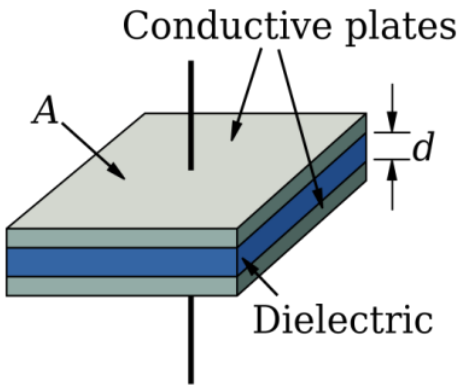

Figure (3.1): Scheme of a parallel-plate capacitor

Such a system measures therefore the complex impedance of the capacitor $Z(\omega)$, defined as:

$$Z(\omega) = \frac{V(\omega)}{I(\omega)} \qquad (1)$$

where now $V(\omega)$ and $I(\omega)$ are complex quantities to take into account their phase. Since for a circuit made of a single capacitor of capacitance C (with no series or

parallel resistance) the complex impedance is $Z = 1/i\omega C$, a complex capacitance of the filled capacitor (or equivalently, of the sample) is defined, from the measured impedance given by Eq. (1) as: $C(\omega) = 1/i\omega Z(\omega)$.

The capacitance of a parallel plate capacitor is $C = \varepsilon A/d$, where A is the area of the metallic plates, d is the distance between the two metallic plates, and ε is the (complex) permittivity or dielectric function of the sample.

The frequency-dependent complex dielectric function of the sample may be defined as the ratio between the capacitance of the filled capacitor to that of the empty capacitor, given by $C_0 = \varepsilon_0 A/d$, where ε_0 is the vacuum permittivity. Hence one has:

$$\varepsilon(\omega) = \frac{C(\omega)}{C_0} = -\frac{i}{\omega Z(\omega)}\frac{d}{\varepsilon_0 A} \qquad (2)$$

While this simple scheme may be applied to measure bulk samples (whether in liquid or solid form), it is however unpractical for the measurement of thin-film samples. In fact, thin films may be obtained by deposition directly on a metallic disc to serve as an electrode; however, obtaining a capacitor configuration by either depositing a metal layer on top of the thin-film or by pressing a metal disk against the electrode with the thin film is, in most cases, not feasible.

For thin-film organic samples, in fact, deposition of a thick metal layer on top of the film is likely to lead to short-circuiting by percolation of the evaporated metal atoms through the film, and it also possesses the problem of obtaining a perfectly flat film in order to achieve a parallel-plate configuration. This approach is however used successfully in some cases, by careful layer deposition.On the other hand, simply sandwiching the film by pressing against it a second electrode is likely to result to damages to the film itself, and thus again to short-circuiting.

A more reproducible way to realize dielectric spectroscopy experiments on thin films, which has been implemented in this thesis, is to deposit an array of interdigital electrodesonto an insulating substrate, and depositing then the films on

top of the electrodes. This configuration is obviously distinct from a parallel-plate configuration, but it allows measuring on deposited films without touching them and leaving a free film surface. This implementation of dielectric spectroscopy is discussed in detail in Section (3.3).

3.1. Measuring Powder Samples

Figure(3.2):Powder sample

For dielectric measurement of polycrystalline solids (powders), the powder material is sandwiched between the two metallic plates, which are then inserted inside a Teflon ring.The Teflon ring is used both to prevent the powder to come out from between the disks, and also serves, during measurement, to prevent stray electric fields at the exterior edge of the capacitor.The cell is prepared by pressing the material between electrode plates by using hydraulic press, so as to obtain a pellet as compact as possible, with the powder crystallites (grain) in close contact to one another. The separation between both electrodes is determined by the pellet thickness, which can be measured by means of a calibration. The prepared capacitor is now carefully placed in sample holder and inserted in a cryostat where temperature is controlled by nitrogen-gas flow.

3.2. Measuring Liquid Samples

Figure (3.3): Liquid samples

For dielectric measurements of liquid samples, a home-made stainless steel parallel plate capacitor is used, equipped with a reservoir to contain excess sample. The sample is placed inside a hollow cylinder with only one base, that acts as the bottom electrode; a Teflon ring that fits tightly in the cylinder is then inserted, and finally, a second hollow cylinder with a single base is inserted inside the Teflon ring (see Figure 3.4, right panel). The base of the inner hollow cylinder serves as the upper electrode, and it has a small hole in the center so that excess liquid can flow upwards. The two hollow cylinders are separated by needle-like cylindrical silica spacers of 50 μmor100μm diameter. The capacitor is then loaded in sample holder and inserted in cryostat.

The scheme of the setup is shown in Figure 3.4.

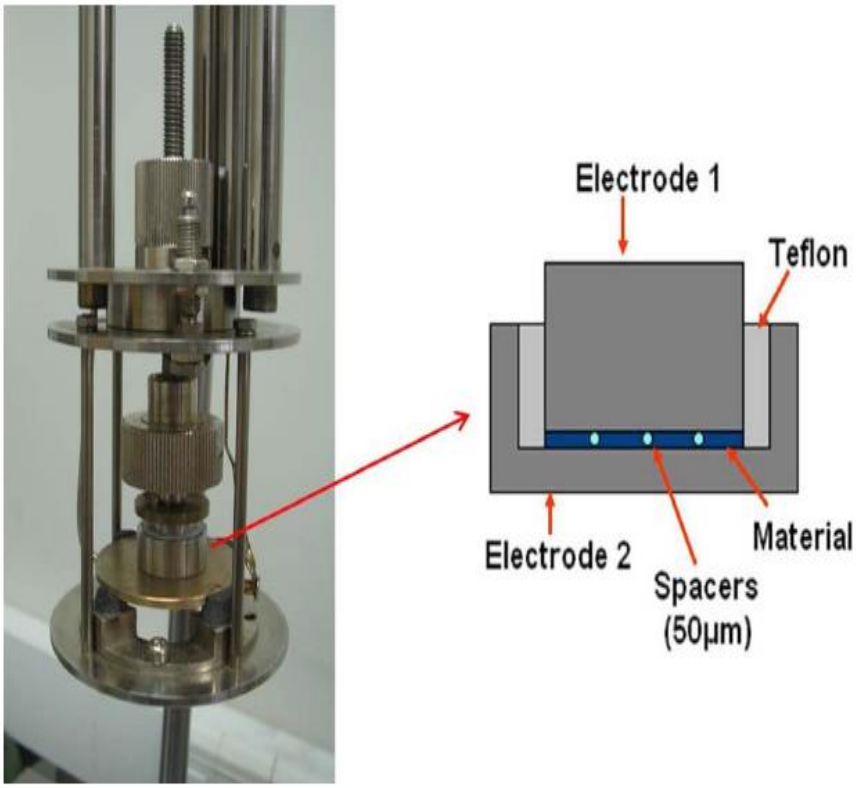

Figure(3.4): Sample holder with a scheme of the home-made capacitor used for measuring liquid samples

3.3.Measuring Thin Films

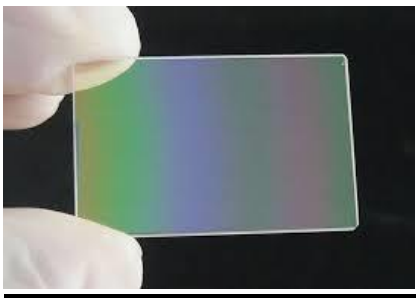

Figure (3.5): A thin-film sample

As mentioned in the introductory section of this Chapter, to measure the dielectric properties of thin filmsplanarInterdigitalElectrodes arrays are commonly used. Such Interdigital electrodes (IDE) generally consist of two comb-like metallic structures (displayed in blue and red color in the scheme shown in Figure 3.6), and havebroad range of sensing applications. The spacing between the comb fingers isSand their width is W,L is the finger length; the fingers have a relatively small height in the direction orthogonal to the plane of the figure (not shown).

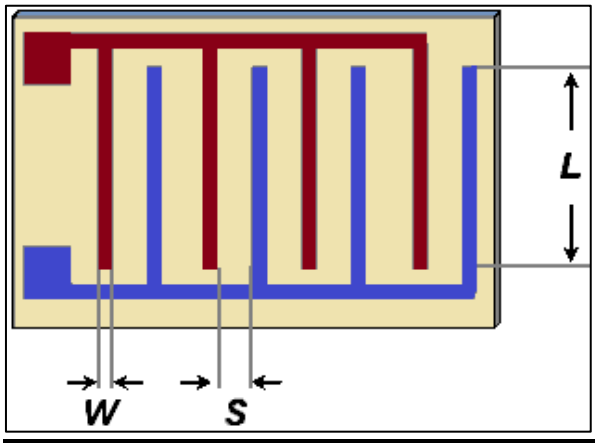

Figure (3.6):Layout of Interdigital Electrodes with finger spacing(S), width (W)and length (L)

Each metal comb acts asone electrode. The sample material is deposited on the finger structure. The height of the fingers is of the order of 100 nanometers, while the spacing S between them is of the order of 10 microns, so that the presence of the fingers does not affect the deposition of flat, 2D films. The interdigital finger configuration creates an electric field distribution which is mainly concentrated within a thin layer with thickness $D \approx S+W$ at the interface between substrate and sample material.They are therefore convenient to measure the dielectric properties of films of thicknesses ranging from one hundred nanometers up to several microns.

An important advantage of the IDE setup, already mentioned in the introductory paragraphs, isthat the upper surface of the sample remains free and can be used for additional (and possibly simultaneous) characterization like optical observations, scattering experiments, and for observing the effect of application of light pulses and gases onto the film, for example.The versatility of IDE allows a wide range of application without changing its fabrication design. For the purpose of dielectric spectroscopy, on the other hand, the more complex IDE geometry with respect to a parallel-plate capacitor requires more sophisticated calibration techniques, as detailed in Section 3.5.

3.4. Fabrication of Interdigital Electrodes

The multipurpose silicon based Interdigital electrode (IDE) devices were fabricated by a standard lithographic techniques **[1- 5]**. The substrate choice was silicon wafer, on top of which an insulating silicon oxide (SiO_2) layer was deposited. The metal used for the fingers was platinum, and an interfacial layer of Titanium was deposited to improve adherence of the platinum on top of SiO_2. The areas of the chip which are not used for external contacts or as IDE were passivated to avoid ageing and short-circuiting of the devices. We employed devices of two different geometries, with different spacing between neighboring fingers (respectively, 10µm or 15µm). The height and width of the fingers are approximately 160 nm (10 nm Ti + 150nmPt) and 10µm, respectively.The finger length L is 1.57mm for

10μmspacing and 1.54mm for 15μm spacing. The sum of the finger width and interfinger spacing is so-called structure size D, equal to 25μm and 15μm for 20μm and 10μm spacing respectively.

External contacts were made by soldering copper wires of 0.25mm diameter on the fabricated platinum electrodes. Before experiments, the Interdigital electrodes are cleaned by acetone with ultrasonic bath and then dried with the help of an air gun.

A scheme of a typical device is shown in Figure 3.7.

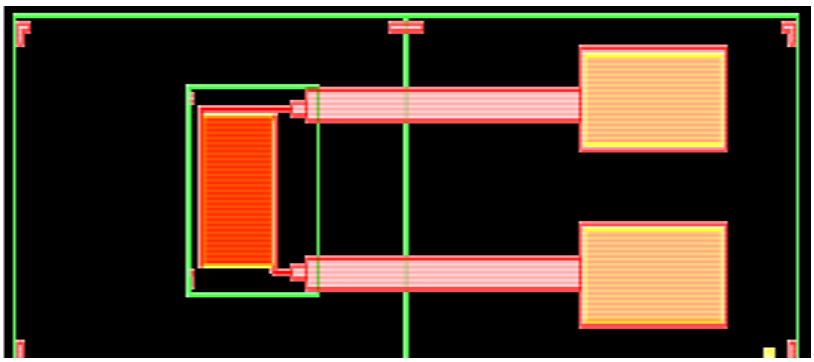

Figure (3.7):Geometry of an IDE including contacts

Figure 3.8 (a) is a photograph of a rectangular chip with two Interdigital Electrode devices, inserted on top of a sample holder. The screws visible in the top part of the picture allow to press gently, onto the area which is not used for external contacts,a Pt100 temperature sensor to measure the temperature of chip and thus of the thin-film sample(the temperature sensor is in the direct contact with the chip and is not visible in the photograph). Panel (b) of Figure 3.8 displays a micrograph image of a IDE device, with a close up to better observe the fingers.

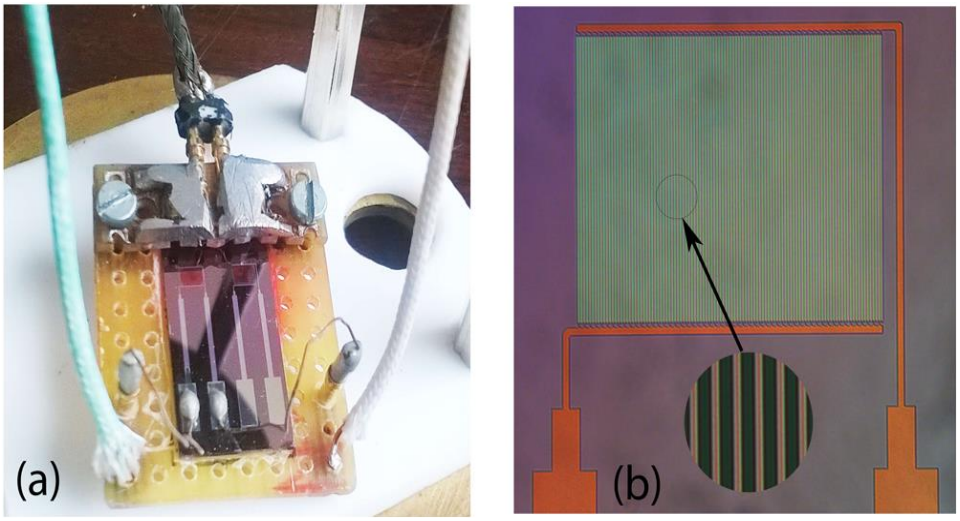

Figure(3.8): (a) Photograph of a silicon chip with two IDEs, mounted on a chip holder. (b) Micrograph of an IDE device

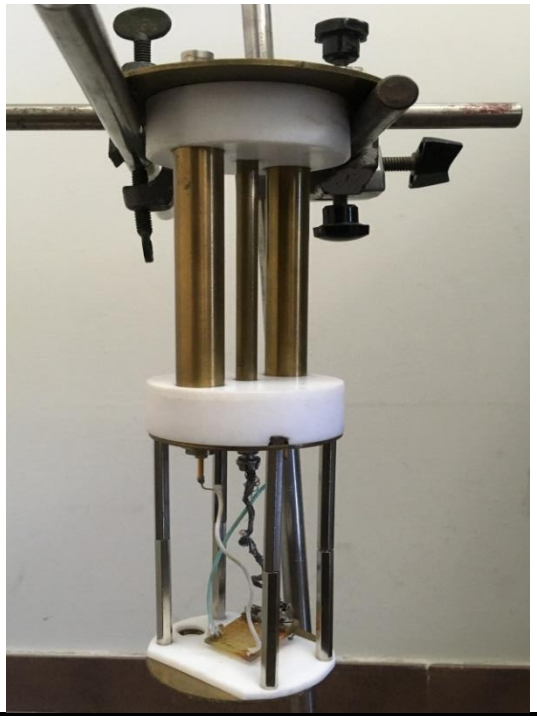

Figure(3.9): Sample holder for the chips carrying theinterdigital electrode devices

Figure (3.9) is a photograph of the complete sample holder for interdigital electrodes. The holder has the correct dimensions to fit inside the same cryostat used for "conventional" broad band dielectric spectroscopy measurements of bulk samples.

3.5. Calibration of Interdigital Electrodes

The IDEs have a geometrical capacitance C_0corresponding to the capacitance of the semi-infinite empty space above the IDE, **[2,9]** that is, one-half of the capacitance of the free-standing IDE electrodes in vacuum. Due to the presence of the Si/SiO_2 substrate (with relative permittivity εsubstrate) on oneside of the IDEs and of air or nitrogen (relative permittivity ε_r=1) on the other side, the actual capacitance of a device in air is given by:

$$C_0(1 + \varepsilon_{substrate}) \quad (3)$$

For calibration of C_0 and $\varepsilon_{substrate}$, we followed the procedure detailed in ref **[6],** using glycerol as the reference material (glycerol displays a very prominent relaxation peak at microwave frequencies below 273 K). Briefly, a drop of glycerol was spread over the IDEs to ensure that thestructure was fully covered. The thickness of the glycerol specimen was much higher than the structure size D of the IDEs, which as mentioned is roughly equal to the distance from the electrode array towhich the electric field of the IDE capacitor extends.**[7,8]** By subtracting the room-temperature spectrum of the pristine device from the experimental room-temperature spectrumacquired with glycerol, the contribution of the substrate tothe overall capacity cancels out, and C_0 is thus found as:

$$C_0 = \frac{(C_{with\ glycerol} - C_{empty})}{\varepsilon_{glycerol} - 1} \quad (4)$$

Here, $\varepsilon_{glycerol}$ = 42.5 is the value of the relative permittivity of glycerol at room temperature **[9].** The calibration also yields the value of $\varepsilon_{substrate}$, which turned out to be approximately 2.46, in agreement withthe expectation for SiO_2.**[10]** Moreover, the real part of thepermittivity of the empty IDE displayed a plateau value of 1.6, avalue close to unity and to half of the value of $\varepsilon_{substrate}$, confirming that the calibration procedure is adequate. The table given below shows the nominal value of C_0 for the two different IDE geometries, and also for a parallel-plate empty capacitor, for comparison purposes.

DEVICE	C_0
IDE (width=spacing=10μm)	15pf
IDE (width=spacing=15μm)	10pf
Parallel plate capacitor (plate separation=0.2mm)	17pf

The complex capacitance of an IDEs with structure size *D* ontop of which a film of thickness *t* is present, is given approximately by **[10]**

$$C^*_{\omega film}(\omega) = C_0\left[\varepsilon^*_{sample}(\omega)\frac{t}{D} + 1\frac{(D-t)}{D} + \varepsilon_{substrate}\right] \quad (5)$$

Here the term multiplying the factor of 1 represents the air or vacuum above the free film surface. By means ofEq. (5), the values of C_0 and $\varepsilon_{substrate}$ and the thickness *t* measured by profilometry could be employed to obtain the correct scale of the complex permittivity of the films from the experimentally measured complex capacitance. From this equation, it is seen thatthe imaginary permittivity may be simply obtained as:

$$\varepsilon^{"}_{sample}(\omega) = \frac{C^{"}_{with\ film}}{C_0}\frac{D}{t} \quad (6)$$

This procedure allowed us to obtain the correct scaling for bothdielectric loss and conductivity spectra using a simple scalingfactor equal to C_0t/D. In fact, the real part of the conductivity isrelated to the imaginary permittivity as $\sigma'(\omega) = \omega\varepsilon_0\varepsilon''(\omega)$, so that a common scaling applies to both quantities.

3.6.Comparison of the Empty Chip with Bulk Glycerol and with a drop of Glycerol onto an IDE Device

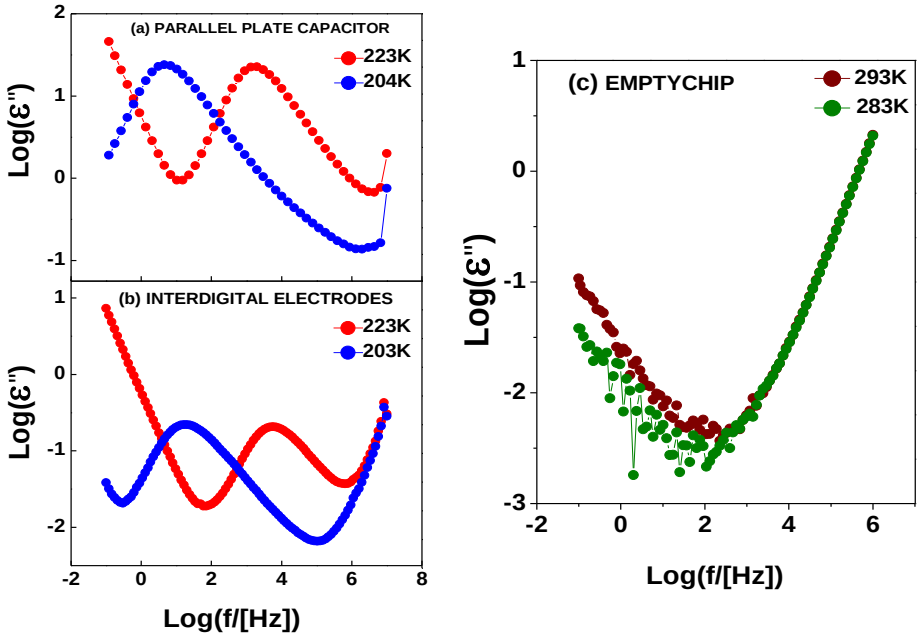

Figure(3.10):(a) Dielectric loss spectra of glycerol measured in the conventional parallel-plate capacitor geometry, at two temperatures (223K,204K), (b) Dielectric loss spectra of aglycerol drop on top of an IDE device, at two different temperatures (223K, 203K).(c) Dielectric loss spectra of the empty chip at 293 and 283K

Figure 3.10(a) represents the collective relaxation feature of glycerol at two different temperatures (223K and 204K), as measured with the home-made parallel-plate-like capacitor especially made for liquid samples (seeSection 3.2). Panel (b) of

the same figure represents the same relaxation measured with an IDE device of, where the fingers are fully covered by glycerol (to this aim, a drop of glycerol liquid is spread onto the interdigitated finger structure). Both measurements yield the same property of the reference material; the relaxation frequency at a given temperature is the same in both cases, which entails that our thin-film setup and calibration is correct.

Figure 3.10(c) shows the loss spectra of the empty IDE device, measured at two temperatures. The increase in the dielectric response above 10^3Hz (visible also in panel (b) of the same figure above 10^5 Hz) is the intrinsic temperature independent contribution of IDE to loss spectrum at high frequency, which is likely due to a self-inductance effect. Such increase in the background usually limits the experimentally available frequency range to below 10^4 Hz or 10^5 Hz unless samples with high dielectric loss strength are measured.

Bibliography:

[1] Z. Chen et al.,J.Phys. 85, 268 (2012)

[2] Antonia baldi et al., J.ElectroChem.8, 1239 (2006)

[3] S.K.Tripathi, Alka Monga and G.S.S.Saini, J.Smart materials and structures, 18,125012,(2009)

[4] M.ALomillo Alonso,J.Gonzalo-Ruiz, F.PascualMuñoz, Biosensor Based on Platinum Chips for Glucose Determination. Anal.Chim.Acta, 547, 209−214,(2005).

[5] O.Laczka,E.Baldrich, X.F.Muñoz,F.J.delCampo,Detection of Escherichia Coli and Salmonella Typhimuriumusing Interdigitated Microelectrode Capacitive Immunosensors: The Importance of Transdu. Geometry.Anal.Chem.,80,7239–47,(2008).

[6] Z.Chen,A.Sepulveda, M.D.Ediger, R.Richert,Dielectric Spectroscopy of Thin Films by Dual-Channel Impedance Measurements on Differential Interdigitated Electrode Arrays. Eur. Phys. J. B, 85, 268,(2012).

[7] P.vanGerwen, W.Laureyn, W.Laureys,G.Huyberechts, M.op de Beeck, K.Baert,J.Suls, W.Sansen, P.Jacobs, L.Hermans, et al. Nanoscaled Interdigitated Electrode Arrays for Biochemical Sensors. Sens. Actuators, B,80,49-73,(1998),

[8] F.Starzyk,Parametrisation of Interdigit Comb Capacitor for Dielectric Impedance Spectroscopy. Arch. Comput. Mater. Sci. Surf. Eng.,34,31−34,(2008).

[9] P.LoidlLunkenheimer A. Dielectric Spectroscopy of Glass-Forming Materials: α-Relaxation and Excess Wing. Chem. Phys., 284, 205−219,(2002).

[10]Schaumburg,G.NovocontrolDielectrics Newsletter.http://www.novocontrol.de/newsletter/DNL22.pdf, Vol. 22, 5−8, (2006).

CHAPTER 4

Dielectric Studies of Organic and Hybrid Thin Films deposited by Three Different Techniques

4.1. Introduction

Dielectric spectroscopy (DS), also known as impedance spectroscopy, is one of the most versatile experimental techniques to probe the electric and dielectric response of materials. The broad frequency window accessible with this technique allows probing in a single experiment both the electrical conduction properties and the molecular orientational dynamics of polar or ionic samples, such as are many organic molecular solids.**[1]** In conventional DS measurements, the samples are liquids or pellets obtained from melts or by pressing granular powders, and the measurement is carried out in a parallel plate capacitor configuration. From an applied point of view, however, the suitable material form for, for example, electronic or optoelectronic devices, is the thinfilm form, which cannot be studied using this conventional geometry. Moreover, the microstructure, molecular dynamics, and electrical properties of a thin film are in general different from those of the bulk material due to interaction between the film and the substrate**[2,3]** and also, if the film thickness is very small, to confinement effects.**[4,5]**

Not only the knowledge of the properties of the bulk material is sufficient to predict its behavior in thin-film devices, but also most importantly, the specific features of the thin-film form are often an added value that allows different and more variedapplications than the bulk system. Some crystallographic or stoichiometric phases of materials may, for example, only be obtained in thin-film form and not as bulk phases.**[6,7]** A recent confirmation of the peculiarity of the thin-film form of organic systems is the discovery that thermally evaporated films of glass-forming materials grown below the glass transition temperature exhibit enhanced stability with respect to thebulk glass.**[8−12]** The main experimental tool that has been employed to characterize such ultrastable thin-film glasses, besides calorimetry, is

an implementation of DS suitable for thin films based on interdigital electrode (IDE) arrays.**[13]**Compared with the conventional parallel capacitor geometry,IDE-based DS is, in general, limited to a smaller frequencyrange due to a chip-induced background at high frequency thatis independent of temperature and usually limits measurements to below 10^4 or 10^5 Hz unless samples with high dielectric lossstrength are measured.**[13]**We show here that the application of DS to thin organic films has useful applications outside of the field of ultrastable glasses and, more in general, can yield valuable information about the fundamental properties of organic materials such as their conductivity, charge-transport mechanism, and dielectric response and about molecular degrees of freedom and dynamics. This is particularly interesting because some basic intrinsic electric properties of materials, such as their dc conductivity and their static permittivity, cannot be measured in the parallel plate geometry on pellets obtained by pressing granular powders due to the inherent inhomogeneity and air content of such samples. Instead, we show here that information about intrinsic material properties can be obtained with IDE-based DS, which is the more valuable as it is relevant to their thin-film form and thus directly applicable to thin-film device performance.

Here we apply thin-film DS to small-molecule films deposited in three different ways. We study in particular thin films of two dyes belonging to the rhodamine family, namely rhodamine 6Gchloride films grown by spontaneous assembly from solution, thermally deposited rhodamine 19 films (in its zwitterionic form) in vacuum, and Langmuir-Blodgett films of cadmium iodide ethylamine covalently attached to an octadecylamine-hydroiodide surfactant.

Rhodamine 6G chloride, of chemical formula $C_{28}H_{31}N_2O_3Cl$ (molecular weight=479.02g/mol),is used as a laser dye and as tracer dye in liquid solutions to determine the rate and direction of flow and transport. It has also extensive applications in biotechnology such as fluorescence microscopy, flow cytometry, fluorescence correlation spectroscopy.

Its molecular structure is shown in panel (a) of Figure 4.1, while that of the related rhodamine 19 molecule is shown in panel (b).

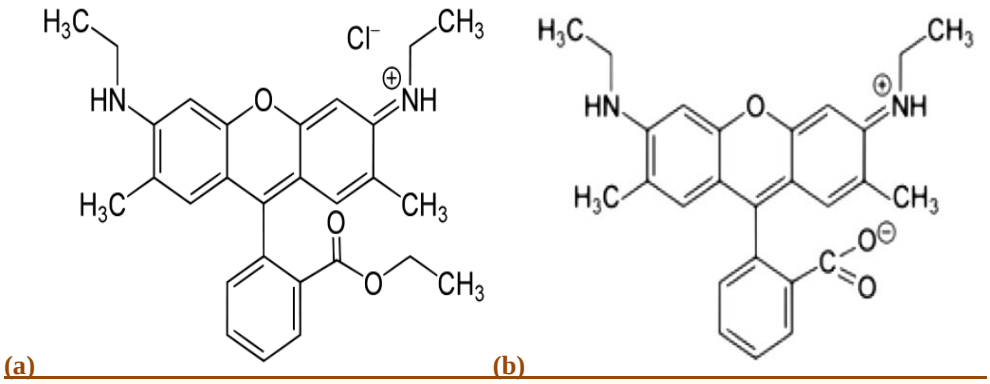

Figure (4.1): Molecular structures of Rhodamine 6G(left) and Rhodamine 19 (right).

As it is observed, while Rhodamine 6G is a cation that forms a chloride salt, rhodamine 19 is a neutral, zwitterionic molecule with no chlorine counter-ion.

The structure of a bilayer of the hybrid (organic-inorganic) molecule made of cadmium iodide ethylamine (CdI_2EA) covalently attached to octadecylamine-hydroiodide (ODA) is shown schematically in Figure 4.2. We will refer to the complex as ODA-CdI_2EA.

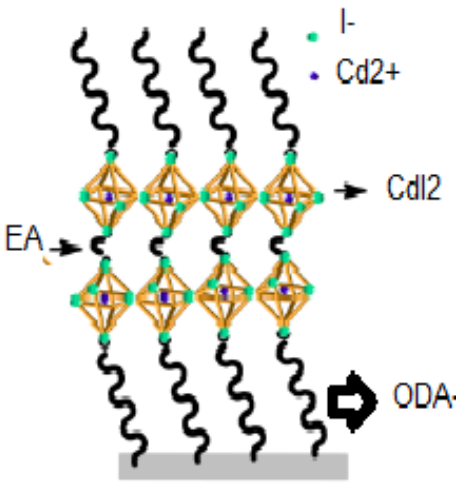

Figure (4.2): Schematic structures of a bilayer Langmuir-Blodgett film of ODA-CdI_2EA (the substrate is shown in gray).

Perovskite-based organic-inorganic hybrids prepared through layer-by-layer deposition hold great potential for many applications in low-cost, low-weight, flexible electronics and optoelectronics, and as components of biosensors or catalysts. [**14-18**]Many of these applications require controlled thin-film growth.Recent interest in such hybrid films includes for example their possible applications for sensitised solar cell devices. In fact, solar cells with relatively highefficiency (9%)were recently demonstrated, based on the inorganic-organic hybrid perovskite (CH_3NH_3)PbI_3.**[19-21]**Among hybrid organic-inorganic materials, crystalline materials which comprise layers of organic molecules alternating with inorganic sheets have been widely studied due to their potential application in integrated devices**[22-24]**.Langmuir-Blodgett thin films of ODA-CdI_2EA were grown to study how the thin-film geometry modifies the properties of CdI_2EA. The Langmuir-Blodgett films were grown by collaborators of the Surfaces and Thin Films Group of the Zernike Institute for Advanced Materials of the University of Groningen, in the Netherlands.

The aim of this chapter is to show that IDE-based dielectric spectroscopy can be employed on thin films of organic and hybrid systems, deposited by a wide range of

methods (immobilization from solution, thermal evaporation, Langmuir-Blodgett deposition), and that interesting differences are in general found with respect to the bulk form of the same materials.

4.2. Experimental Details

As mentioned in Section 4.1, two different methods havebeen used for depositing the rhodamine thin films. They were actually obtained using the same starting material, namely, rhodamine 6G (Rh6G) powder; in fact, as will be clear from the results shown in this chapter,immersion in solution and thermal evaporation yield films with quite different properties.Solution-deposited films were prepared by immersion of the silicon-based chips (IDEs) in 10^{-3}M Rh6G solutions in ethanol.A Rh6G chloride film formed spontaneously upon immersion due to the electrostatic interactions between the substrate, cations, and counterions. The chips were retrieved carefully from the solution to avoid the formation of drops that could result in inhomogeneity, and the film thickness was determined by profilometry.

Thermally evaporatedfilmswere prepared by vapor deposition onto the chip (at room temperature) using a commercial vacuum deposition system for organic powders, with a base pressure of 10^{-7}mbar. The deposition rate was kept at 1Å/s by controlling the temperature of the Knutzen cell (approximately 420 K), which contained Rh6G powder. Upon sublimating, the Rh6G chloride powder decomposed into rhodamine 19 (Rh19), which then condensed to form Rh19 thin films.

The typical thickness of solution deposited Rh6G chloride filmswas 130nm, while the thickness of thermally deposited Rh19 films was set to 300nm.

Preparation of LB films of ODA-CdI_2EAwas accomplished using a NIMA Technology Langmuir Trough 5. For all the experiments, the sub phase was prepared in 2 liters of purified water at room temperature. The ODAH+I- mixtures were dissolved in 9:1 chloroform/ethanol and deposited onto the surface of subphase of CdI2+EA by means of a microsyringe to form monolayer film at the air-water interface. It took about 30min for the solvent to evaporate and to achieve

equilibration of the film; the film wasthen compressed by the trough barriers. The pressure was stabilized at around 30 mN/m before deposition. The barriers were computer-controlled so that uniform compression of the film and constant feedback can be achieved when depositing monolayers. The surface pressure was measured with a Wilhelmy plate interfaced to a personal computer. The ODA-CdI_2EAfilms were deposited vertically onto substrates at 30 mN/m upon first compression. For deposition we set 120 sec and 60 sec dipping time for the up and down strokes, respectively. The films were grown directly onto the chips with the IDE devices.The deposited silicon based IDEs were then carefully placed in the sample holder (explained in Chapter 3), which was then inserted inside the cryostat where the sample temperature was controlled by nitrogen flow.

The experimental loss spectra (imaginary part of the permittivity) were fitted as the sum of one or moreHavriliak-Negami functions (Cole-Cole functionsfor the CdI_2EA samples), each representing a dielectric loss feature, on top of a low-frequency conductivity background proportional to inverse frequency. From the fit the value of the relaxation time is obtained, which is then plotted as a function of the inverse temperature (Arrhenius plot).
The loss spectra and real conductivity spectra are related as:

$$\sigma`(f) = 2\pi f\varepsilon_0\varepsilon``(f) \qquad (1)$$

so that the same information is actually contained in both spectral representations. The value of the dc conductivity (σ_{dc}) was obtained as the plateau value of the real part of the complex conductivity of the sample at low frequency.
The film thickness was used for calibration of the vertical scales of the real and imaginary part of the permittivity (see Chapter 3).

4.3.Dielectric Relaxations in Rh6G and Rh19Films

Dielectric measurements were carried out by Novocontrol Alpha analyzer between 130K to 475 K in the frequency range from 10^{-1} to 10^{6} Hz, both on thin films using IDE-based DS, and on the Rh6G powder by conventional capacitor (parallel plate capacitor).The typical loss spectra (imaginary part of the permittivity)of both solution and thermally deposited rhodamine thin films are shown in Figure 4.3.

Panels (a) and (c)display the spectra of a 130nm thick film grown by immobilization from an ethanolsolution, while panels (b) and (d) show the spectra of a 300 nmthick vacuum-deposited film obtained by thermal evaporation.The spectra of panels (a) and (b) (temperatures between 383K and433 K) are characterized at low frequency by a line shapeproportional to reciprocal frequency, which represents the dcconductivity of the film, followed by a relaxation featureat intermediate frequencies (between 10^{1} and 10^{3} Hz). At lowertemperatures (panels c and d), a dipolar loss feature is observed in solution-deposited films, which is absent in thermally deposited ones. The increase above 10^{3} Hz in panel d is observed also in the dielectric response of the empty chipand represents the intrinsic temperature independent contribution of the IDE to the loss spectrum at high frequency. For more details referto Chapters2 and 3.

We will show in the next Section that the high-temperature relaxations are conductivity-induced losses (both in the case of Rh6G and Rh19 films). In the remainder of this Section we discuss instead the origin of the low temperature feature in the Rh6G chloride films.

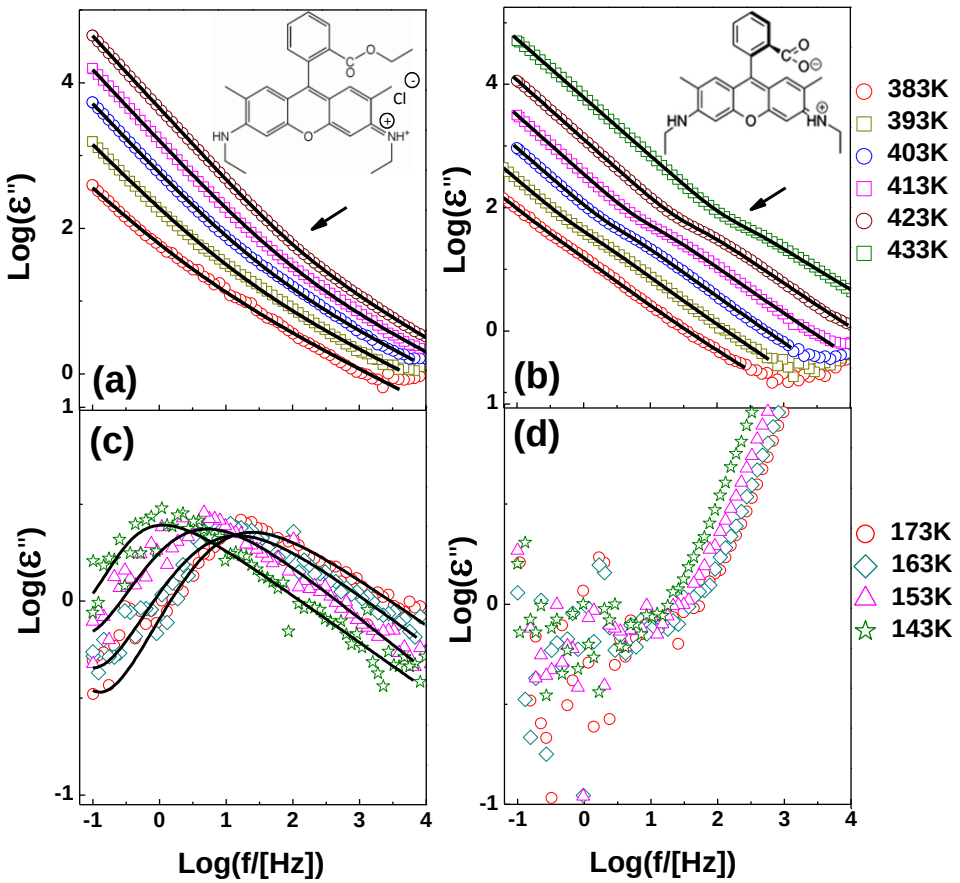

Figure (4.3): Dielectric loss spectra of solution-deposited Rh6G films (a,c) and of thermally evaporated films (b,d). The loss spectra were measured in two different temperature ranges (see legends). Markers are experimental points, continuous black lines are fits to extract the frequency of the loss maximum and arrows indicate the position of the high-temperature loss features (BNN relaxations) and their variation with temperature.

Rh6G, whose molecular structure isshown in Figure (4.1(a)),is a chloride salt, and the solution-processed films are ionic as the Rh6G powder (they contain both Rh6G cations and chlorine counterions), and display a high degree of order especially in the first molecular layers.**[25,26]** On the other hand, vacuum-deposited films are deposited via sublimation of powder in vacuum, do not contain chlorine,**[27]** and appear to be amorphous.**[28]** The thermally deposited films consist of a neutral

rhodamine molecule, namely, the zwitterionic form of rhodamine 19(Rh19), which has a slightly different molecular formula than Rh6G shown in Figure (4.1(b)).

In fact, we observed by thermogravimetry analysis(TGA) that under a nitrogen atmosphere, Rh6G undergoes a mass loss just below the temperature of melting and simultaneous decomposition (483 K).**[29]** The observed mass loss (roughly 11%) corresponds to the loss of a Cl counterionand an ethyl group(-CH_2CH_3) per Rh6G molecule, or equivalently by a Cl_2 and a C_4H_{10} molecule every two Rh6G units, consistent with the chemical formulas of Rh6G and Rh19.**[27-29]**As a consequence, upon sublimation in vacuum chlorine gas separates from the rhodamine cation so that thermally evaporated films actually consist of a slightly distinct, neutral rhodamine species.

Since the high-temperature feature is a conductivity-induced loss, the loss feature visible at low temperature (Figure 4.3(c))must have a different origin, i.e., it muststem from the relaxation of a dipolar unit. Since both the Rh6G cation and the Rh19 zwitterion possess a non-zero dipole moment, if the two species were capable of whole-molecule reorientations in their respective films, one would observe a relaxation in both samples; instead, a dipolar relaxation is only found in Rh6G.In view of the above-mentioned differences between the two types of films, it is natural to assign the low-temperature, faster relaxation to are orientational motion of the intramolecular dipole associated with the Cl counterion and the positively charged nitrogen atom of the Rh6G cation. Such intramolecular dipole moment is obviously absent in thermally evaporated films, where the chlorine ions are missing. This interpretation rationalizes why the low temperature relaxation is absent in Figure 4.3(d), despite the fact that thecorresponding film is more than twice thicker than that of panel (c).

We have carried out a study on pellets made of the Rh6G chloride powder. Figure 4.4 shows the Arrhenius plots of characteristic relaxation timeof all relaxations present in both bulk and thin films. The Rh6G powder exhibits hygroscopic behavior, and in fact two relaxations are observed in this material **[29]**,displayed by open orange circles, which are due to the presence of hydration water at theRh6G grains' surface. We will not be concerned here with these water-induced features.As

visible in Figure 4.4, the bulkmaterialdisplays two intrinsic relaxations(blue closed circles). The slower one lies in the neighborhood of the slow relaxation observed in both rhodamine films, and as shown in thenext section it is a conductivity-induced feature as the latter ones. The Rh6G powder exhibits a faster relaxation feature, more or less in the temperature range of the intramolecular dipole relaxation of Rh6G films associated with the chlorine counterions. The dynamic behavior of this feature is actually slightly different from that of the low-temperature thin-filmfeature of Figure 4.3(c).

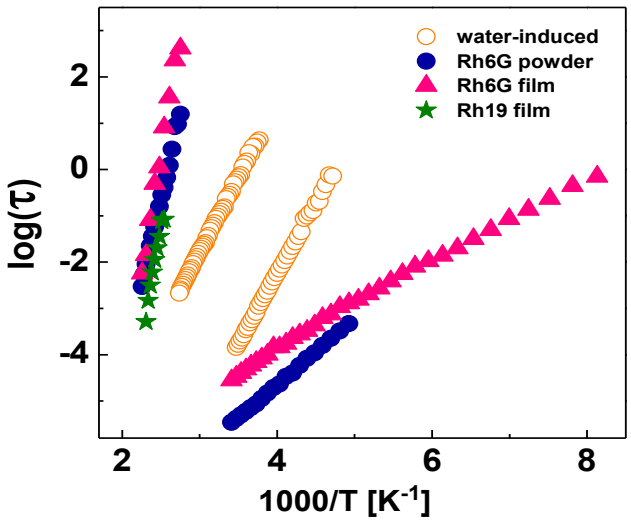

Figure (4.4): Arrhenius plot of the relaxations observed in solution-deposited films (pinktriangles) and of the single relaxation present in Rh19 films (green stars). For comparison, the relaxation times observed inthe hydrated Rh6G powder are also shown; two of the four relaxations are due to surface hydration water (open orange circles), while the other two are intrinsic to Rh6G (filled blue circles)

The activation energies of low temperature relaxations associated to the intramolecular dipole with chlorine counterions has quite different activation energy in the (solution-deposited) Rh6G films than that in the Rh6G powder. The activation energy is 17.9 kJ/molin the films and 27.3 kJ/mol in the pellets, that is, more than 50% higher in the latter. It is likely that the relatively looser molecular

environment in the film (with respect to the bulk polycrystalline powder) results in a lower activation energy for the motion of the local dipole moment involving the chlorineion and nitrogen moiety, as observed.

On the other hand, theactivation energies of the high-temperature relaxations are 143kJ/mol in the pellet, **[29]** 180 kJ/mol in thermally evaporated films, and 198 kJ/mol in solution-deposited films. The relatively small variation of the activation energy (≤25%) and the very similar values of relaxation times in the bulk and thin-film formsconfirm the common origin of these relaxation. In the next section we show that this common origin is a conductivity-induced space-charge relaxation.

4.4.Conductivity Properties ofRh6G and Rh19 Films

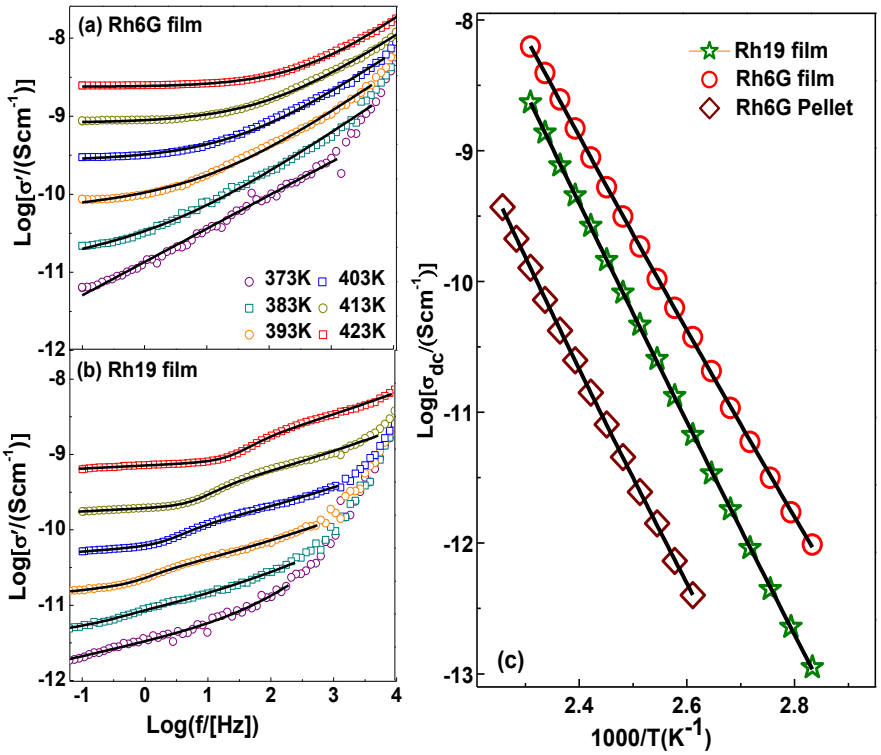

Figure (4.5): Conductivity spectra of Rh6G (a) and Rh19 (b) films between 373 and 423 K, corresponding to the data of the upper panels of Figure 4.3. Markers are experimental points,and continuous lines are fits. (c) Arrhenius plot of the dc conductivity of both films and of a water-free Rh6G pellet.

The steady increase with decreasing frequencyin the loss spectra of panels (a) and (b) of Figure 4.4corresponds to the contribution from dc conduction. This is best visualized in the ac conductivity spectraσ`(*f*) shown in figure 4.5 (panels(a) and (b)) for both Rh6G and Rh19 films, respectively (the data correspond to those of the upper panels of Figure 4.3).We extractedthe dc conductivity as the low-frequency plateau value in the spectra of the left-hand panels of Fig. 4.5, and displayed it as Arrhenius plot in panel (c). The σ_{dc} value increaseswith increasing temperature,

implying that the conductivity is thermal-assisted as it is commonly the case for semiconducting materials.

The Arrhenius plots of the dc conductivity for bulk Rh6G (open squares), Rh6G films (open circles), and Rh19films (open stars) all exhibit a positive curvature, which proves that the conductivity in all rhodamine samples is due to hopping of electronic species.**[30−32]**Indeed, such plots could be fitted with a power-law temperature dependence of the form $\log(\sigma_{dc}) = A - (B/T^{n})$. The values of the power-law exponent *n* were all lower than one, in agreement with the prediction of variable-range hopping (VRH) models of electronic chargetransport.**[30,31]**In particular,*n* was 0.66 for Rh19 films and 0.52 for Rh6G films. Both values are close to the value of 1/2 observed in many systems, ranging from metal−cluster compounds and granular and ceramic metals to doped or amorphous semiconductors and thin films,[**30,31,33,34]** which corresponds to charge hopping in a landscape characterized by a quadratic energy dependence of the local electronic density of states.**[35]** On the other hand, for the pellet, *n* was 0.27, close to the theoretical value of 1/4 that corresponds to Mott's original formulation of VRH assuming an energy-independent (flat) electronic density of states.**[35]** The distinct value of *n* would thus suggest that the difference in morphology between the films and the polycrystalline pellet leads to differing effective local density of electronic states. We point out that the nature of conduction in rhodamine could instead not be identified in a previous study on a Rh6G pellet with conventional DS. **[36].**

As may be gathered from panel c, the conductivity of the pellet made by compressing the Rh6G powder is significantly lower than that of either type of film, and it is lower than the conductivity of the Rh6G film. This may be expected because the pellets are not homogeneous but rather contain grain boundaries (and possibly air gaps), which decrease the overall conductivity of the sample. At the lowestmeasured temperature, the dc conductivity is roughly 1 order of magnitude higher in the Rh6G film than inthe Rh19 one. This difference may also be expected because solution-deposited Rh6G films are well ordered (at least forsmall thickness)**[25]** while thermally evaporated Rh19 films are amorphous**,[28]**and the

degree of crystallinity is known to havea profound impact on the conductivity of organic (as well as inorganic) films.**[37]** It is worth pointing out, also, that the difference in conductivity becomes smaller at higher temperature. This may be rationalized because thermal motions become more and more important as the temperature is raised, likely leading to an effective disorder that limits the hopping rate.

We can now identify the origin of the slow relaxation present in all samples (see Figure 4.4). Figure 4.6 shows the comparison between the Arrhenius plots of σ_{dc} and f_{max} of the slower relaxation, for both Rh6G (a) and Rh19 (b) films.It may be observed that the temperature variation of both quantities is virtually identical in both films. To better visualize this correlation, the two quantities are plotted in linear scale in the respective insets. The frequency f_{max} is actually multiplied by a constant times the dielectric strength $\Delta\varepsilon$ of the slow relaxation, to test the validity of the so-called Barton-Nakajima-Namikawa (BNN) relation [**38,39]**, according to which a conductivity-induced loss feature should obey the condition:

$$\sigma_{dc}=p\ 2\pi\varepsilon_0\ \Delta\varepsilon f_{max} \qquad (2)$$

In Eq.2, p is a constant of order unity. As visible in the insets to Figure 4.6, theBNN relation indeed holds for both Rh6G (a) and Rh19 (b) films.Analogous results are obtained for the pellets made of Rh6G powder (not shown).

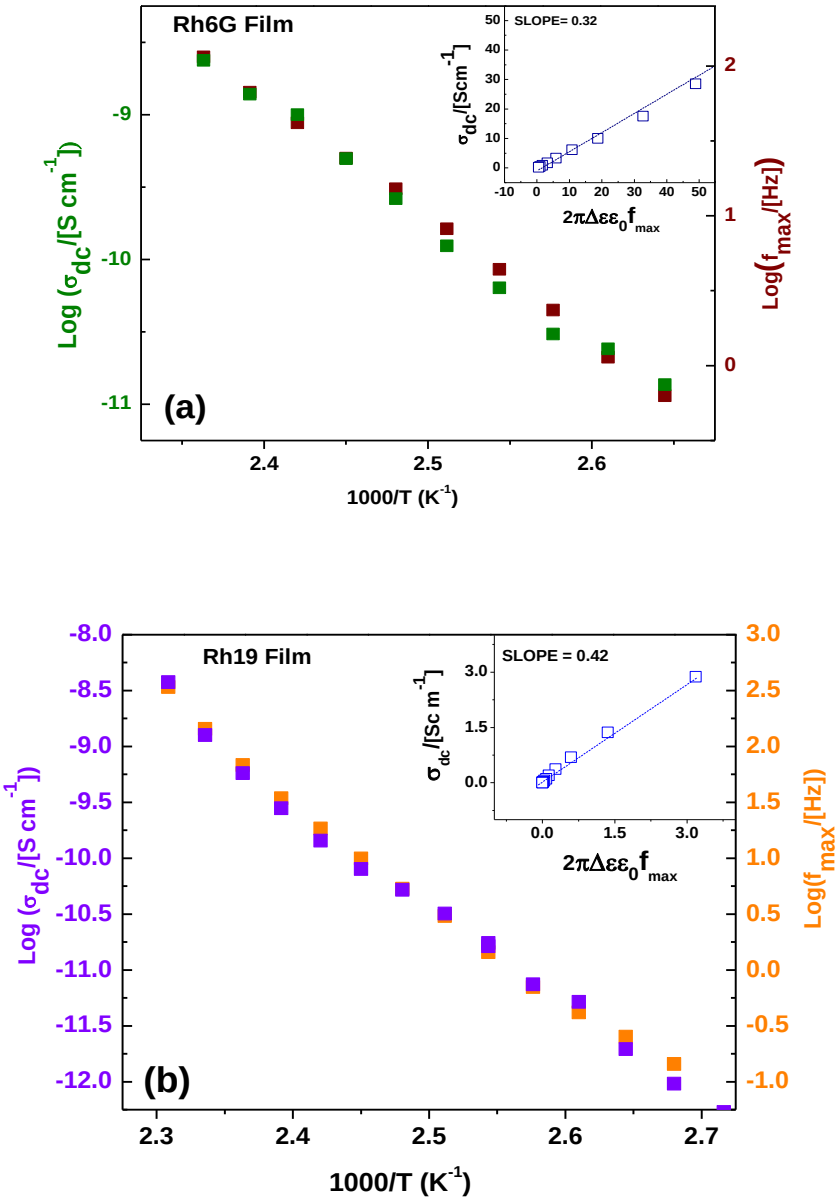

Figure (4.6): Arrhenius plot of dc conductivity (σ_{dc}) of compared with relaxation frequency (f_{max}) for both Rh6G (a) and Rh19 (b) films.The vertical scales in each panel span the same number of decades. The insetsare linear plots of f_{max}*versus*$\sigma_{dc}$to test the validity of theBNN relation.

The validity of the BNN relation for the slow relaxation observed in all samples indicates that it such slow process is a conductivity-induced loss feature due to

theaccumulation of electronic charge carriers at sample's heterogeneity such as grain boundaries (pellet) or domain boundaries (films).

(4.5) Preliminary Characterization of Bulk CdI_2EA by DSC and XRD

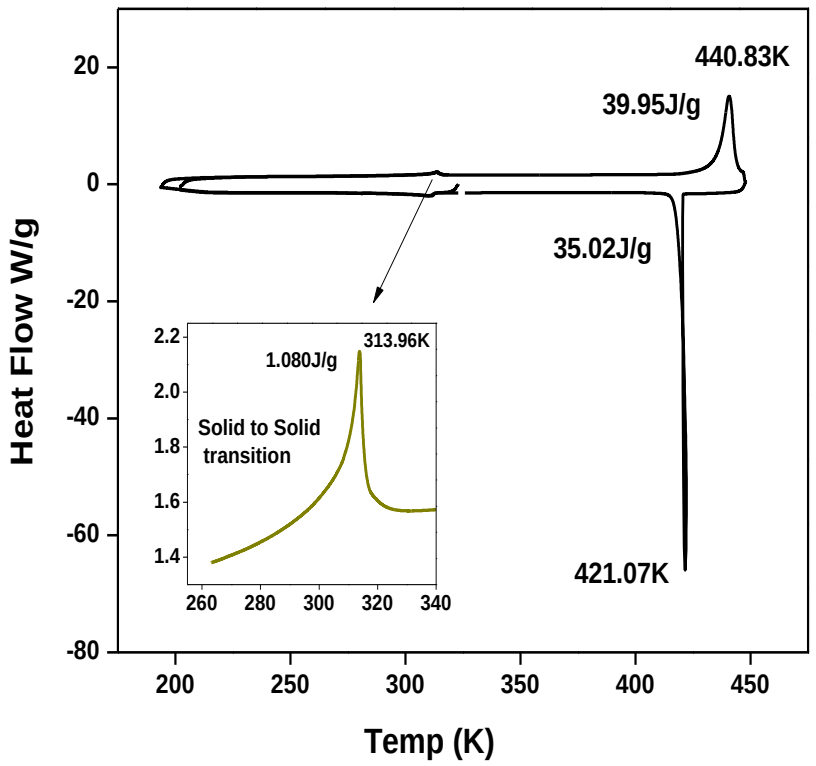

Figure(4.7):DSC thermogram of the CdI_2EA powder. Two transitions are observed. For each, the graphical calculation of transition temperatures and transition enthalpies is shown.

Figure 4.7 shows the calorimetry thermogram of the CdI_2EA powder.A solid-solid phase transition is observed just above room temperature, and melting is observed at higher temperature. According to the X-ray diffraction results displayed in Figure

4.8,the lower-temperature endothermic phase transition is a solid-solid structural phase transition involving a significant change in structure. The transition temperature is 314K, with a latent heat of 1.080 J/g. The melting temperature is 441K, and the associated latent heat is 39.95J/g. The transitions are reversible, implying that the material does not decompose upon melting, and that the structure of the high-temperature solid phase is recovered when the material crystallizes from the melt (at 421K, with hysteresis of 18 K). The solid-solid transition exhibits a small hysteresis of less than 4 K. It is observed that there is no visible signature of crystallization or evaporation of water, implying that the LB films do not contain any residual water.

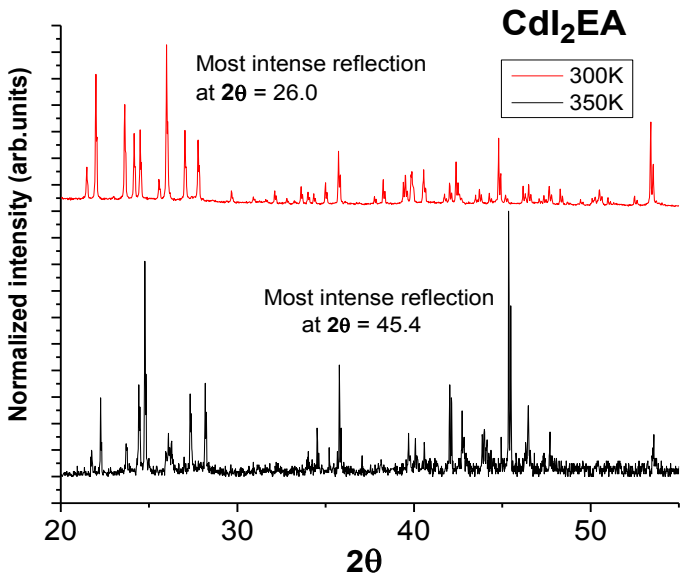

Figure (4.8): XRD patterns of the CdI_2EA powderat 300 K and 350 K, i.e., below and above the solid-solid transition temperature. A clear modification of the XRD peaks is observed.

4.6.BDS Study of bulk CdI_2EA and Langmuir-Blodgett films of ODA-CdI_2EA

Dielectric spectroscopy measurements were carried out both on a Langmuir Blodgett (LB)film of ODA-CdI_2EA,measured with the chip setup, and bulk samples of CdI_2EA,obtained by cooling the CdI_2EA melt directly inside the capacitor especially designed for BDS characterization of liquid samples, and measured directly.The LB film had 6 layers and nominal thickness 17.1 nm (the latter value was used for calibration, see Chapter 3)

Figure 4.9 shows the isothermal ac conductivity spectra $\sigma`(f)$ of bulk CdI_2EA(upper panel) and of the LB film (lower panel). The $\sigma´(f)$ spectra display a plateau at low or intermediate frequency, from which the dc conductivity value (σ_{dc}) is obtained.In both series of spectra a phase change is visible as a variation of spacing between the spectra.

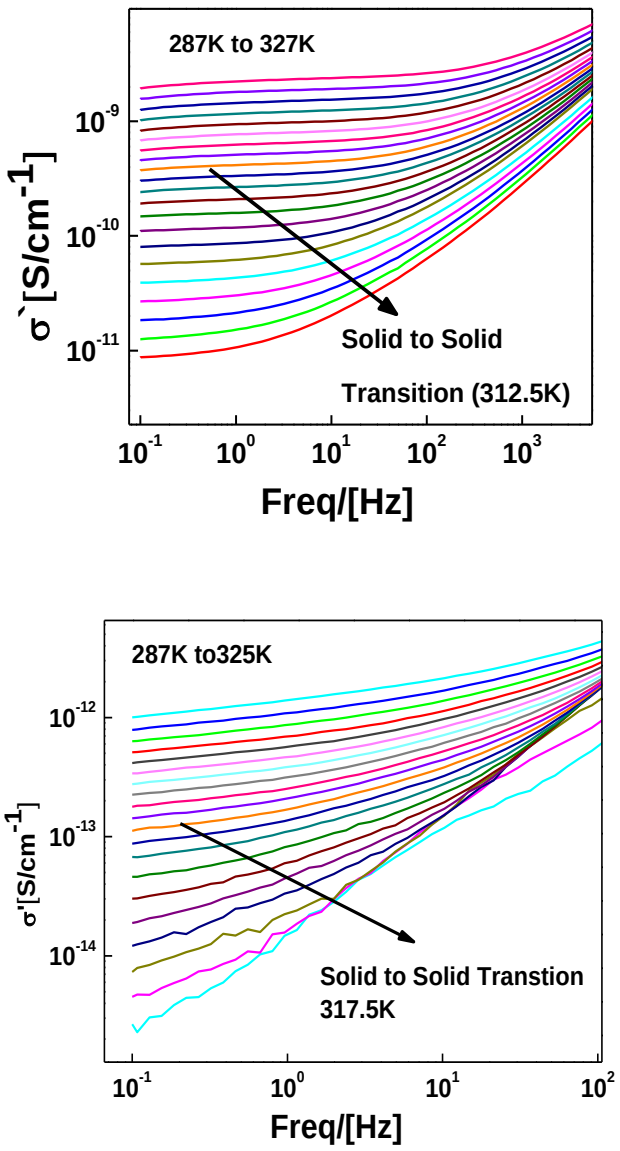

Figure 4.9: Comparison of isothermal ac conductivity spectra ($\sigma`(f)$) of bulkCdI_2EA(upper panel) and of a film of ODA-CdI_2EA(lower panel). Subsequent spectra were measured upon increasing temperature. In both series of spectra, a phase change is visible as a variation in vertical spacing between the spectra.

Figure 4.10 shows the Arrhenius plot of σ_{dc} for both samples of Figure 4.9. The phase transition is visible as a cross-over from a higher to a lower activation energy (change of slope in Figure 4.10). The change in temperature dependence can also be observed directly in the ac conductivity spectra.

The transition temperature in the bulk sample is 312.5 K, comparable to the one detected by DSC (314 K). The transition temperature in the LB film is higher by roughly 5 K than that of the bulk. This difference might be due to the different chemical composition or structure of the film sample.

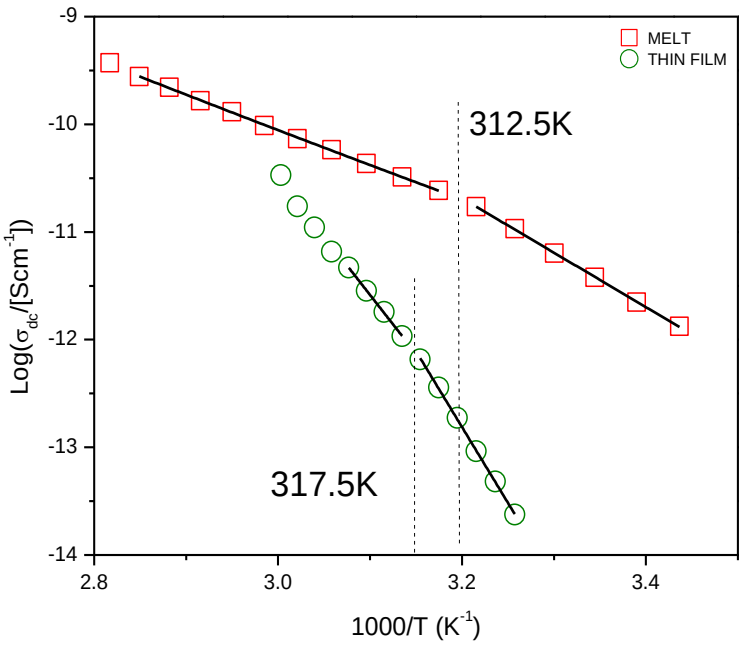

Figure (4.10): Arrhenius plot of dc conductivity (σ_{dc}) for both samples (data of Figure 4.9). Continuous lines are fits with the Arrhenius equation in different temperature ranges (above and below the solid-solid transition).

The phase change in the thin film is also visible from the spectra of the real part of the permittivity, shown in Figure 4.11 for the bulk sample.The spectral increase at low frequency is due to a conductivity effect (electrode polarization, i.e., the

accumulation of charges at the sample-electrode interface). The vertical scale is less reliable than that for the loss spectra.

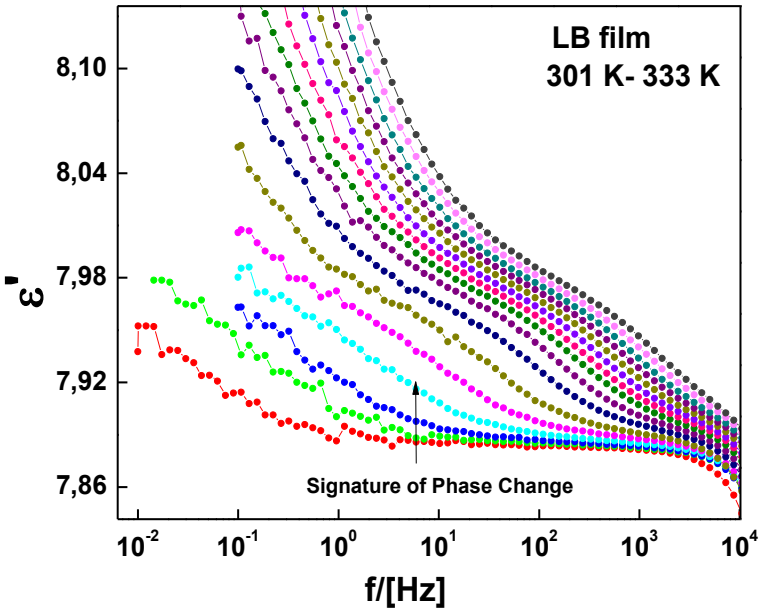

Figure (4.11): Isothermal dielectric function (ε`(*f*)) of the bulk CdI_2EA powder, measured upon heating.

Figure 4.12 shows a series of loss spectra (imaginary part of the complex permittivity, ε``(*f*)) on the LB film. Thespectra show the existence of a clear relaxation process, visible as a peak between 10^{-1} and 10^{3} Hz.(The more pronounced peak around 10^{5} Hz or 10^{6} Hz is instead intrinsic to the empty chip, and it is due to a self-inductance effect see Chapter 3). The relaxation peak shifts to higher frequency as the temperature of the isothermal spectra is increased, as expected for a dipolar molecular relaxation.

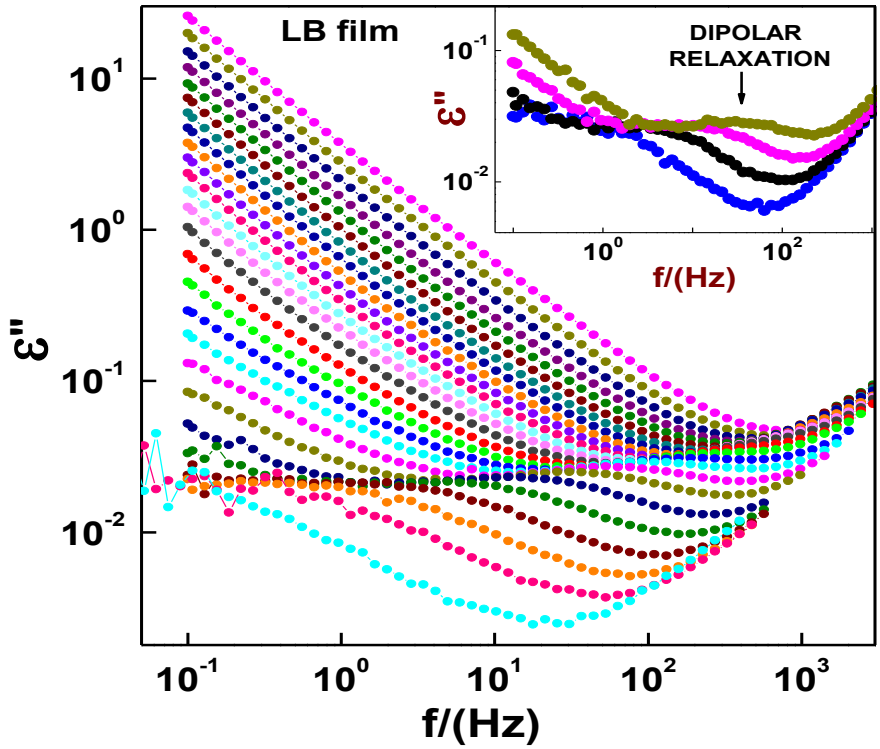

Figure (4.12): Isothermal dielectric loss spectra (ε"(*f*)) of the ODA-CdI_2EA film, measured upon heating.A clear loss feature is observed, marked by an arrow in the inset.

A less visible relaxation is also present at lower frequency in the spectra of Figure 4.12. Accordingly, we fitted the spectra with two Cole-Cole functions on top of a conductivity background.

The low-frequency relaxation is a conductivity relaxation, as proven by the validity of the BNN relation for this process (see Figure 4.13(a)). The origin of such space-charge relaxation is likely the hybrid character of the samples, i.e., the alternation of organic (ethylamine, ODA) and inorganic (CdI_2) moieties, leading to charge accumulation at their interfaces.

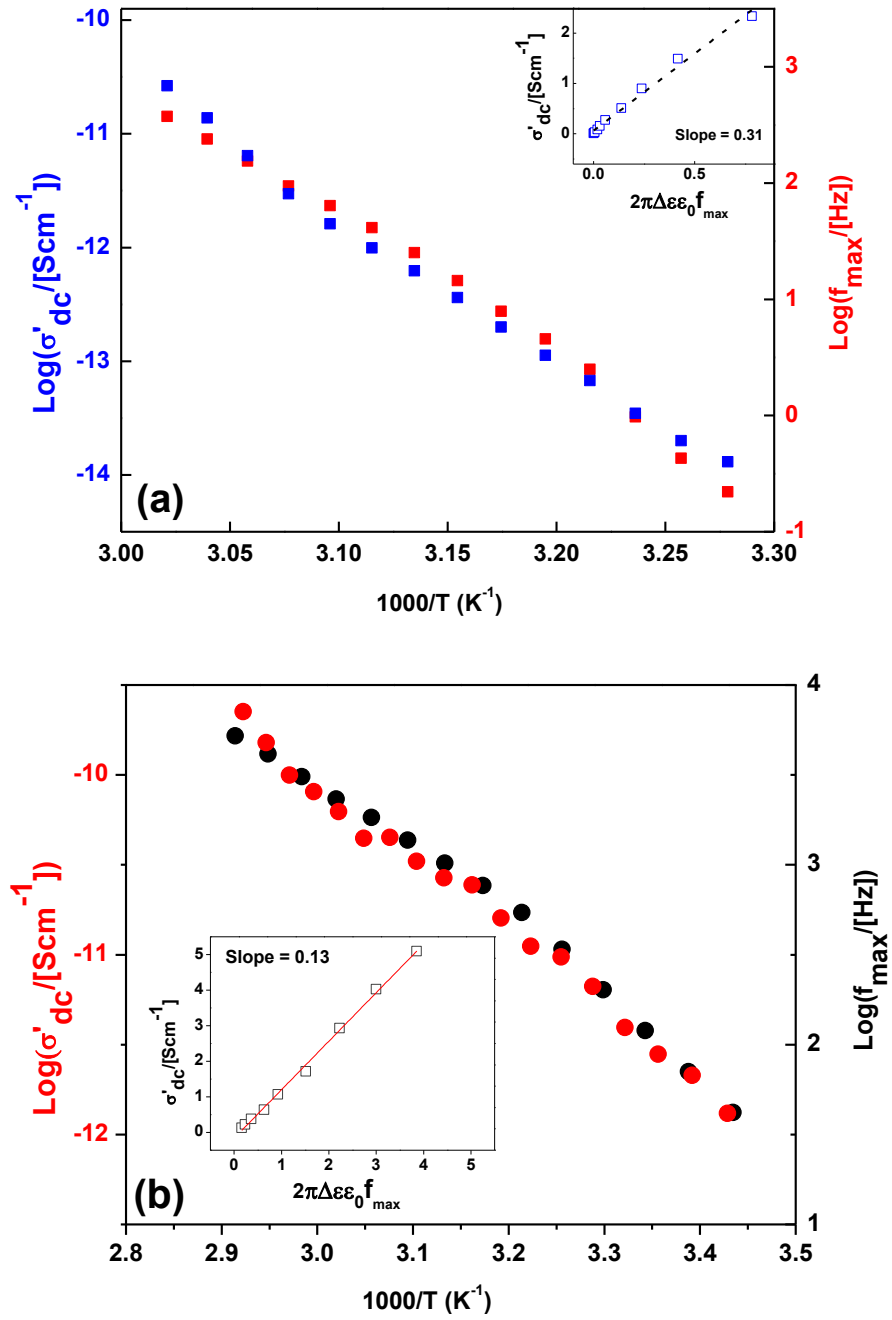

Figure (4.13): Arrhenius plot of dc conductivity (σ_{dc}) compared with relaxation frequency (f_{max}), for both the ODA-CdI_2EA film and the bulk CdI_2EA sample obtained by cooling from the melt. The vertical scales span the same numebr of decades. The insets show linear plots of f_{max} versus σ_{dc} to test the validity of the BNN relation in both samples.

As for the faster relaxation, it must be assigned to a molecular dynamics process such as a reorientation of the constituent molecules. In order to be observable by dielectric spectroscopy, such molecular dynamics must involve a change in direction of the molecular dipole moment. In other words, the dynamic motion must involve molecular species with non-zero dipole moment. Interestingly, while the bulk CdI_2EA sample also displayed a BNN-type relaxation (Figure 4.13(b)), it did not exhibit such fast relaxation.

The characteristic time of the fast dynamic process in the ODA-CdI_2EA film, as extracted from the fit described above, is shown as Arrhenius plot in Figure 4.14. The plot displays an overall positive curvature, typical of cooperative relaxations in glass-forming systems. In more detail, it appears that below the phase-change temperature of 317.5 K, the temperature dependence of the relaxation time is roughly simply-activated (i.e., it follows an Arrhenius law), while at higher temperature the temperature-dependence becomes sub-Arrhenius. An anomaly is also observed in the parameters of the Cole-Cole fit function of this relaxation at approximately the same temperature (not shown).

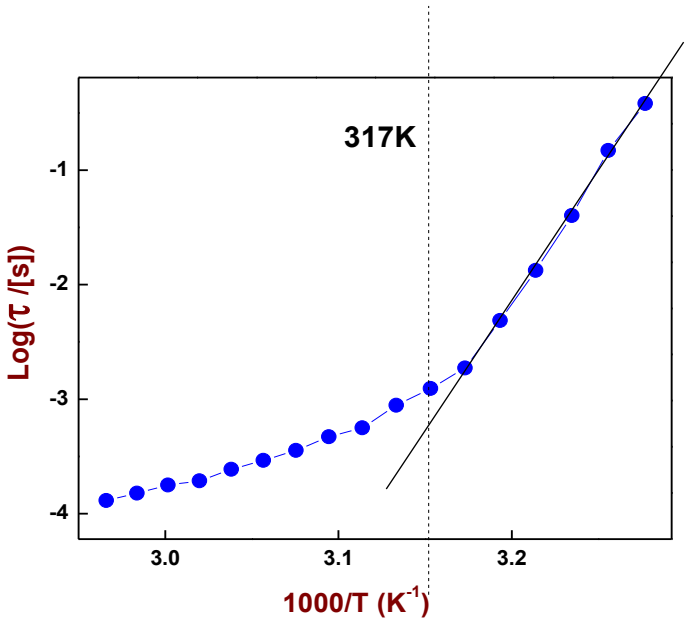

Figure (4.14): Arrhenius plot of fast relaxation time of the ODA-CdI_2EA film (data of Figure 4.12, relaxation shown in the inset). The straight oblique line is a fit with the Arrhenius equation.

The fact that the relaxation is only visible in the film indicates that it is a molecular dynamic process that can only take place in the LB geometry, either due to the different chemical composition or the looser local environment in the film compared with the bulk material.

It is at present unclear why the relaxation is not visible in the first experimental run, while conversely the change in conductivity is quite visible at first, while it is not so evident in subsequent runs. More experiments are needed to clarify these last two points.

4.7.Conclusions

In conclusion, we have implemented IDE-based dielectric spectroscopy on thin films deposited by three different techniques, namely immobilization from solution, thermal evaporation, and the Langmuir-Blodgett technique. We have shown that, in

the case of rhodamine 6G chloride, solution-based methods and thermal evaporation yield quite different results, due to decomposition of rhodamine 6G chloride (Rh6G) into chlorine-free rhodamine 19 (Rh19) upon sublimation. While pellets obtained by pressing polycrystalline powders are inhomogeneous and contain gaps, so that no reliable conductivity values can be obtained, the thin-film geometry allows determination of the exact conduction mechanism and measurement of the intrinsic conductivity of pure Rh6G and Rh19 phases.In particular, the room-temperature electronic conductivity is higher by one order of magnitude in Rh6G films than in Rh19 ones, likely due to the fact that the former are crystalline and the latter are amorphous. The dynamics of the molecular dipole associated with the chlorine counterions has much lower activation energy in the Rh6G films than that in bulk Rh6G material, possibly due to a looser environment in the film. As for Langmuir-Blodgett films of cadmium iodide ethylamine (CdI_2EA) covalently attached to octadecylamine-hydroiodide (ODA), the dielectric spectroscopy characterization indicates that the solid-solid phase transition (visible as a variation in vertical spacing between the ac conductivity spectra) in the films takes place at 317.5 K, i.e. roughly 5 K higher than in bulkCdI_2EA. Also, a dipolar dielectric relaxation is observed in the films, which is instead absent in the bulk sample. These differences between the ODA-CdI_2EA films and bulk CdI_2EA arise either because of the different chemical composition of the two, or the looser local environment in the film compared with the bulk material. More experiments are needed to settle this point.

These results show that silicon-chip-based DS is an easily implementable characterization probe of the thin-film form of organic materials, thus providing information that is directly relevantfor the sample geometry used in device applications. They also show that comparison between bulk and thin-film results are useful, but that molecular dynamics simulations or complementary techniques may be needed for a full interpretation of dielectric spectroscopy results.

Bibliography:

[1] F.Kremer, A.Schönhals, Broad Band Dielectric Spectroscopy ;Springer: Berlin, Germany, (2003)

[2] S.Capponi, S.Napolitano,N.R.Behrnd, G.Couderc,J.Hulliger, M.Wübbenhorst, Structural Relaxation in NanometerThin Layers of Glycerol. J. Phys. Chem. C, 114, 16696−16699, (2010)

[3] C.J.Palmstrom,Epitaxy of Dissimilar Materials.Annu.Rev.Mater.Sci., 25, 389−415,(1995)

[4] C.M.Evans, H.Deng,W.F.Jager, J.M.Torkelson, Fragility is aKey Parameter in Determining the Magnitude of Tg-ConfinementEffects in Polymer Films.Macromolecules, 46, 6091−6103, (2013)

[5] A.Sepulveda,E.Leon-Gutierrez,M.Gonzalez-Silveira,C.Rodriguez-Tinoco,M.T. Clavaguera-Mora,J.Rodriguez-Viejo,AcceleratedAging in Ultrathin Films of a Molecular GlassFormer.Phys. Rev. Lett, 107, 025901,(2011)

[6] T.H.Scabarozi, J.Roche, A.Rosenfeld, S.H.Lim, L.Salamanca-Riba, G.Yong, I. Takeuchi,M.W.Barsoum, J.D.Hettinger, S.E.Lofland, Synthesis and Characterization of Nb2AlC ThinFilms.Thin Solid Films, 517, 2920−2923,(2009)

[7] H.Y.Hwang,Y.Iwasa, M.Kawasaki, B.Keimer, N.Nagaosa, Y.Tokura, Emergent Phenomena at Oxide Interfaces. Nat. Mater., 11, 103−113,(2012)

[8]M.D.Ediger,P.Harrowell, Perspective:Supercooled Liquids andGlasses. J.Chem. Phys., 137, 080901, and references therein,(2012)

[9] K.R.Whitaker, D.J.Scifo, M.D.Ediger, M.Ahrenberg, C.Schick, Highly Stable Glasses of cis-Decalin and cis/trans-DecalinMixtures. J. Phys. Chem. B, 117, 12724−12733, (2013)

[10] S.Capponi,S.Napolitano, M.Wübbenhorst, SupercooledLiquidswithEnhanced Orientational Order. Nat. Commun., 3,1233,(2012)

[11] A.Sepulveda, E.Leon-Gutierrez, M.Gonzalez-Silveira, C. Rodriguez-Tinoco, M.T. Clavaguera-Mora, J.Rodriguez-Viejo, Glass Transition in Ultrathin Films of Amorphous Solid Water.J.Chem. Phys., 137, 244506, (2012)

[12] A.Sepulveda, E.Leon-Gutierrez, M. Gonzalez-Silveira, M.T. Clavaguera-Mora, J.Rodriguez-Viejo,AnomalousTransformationof Vapor-Deposited Highly Stable Glasses of Toluene intoMixed Glassy States by Annealing above Tg. J. Phys. Chem. Lett.,3, 919−923, (2012)

[13] Schaumburg, G. Novocontrol Dielectrics Newsletter. http://www. Novocontrol.de/newsletter/DNL22.pdf, Vol. 22, pp 5−8,(2006)

[14] D.J.Gundlach, Nature Materials 2007, 6, 173M.A. Lomillo Alonso, J. Gonzalo-Ruiz, F.PascualMuñoz, Biosensor Based on Platinum Chips for Glucose Determination. Anal.Chim.Acta, 547, 209−214, (2005)

[15] T.WKelley,P.FBaude, C.Gerlach, D.E..Ender,D.Muyres,M.AHaase, D.E Vo-gel, Theiss, S. D. Chemistry of Materials, 16, 4413,(2004)

[16] F. Palacio,J. S. Miller, Nature, 408, 421,(2000)

[17] D.B.Mitzi,K.Chondroudis,C.Kagan, IBM Journal of Research and Develop-ment, 45, 29,(2001)

[18] G.Pedro, C.Sanchez, Functional Hybrid Materials; Wiley-VCH, (2006).

[19] J.H.Im, C.R.Lee, J.W. Lee, S.W.Park and N.G.Park,Nanoscale, 3, 4088–4093,(2011)

[20] H.S.Kim, C.R.Lee, J.H.Im, K.B.Lee, T.Moehl,A.Marchioro, S.J.Moon, R. Humphry-Baker, J.H.Yum,J.E.Moser, M.Gr¨atzel and N.G. Park, Sci. Rep., 2,591,(2012)

[21] M.M.Lee, J.Teuscher, T.Miyasaka, T.N.Murakami and H.J.Snaith, Science, 338, 643–647,(2012)

[22] T.Sugimoto, H.Fujiwara, S.Noguchi,K. Murata, Science and Technology of Advanced Materials ,10, 024302,(2009)

[23] J.Lü,E.Shen,Y.Li, D.Xiao, E.Wang,L.Xu, Crystal Growth & Design, 5, 65,(2005)

[24] D. B.Mitzi, P.Brock, Inorganic Chemistry, 40, 2096,(2001)

[25] T.Kikteva, D.Star, Z. Zhao, T.L. Baisley, G.W. Leach, Molecular Orientation, Aggregation, and Order in RhodamineFilms at the Fused Silica/Air Interface. J. Phys. Chem. B, 103, 1124−1133,(1999)

[26] R.Macovez, N.Lopez, M.Mariano, M.Maymò, J.Martorell,Molecular Conformation in Organic Films from Quantum Chemistry Ab Initio Calculations and Second Harmonic Spectroscopy. J. Phys.Chem. C, 116, 26784−26790, (2012).

[27] H.Weininger,J.Schmidt, A.Penzkofer, Absorption Spectroscopic Investigaton of Rhodamine Dye Vapors. Chem. Phys., 130, 379−387, (1989)

[28] S.K.Tripathi,A.Monga,G.S.SSaini, Characterization of Thermally Evaporated Thin Films of Rhodamine 6G. J. Smart Mater. Struct. , 18, 125012,(2009)

[29]R.Macovez,E.Mitsari,M.Zachariah,M.Romanini,P.Zygouri,D.Gournis,J.Ll.Tamarit, Ultraslow Dynamics of Water in Organic Molecular Solids. J. Phys. Chem. C, 118, 4941−4950,(2014)

[30] M.P.J.vanStaveren, H.B. Brom, .L.J. de Jongh, Metal−Cluster Compounds and Universal Features of the HoppingConductivity of Solids. Phys. Rep., 208, 1−96, (1991)

[31] S.Capaccioli, M.Lucchesi, P.A.Rolla, G.Ruggeri, Dielectric Response Analysis of a Conducting Polymer Dominated by the Hopping Charge Transport. J. Phys.: Condens. Matter, 10, 5595−5617 ,(1998)

[32] R.Macovez, M. Zachariah, M.Romanini, P.Zygouri, D.Gournis,J.Ll.Tamarit, Hopping Conductivity and Polarization Effects in a Fullerene Derivative Salt. J. Phys. Chem. C, 118, 12170−12175, (2014)

[33] L.J.Huijbregts, H.B.Brom, J.C.M.Brokken-Zijp, M.Kemerink, Z.Chen, M.P.deGoeje, M.Yuan,M.A.JMichels, TheOptimalStructureConductivityRelation in Epoxy−PhthalocyanineNanocomposites.J.Phys.Chem.B, 110,23115–23122 ,(2006)

[34] T.B.Tran, I.S.Beloborodov, X.M.Lin, T.P.Bigioni, V.M. Vinokur, H.M.Jaeger, MultipleCotunneling in LargeQuantumDotArrays. Phys. Rev. Lett., 95, 076806 (2005)

[35] H.Böttger, V.V.Bryksin, Hopping Conduction in Solids;VCH:Weinheim, Germany, (1985)

[36] Sh.A.Mansour, I.S.Yahia, F.Yakuphanoglu, The Electrical Conductivity and Dielectric Properties of C.I. Basic Violet 10.DyesPigm., 87, 144−148,(2010)

[37] Y.Wu, T.Toccoli, N.Koch,E.Iacob, A.Pallaoro, P.Rudolf, S.Iannotta, Controlli -ng the Early Stages of Pentacene Growth by Supersonic Molecular Beam Deposition. Phys. Rev. Lett., 98,076601, (2007)

[38] H. Namikawa, J. Non-Cryst. Solids., vol. 18, p. 173, (1975)

[39] D.L.Sidebottom Phys. Rev. Lett., vol. 82, p. 3653, (1999).

[40] O.Laczka, E.Baldrich, X.F.Muñoz, F.J.del Campo, Detection of Escherichia Coli and Salmonella Typhimurium Using Interdigitated Microelectrode Capacitive Immunosensors: The Importance of Transducer Geometry. Anal.Chem., 80, 7239−7247, (2008)

CHAPTER-5

Collective relaxation dynamics and crystallization kinetics of amorphous Biclotymol antiseptic

5.1.Introduction

Pharmaceutically active molecules and active pharmaceutical ingredients are generally stored in solid form, either as crystalline or amorphous (glassy) powders. When a liquid is cooled fast enough to avoid crystallization, a glassy state can be reached; the transformation from liquid to glass occurs at the so-called glass transition temperature, T_g, where cooperative molecular motions slow down to the time scale of hundred seconds. Compared to the crystalline form, the amorphous (glass) form of pharmaceutical compounds offers the advantage of a higher solubility [**1]** and bioavailability **[2].** The glass state has however the disadvantage of being thermodynamically unstable against the nucleation of crystalline phases [**3,4].** The microscopic mechanisms governing the kinetic stability of organic glasses remains unclear, and the crystallization kinetics appears to be determined by a large number of factors such as preparation method, thermal and mechanical treatments employed during formulation [**5],** storage temperature, application of pressure or exposure to humidity [**6].** It is generally found that storage well below the glass transition temperature T_g (e.g., at T_g – 50K) prevents crystallization of the amorphous state and thus ensures a physically stable glassy drug during its shelf-life [**7,8]**. In general, the thermal energy and the molecular mobility below T_g are considered to be too low to produce the rearrangements necessary for the nucleation of the crystalline phase, although some authors have proposed that the secondary Johari–Goldstein relaxation (considered as the primitive relaxation) can provide enough mobility to activate the crystallization process. **[9]** A recent study **[10]** on the active pharmaceutical ingredient known as biclotymol has shown that it can be stored in its amorphous form during months also several degrees above the T_g of the material, i.e., at temperatures at which the material is in the supercooled liquid state and the molecular mobility is slow but not negligible.

Our interest in the crystallization of this material from the point of view of the research presented in this thesis lies in the fact that the study of crystallization kinetics is a less conventional application of dielectric spectroscopy (compared to more common studies of the molecular dynamics of glass-forming systems), and also in the fact that the crystalline phase obtained from the liquid phase of biclotymol grows in the form of 1D-like needles [**10,11**].Motivated by this low-dimensional behavior, we present here an experimental study of the re-crystallization of biclotymol from its supercooled state at four different temperatures by means of broadband dielectric spectroscopy [**12,13]**.Biclotymol presents a glass transition at T_g = 293 K **[11]**. It appears that below this temperature the molecular rearrangement is extremely slow and the molecules cannot reach their equilibrium positions, so that re-crystallization is not observed. We find, however, that crystallization of the supercooled liquid takes place on the timescale of hours even at moderate temperatures (T_g+14K), and that therefore temperature control is critical to preserve the amorphous state. We study in detail the fragility of this glass-forming active pharmaceutical ingredient (API) and the crystallization mechanism. In particular, the crystallization kinetics can be well described by the Avrami law with integer exponent n equal to 2, corresponding to one-dimensional growth of needle-like crystallites, as experimentally observed, with a time-independent nucleation rate.

Biclotymol, short name for 2,2-methylenebis(4-chloro-3-methylisopropylphenol), chemical formula $C_{21}H_{26}Cl_2O_2$with a molecular mass of 381.32 g.mol^{-1}, is an active pharmaceutical drug which has antiseptic properties for treatment in throat infection. It is also used in cough medicines. As shown in Figure 4.1, biclotymol is a phenolic compound, actually consisting of two functionalized phenyl groups covalently attached together.

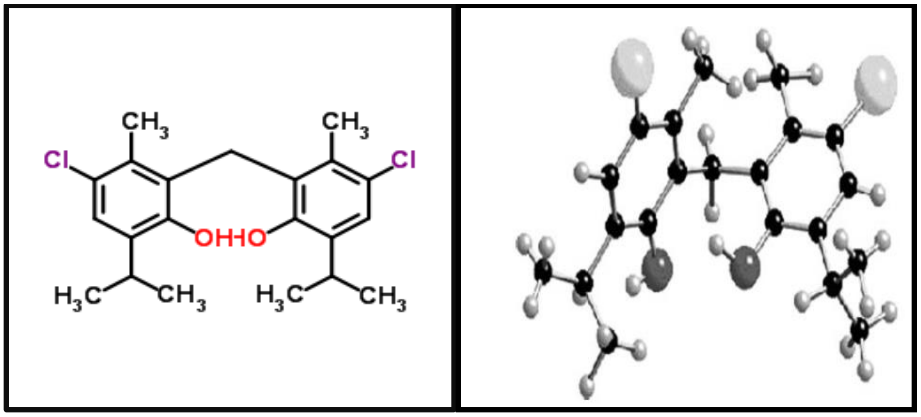

FIGURE (5.1) : Molecular structure of Biclotymol

5.2. Experimental Details

The sample was initially melted above 400 K and inserted in the molten state inside a home-made stainless steel capacitor specially designed for liquid samples. For plates separation, 50µm silica spacers are used. The capacitor was held at high enough temperature to ensure that the sample remained liquid during samplepreparation and was then mounted carefully in the dielectric spectroscopy setup. For studying molecular dynamics of drug the material was melted in the cryostat again to be sure that is in liquid form and then cooled fast enough (10K/min) to avoid crystallization. For studying crystallization kinetics at given four temperatures all measurements, the sample was initially meltedand then cooled down below T_g. All measurements for primary relaxation were measured while heating up for the same reason, and for isothermal crystallization measurements, the measuring temperature was reached by heating as fast as possible from T_g. Low frequency dielectric measurements were carried out in parallel-plate capacitor configuration by Novocontrol Alpha analyzer. For high-frequency measurements a HP4291 impedance analyzer was employed in reflectometry geometry, with the sample capacitor mounted at the end of a coaxial cable (see chapter 2for more details).Only few measurements were carried out between

10^6 and 10^9 Hz to probe the secondary relaxation dynamics above the glass transition temperature.

5.3.Primary and Secondary RelaxationBehavior

Figure 5.2 shows the real (a) and imaginary (b) parts of the permittivity spectra of biclotymol in temperature range from 115 to 350 K and for frequencies between 10^{-2} to 10^6 Hz.

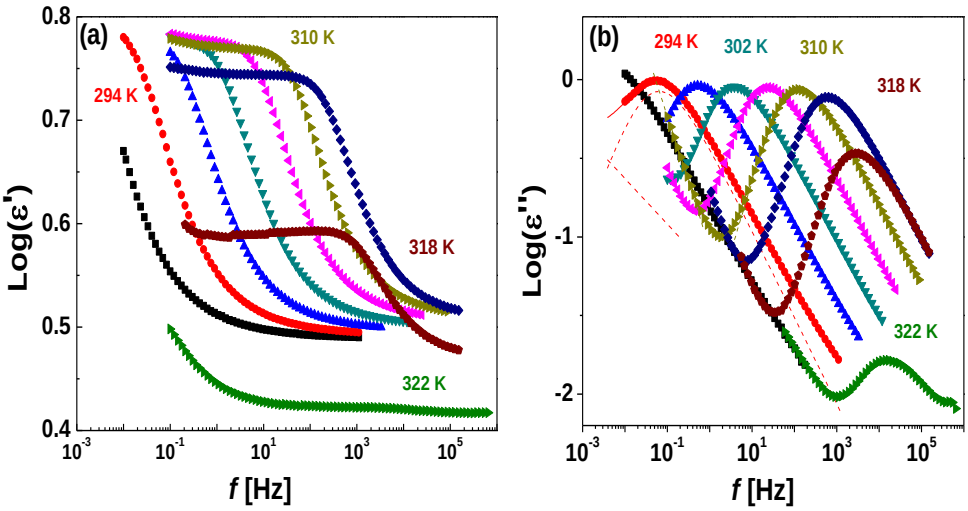

FIGURE (5.2): Real part of permittivity (a) and loss spectra (b) of supercooled Biclotymol between 290 and 322K,measured every 4K upon heating. Continuous lines are fits using a Havriliak-Negami function on top of a conductivity background proportional to inverse of frequency.

In these temperature and frequency windows, biclotymol exhibited two dynamic processes, namely a collective primary relaxation at lower frequency (α process) and a secondary dynamics (β process) at higher frequency.The primary relaxation is clearly visible in Figure 5.2 both as a loss peak in the imaginary partof the permittivity (panel b),and as a step-like decrease in the real part (panel a) as expected from the Kramers–Kronig transformations **[14]**.Such primary relaxation corresponds to so-called α

process stemming from the collective reorientation of the Biclotymol molecules. The value of the real part of the permittivity at frequencies lower than the primary relaxation can be taken as an estimate of the relative dielectric constant of the material. For amorphous Biclotymol, it appears to be roughly 6 near room temperature.The spectral position of theloss feature shifts to lower frequency (longer characteristic times) as the temperature is decreased until it freezes out slightly above 290 K (Fig. 5.2(b)), which is consistent with the glass transition temperature obtained from our calorimetry data, displayed in Fig. 5.3.

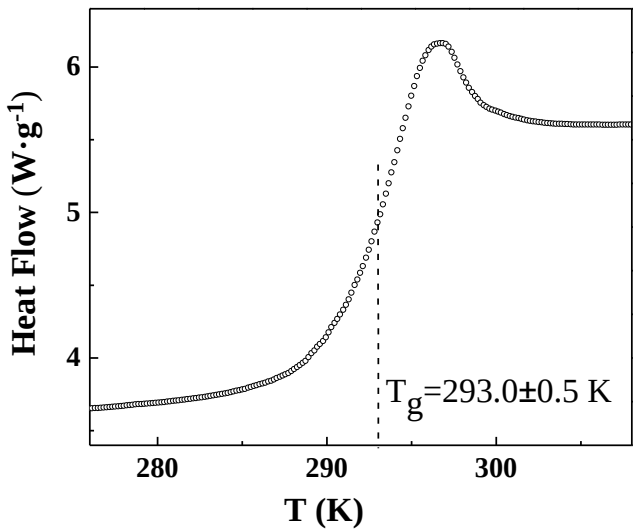

Figure (5.3):Differential scanning calorimetry thermogram acquired upon heating from below T_g, after cooling the sample from the molten state at a rate of 10 K min^{-1}. The dashed line indicates the glass transition temperature T_g determined from the inflection point below the endothermic feature in the thermograph.

As visible in Figure 5.3, the calorimetric T_g determined from the inflection point of the specific heat jump is 293.0 ± 0.5 K, in perfect agreement with a recent calorimetry study of the crystallization kinetics **[10]**(an additional determination of the glasstransition temperature by dielectric spectroscopy can be obtained from the fit to the Arrhenius plot to the dielectric spectra, see below).

Biclotymol also exhibited a secondary relaxation feature, visible at higher characteristic frequency than α process. Fig. 5.4 shows dielectric loss spectra at different temperatures below T_g, to highlight the temperature evolution of the secondary process.

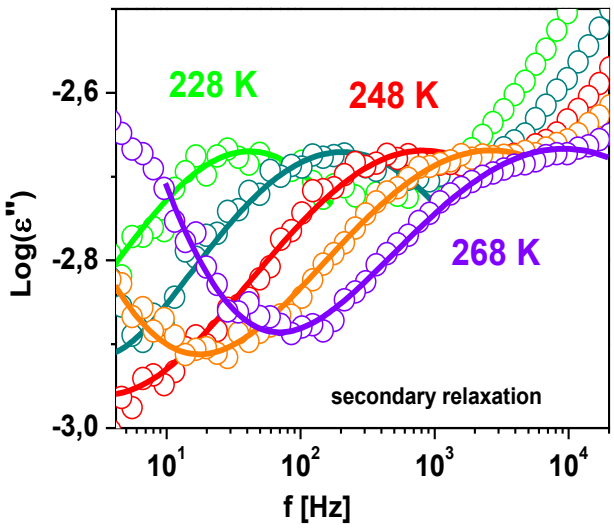

Figure (5.4): Secondary relaxation dynamics at few selected temperature fitted with a Cole–Cole function plus a background mimicking the high-frequency tail of theα relaxation feature

It can be observed that the dielectric strength of this secondary process is quite low, namely of the order of 10^{-3} (much smaller than that of the cooperative α relaxation). A high-frequency spectral background, which increases with increasing frequency, may be noticed in these low-temperature spectra. Such high-frequency background could be due to heterogeneities induced in the sample by the rapid cooling to below T_g that was performed to avoid crystallization of the supercooled liquid phase.

The primary relaxation feature (α) was fitted with a Havriliak–Negami function, superposed to a background proportional to reciprocal frequency that mimicked the conductivity contribution to the loss spectra. The exponents of the Havriliak–Negami function were in the range from 0.8 to 0.9 for β and close to 0.55 for γ, although they varied slightly with temperature. The secondary (τ_s) relaxation processes was fitted as a

Cole–Cole function, commonly employed for secondary relaxations **[14]**. The value of the Cole-Cole shape parameter was in the range between 0.4 and 0.6.For the fit of secondary relaxation, a background proportional to reciprocal frequency was also added, to reproduce the high-frequency tail of the α process.

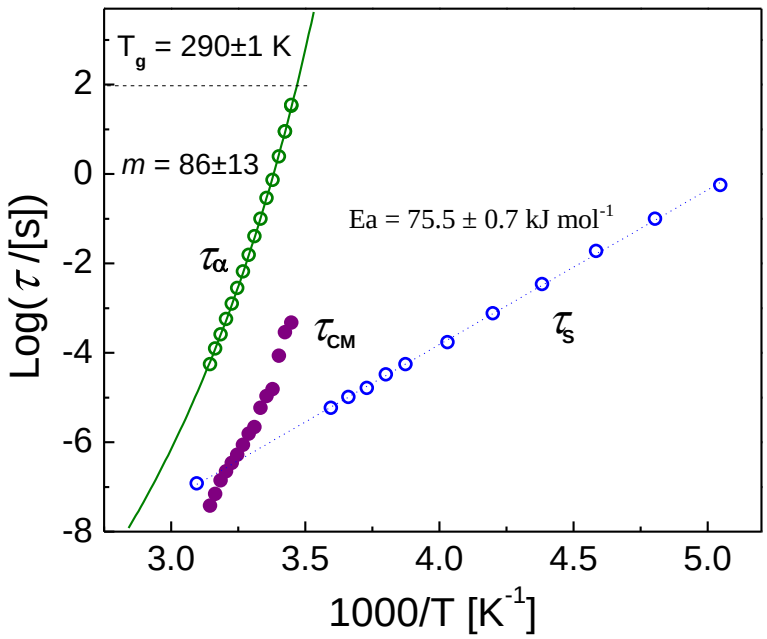

FIGURE (5.5): Arrhenius plot of the primary relaxation (τ_α) and secondary (τ_s) relaxation times. The continuous line is the fit of τ_α using the Vogel–Fulcher–Tammann equation (see Chapter 2),while the dotted line is the fit of τ_s assuming a simply-activated (Arrhenius) temperature dependence. The horizontal dashed line indicates the value of τ_α (Log τ_α = 2, i.e., τ_α = 100 s) that corresponds to the glass transition temperature (T_g = 290 ± 1 K). Filled markers indicate the theoretical relaxation time τ_{CM} of a Johari– Goldstein relaxation precursor to the primary relaxation, as calculated according to the Coupling Model.

Figure5.5 shows the relaxation times of both relaxations, τ_α and τ_s, displayed as Arrhenius plots. It is observed that $\tau_s$exhibits a simply activated (Arrhenius) behavior, with constant activation energy E_a = 75.5 ± 0.7 kJ mol^{-1}; instead, τ_α exhibits a more pronounced (super-Arrhenius) temperature dependence. The relaxation time of the α

process could be fitted using the Vogel–Fulcher–Tammann (VFT) equation (see Chapter 2):

$$\tau_\alpha = \tau_0 \, exp\left[\frac{DT_{VF}}{T-T_{VF}}\right] \quad (1)$$

The values of the prefactor τ_0, the strength parameter D and the Vogel-Fulcher temperature T_{VF} obtained from the fit were, respectively, $Log(\tau_0/[s]) = -18.9 \pm 0.9$, $D = 15.5 \pm 1.9$ and $T_{VF} = 218 \pm 4$ K. The glass transition temperature, estimated as the temperature at which the VFT function displayed a value of τ_α equal to 100 s, is $T_g = 290 \pm 1$ K, which matches perfectly that estimated by calorimetry (shown in Figure 5.3). A slight difference between the two techniques might arise due to the different cooling/heating rates in each experiment. A VFT profile is indicative of a co-operative nature of the relaxation process, which becomes more pronounced approaching the glass transition temperature. As it should be in the VFT model, T_{VF} is lower than T_g.

While the α relaxation feature is the collective relaxation process associated with the glass transition, the identification of the secondary process is not as straight forward.Secondary processes in glass-forming materials may correspond either to intramolecular motions involving a relative motion of polar sidegroups, or else involve the whole molecule and represent the single-molecule precursor of the cooperative α relaxation. **[14,15]** The latter type of secondary relaxations are termed Johari–Goldstein relaxations and are directly correlated with the primary α dynamics **[16,17]**. For example, according to the so-called Coupling Model **[18]**, the relaxation time τ_{CM} of the Johari–Goldstein relaxation should be related with that of the primary process (τ_α) as:

$$\tau_{CM} = t_c^p (\tau_\alpha)^{1-p} \quad (2)$$

Here t_c is a cross-over time, whose typical value is 2×10^{-12} s for molecular and polymeric glass formers [**18,19]** and *p* is a shape parameter of the α relaxation given by $p = 1 - \beta_{KWW}$, where β_{KWW} is the exponent of the stretched exponential function that

describes the α spectral feature in the time domain (see Chapter 2). For the obtained shape parameters (β,γ) of the HN function employed to fit the α relaxation, the value of *p* can be accurately estimated as $p \approx 1-(\beta\gamma)^{1/1.23}$ **[19]**. The theoretical precursor time τ_{CM} calculated using Eq. (2) is shown in Fig. 5.5 together with the experimental values of τ_α and τ_s. It may be observed that τ_s is, for most temperatures, quite far from the value expected for a Johari-Goldstein precursor, and has a totally different temperature dependence, which indicates that the secondary process is an intramolecular relaxation rather than a whole-molecule relaxation. This is also confirmed by the fact that the activation energy (slope) of the secondary relaxation does not change below T_g (see Fig. 5.5), as it is instead customary for Johari–Goldstein relaxations **[16]** Judging from its relatively high activation energy (75.5 ± 0.7 kJ mol^{-1}), it is likely that this intramolecular secondary dynamics involves the hydrogen bonds formed by the hydroxyl groups (and possibly the chlorine atoms) of biclotymol, as found in other organic small-molecule glass formers [20], given that hydrogen bonds have a relatively high cleavage energy leading to a high activation energy of associated secondary processes **[21]**.

From the fit of τ_α with Eq. (1) one may obtain the kinetic fragility index of the biclotymol glass-former. The fragility index is defined as:

$$m = \left.\frac{d(Log\tau_\alpha)}{d\left({}^{T_g}/_{T}\right)}\right|_{T=T_g} \qquad (3)$$

The obtained experimental value is *m*=86±13. This value matches that calculated directly from the VFT fit parameters listed above according to the relation**[22]**:

$$m = (D/Ln(10))\left(T_{VF}/T_g\right)/(1-T_{VF}/T_g)^2 = 82 \pm 15. \qquad (4)$$

Both values are slightly lower than (but compatible with) the value obtained from calorimetry experiments **[10]**, which was reported to be 99± 5. This confirms, by means of a more direct experimental tool such as dielectric spectroscopy, that biclotymol is a rather fragile glass-former **[10]**. As for the temperature dependence of the dielectric strength of the loss feature, it is constant for temperatures close to T_g, while it is observed to decrease upon heating (in Fig.5.2, starting from 318 K). Since the dielectric strength $\Delta\varepsilon$is proportional to the number of molecules participating in the cooperative α relaxation, the decrease of the dielectric strength is indicative of a re-crystallization process, in which some molecules are removed from the supercooled liquid phase, in which they are mobile, to form crystallites in which all motion ceases.

5.4.Analysis of the Crystallization Kinetics

The process of re-crystallization is a complex phenomenon of crystal nuclei formation and crystal growth. Crystallization more likely takes place at higher temperature because the viscosity η, which is essential to the crystallization transition **[23]**, is lower at the higher temperature. The molecular diffusional relaxation time τ_α is related to the viscosity by the relation $\eta = G_\infty \tau_\alpha$, where G_∞ is the elastic shear modulus, that does not vary considerably in the supercooled liquid regime **[14]**. In other words, the relaxation time τ_α of the primary process is basically proportional to the viscosity and thus directly correlated with the crystallization process. Just as the primary relaxation boosts the crystallization transition, it has been suggested that secondary precursor relaxations (Johari–Goldstein) could also trigger crystallization **[24]**.A partial evidence for this is the fact that glasses are generally stable against crystallization only well below T_g**[25]**, namely, at temperatures at which not only the primary process, but also precursor secondary relaxations are frozen. As discussed, the secondary relaxation in Biclotymol is not a precursor relaxation but rather an intramolecular one, which would explain why the material is stable against crystallization already near T_g**[10]**, where only the α process is almost frozen while the secondary relaxation is not.

In the case of Biclotymol, while the material exhibits a crystallographic stable phase known as Phase I, upon re-crystallization from the melt a metastable phase (Phase II) is

formed. This has been evidenced by a previous study employing DSC, optical microscopy and XRD, some results of which are displayed in Figure 5.6.

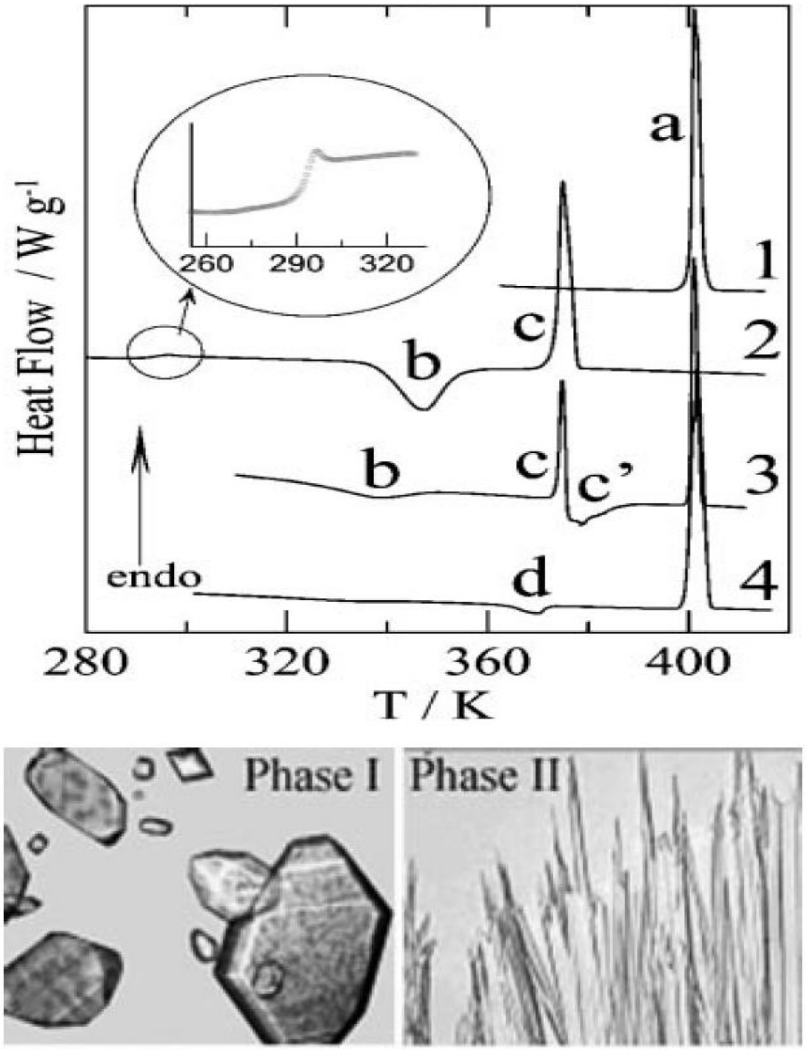

FIGURE(5.6): Upper panel: Differential Scanning Calorimetry curves. Curve1: Melting of biclotymol Phase I (peak a). Curve2: Thermal effects recorded upon heating the glassfrom the Phase-I melt: glass transition (see inset),re-crystallization into Phase II (peak b), melting ofPhase II (peak c). Curve 3: Thermal effects sometimesrecorded upon heating the Phase-I melt: recrystallizationinto phase II (peak b), melting of Phase II (peak c)and recrystallization into Phase I (peak c'), then meltingof Phase I. Curve 4: Thermal effects sometimesrecorded upon heating Phase II from room temperature:solid-solid transition into Phase I (peak d), then meltingof Phase I. Lower left panel:Polyhedralcrystals of Phase I in equilibrium with the liquid at400 K. Lower right panel: Needles of Phase IIhaving spontaneously grown from the metastablemelt at 344 K. [After Ref. **11**]

As visible in the lower panels of Figure 5.6, the two crystalline phases (I and II) exhibit very different crystallite morphology. This is indicative of a different crystal structure of two phases, as confirmed directly by study of the respective x-ray diffraction patterns [**11**]. To characterize in detail the crystallization of biclotymol from the supercooled liquid state, we performed four separate experiments at four fixed temperatures, which were reached by heating up from a temperature lower than T_g to preserve (initially) the supercooled liquid state. The experimental results are reported in Figs. 5.7 and 5.8 for real and imaginary parts of the permittivity, respectively. As already mentioned, the supercooled liquid phase of biclotymol crystallizes into a metastable solid phase (Phase II) **[10,11]** rather than into the stable crystalline Phase I. After nucleation of metastable crystallites, and during its growth, the sample is in a mixed phase that is partially crystalline (Phase II) and partially amorphous. Fig. 5.9(a) shows an optical microscopy image of the sample taken during the crystallization process (see also the lower right panel of Figure 5.6). Needle-like (Phase II) crystallites are observed, which are embedded in an amorphous (supercooled liquid) biclotymol matrix from which they are spontaneously nucleated.

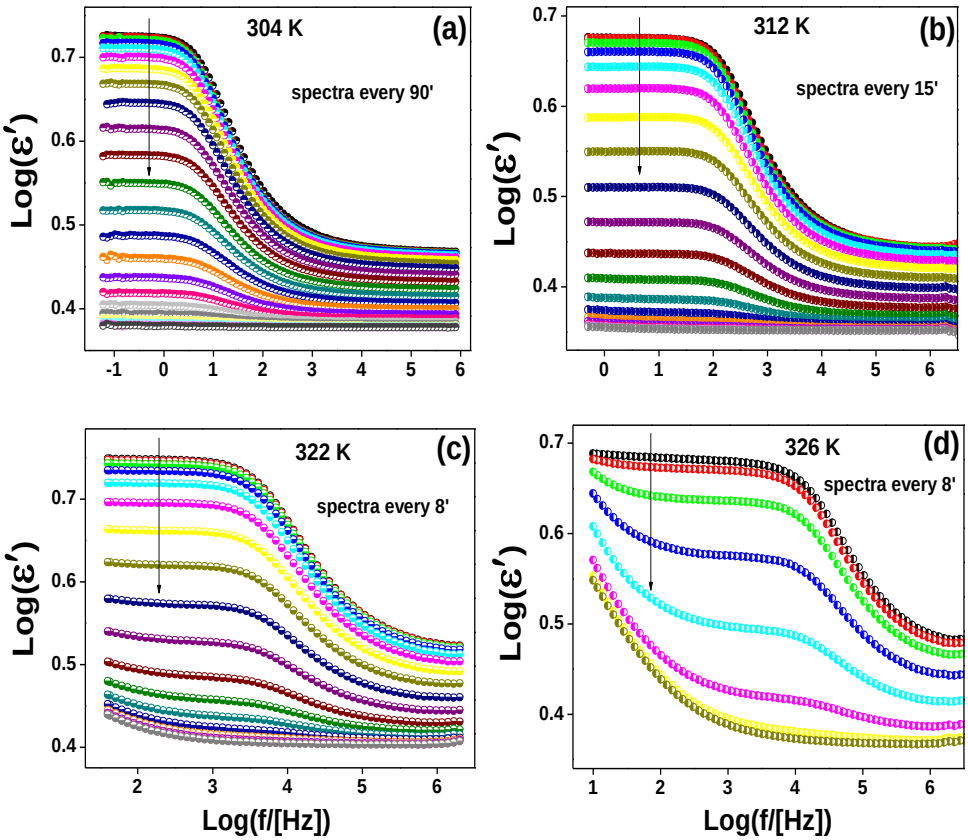

FIGURE (5.7): Real permittivity spectra ε`(f) of biclotymol during isothermal dielectric measurements at the temperatures of 304 (a), 312 (b), 322 (c) and 326 (d) K as a function of time. The arrows indicate the line shape changes as crystallization progresses. For clarity, only some of the spectra are displayed, namely those measured at fixed time intervals (specified in minutes in each panel).

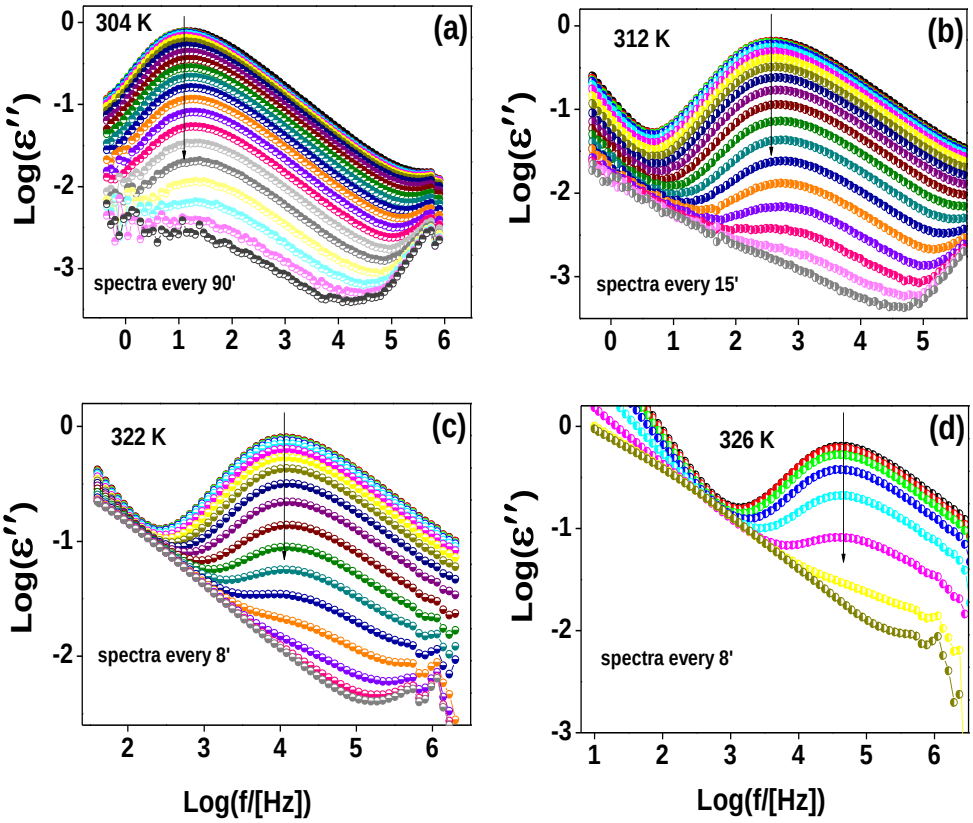

FIGURE (5.8): Loss spectra ε``(f) of biclotymol during isothermal measurements at 304 (a), 312 (b), 322 (c) and 326 K (d) as a function of time. The strength of the loss feature, proportional to the number of molecules in the amorphous phase, decreases over time due to crystallization (see arrows). The displayed spectra correspond to the same measurements as in Fig. 5.6, namely those acquired at fixed time intervals as specified in each panel.

The fits of the series of loss spectra shown in Fig. 5.8 indicate that, as the dielectric strength of the α relaxation decreases during isothermal annealing, it also shifts slightly towards higher frequencies. In other words, the time τ_α of maximum loss of the amorphous part of the sample becomes shorter during the growth of the crystallites, as visible in Fig. 5.9b. The origin of such shift must be related to the growth of the crystallites at the expense of the amorphous phase. One possibility is that (partial) crystallization results in smaller amorphous domains in which the cooperative α

process involves dynamically-correlated clusters of fewer molecules, thus yielding faster dynamics. Another possibility is that, since the density of a crystal phase is usually higher than that of the amorphous phase, partial crystallization results in a larger free volume per molecule in the amorphous state (to put it in different words, the molecular dynamics is faster at the surface of a cluster where the molecules have lower coordination number, and such "surface effect" becomes more important as the size of amorphous domains is reduced). At the same time, the width of the relaxation feature increased (as visible e.g. in the increase of the shape parameter *p* over time, not shown). This is indicative of a greater variety of local environments of the Biclotymol molecules in the amorphous phase as the crystallization progresses, and it likely results from the shrinking of amorphous domains, which leads to different extent and shape of cooperatively relaxing molecular clusters (more pronounced surface/interface effect). A spectral evolution of the α relaxation peak during crystallization is frequently observed **[26,27]**.

The evolution of the spectral strength Δε is best observed in the real permittivity spectra (Fig. 4.7) where it corresponds to the difference between the static permittivity value ε_s at the lowest frequencies (i.e., between 0.1 and 100 Hz depending on the measuring temperature) and the value ε_∞at frequencies higher than that of the relaxation peak (e.g. at the highest measured frequency of 2×10^6 Hz). The initially constant value of ε_s observed in the series of isothermal spectra acquired at 304K or312 K corresponds to the full dielectric strength in the supercooled liquid phase before the onset of crystallization. As known, the quantity $\Delta\varepsilon = \varepsilon_s - \varepsilon_\infty$ is directly proportional to the number of molecules in the amorphous phase, so that Δε decreases as the crystallization develops. To analyze the crystallization kinetics, we have studied the time evolution of the normalized static-permittivity difference, defined as **[28]:**

$$\hat{\varepsilon}(t) = \frac{\varepsilon_S(t) - \varepsilon_S(SL)}{\varepsilon_S(MC) - \varepsilon_S(SL)} \qquad (5)$$

Here ε_s(SL) and ε_s(MC) are the static permittivity of the supercooled liquid and metastable crystal (Phase II), respectively, as measured the former before the onset of nucleation of the crystal phase and the latter at the end of the crystal growth, while ε_s(t) is the static permittivity of the mixed-phase sample as a function of the time elapsed from the start of the isothermal measurements. The quantity $\hat{\varepsilon}$(t) is plotted in Fig. 5.9(c) for all four studied crystallization temperatures. For small t, the sample is still in the supercooled liquid state and ε_s(t) = ε_s(SL), so that $\hat{\varepsilon}$=0, while for largest the sample has crystallized completely and ε_s(t)= ε_s (MC), so that $\hat{\varepsilon} = 1$ (these lower and upper bounds are indicated by dashed lines in Fig. 5.9(c)). The normalized static-permittivity difference can be used to describe the time-dependence of the crystallization process, i.e., the crystallization kinetics. Assuming an Avrami-like temporal dependence of the crystallization **[29,30],** the normalized static-permittivity difference can be used to describe the time-dependence of the crystallization process, i.e., the crystallization kinetics. Assuming an Avrami-like temporal dependence of the crystallization **[29,30]** the normalized static-permittivity difference can be described by the equation **[9]:**

$$\hat{\varepsilon}(\mathrm{t}) = 1 - \exp(-K(t - t_0)^n) \qquad (6)$$

In this expression, valid at times greater than the induction time t_o (onset time of nucleation of the crystal phase), *K* is the temperature-dependent crystallization rate and *n* is the so-called Avrami exponent, which depends only on the crystallite morphology and crystallization mechanism **[31]**

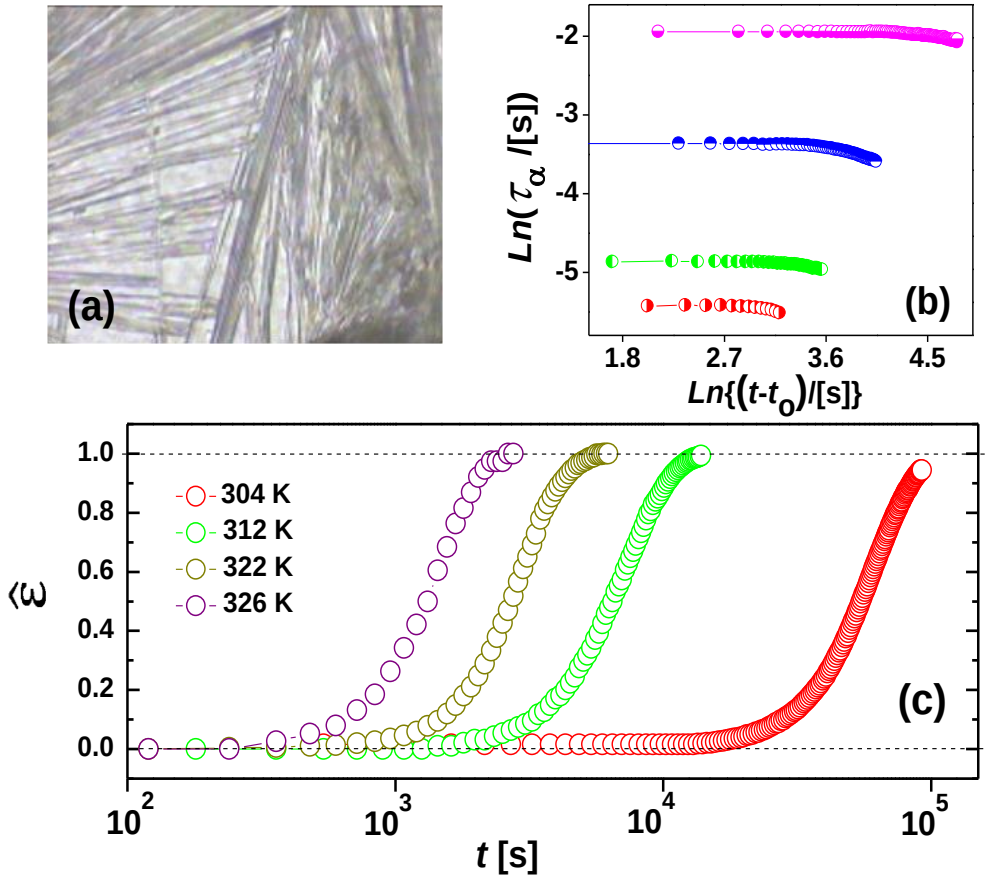

FIGURE (5.9): (a) Optical microscopy photograph of the needle-like crystallites of Phase II of Biclotymol grown spontaneously from the supercooled liquid state. (b) Logarithmic plot of the time-evolution of the characteristic relaxation time τ_α of the α relaxation, during crystallization from the supercooled liquid phase to the crystalline Phase II of Biclotymol, as a function of time since the induction time to. (c) Time evolution of the normalized static-permittivity difference $\hat{\varepsilon}$ during crystallization, as a function of the time elapsed since the start of each isothermal measurement (in logarithmic scale). Both τ_α and $\hat{\varepsilon}$are plotted as a function of time for all four isothermal crystallization temperatures (304, 312, 322 and 326 K).

To verify the dependence predicted by Eq. (5), in Fig. 5.10 we have plotted the quantity $\mathrm{Ln}\,[-\mathrm{Ln}(1-\hat{\varepsilon})]$ versus $\mathrm{Ln}(t-t_o)$ (Avrami plot) for all four studied temperatures. It may be observed that for all the temperatures studied the crystallization kinetics follows the time dependence predicted by the Avrami equation, with virtually the same slope (i.e., the same exponent *n*). The best-fit

parametersobtained by fitting the experimental data to Eq. (5) are shown in Table 5.1, together with the experimental values of the induction time t_o.

T(K)	***t*$_o$(min)**	**Ln(*K*)**	***n***
304±0.1	295±2	-9.66±0.03	2.00±0.01
312 ±0.1	26 ±2	-7.92 ±0.04	2.01±0.01
322 ±0.1	13 ±2	-7.22 ±0.05	2.04±0.02
326 ±0.1	4 ±2	-6.96 ±0.14	2.14±0.05

TABLE(5.1):Experimental parameters obtained by fitting the experimental normalized static permittivity difference by means of Avrami equation, Eq. (5), together with induction time t_o (time elapsed before the crystallization onset)

The crystallization rate *K* and the induction time $t_o$are displayed as Arrhenius plots in the inset toFig. 5.10.

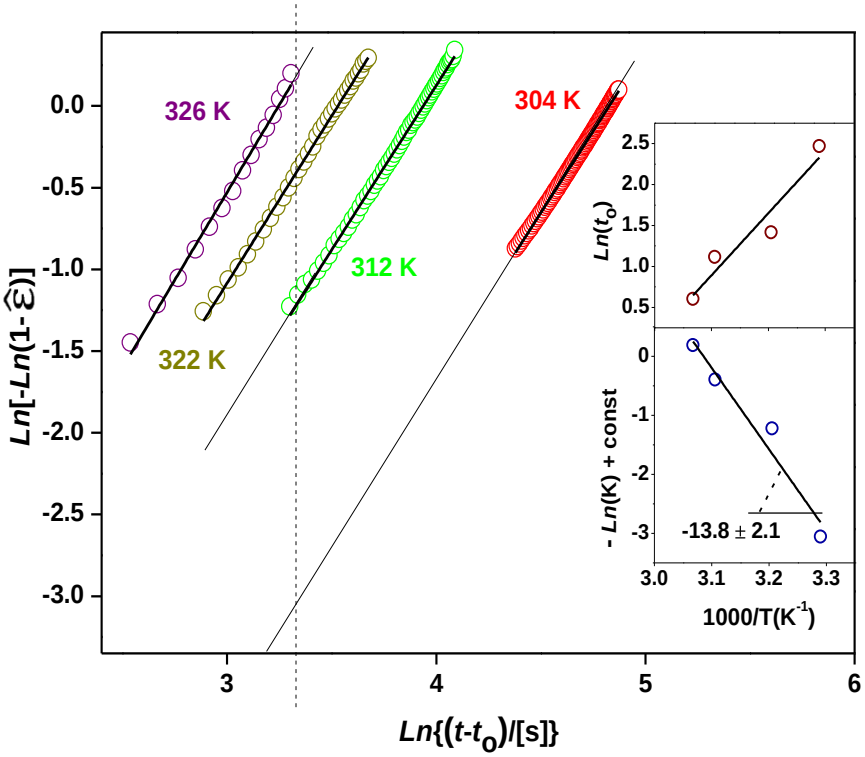

FIGURE (5.10): Avrami plot of the normalized static-permittivity ε̂difference as a function of the time elapsed from the crystallization onset ($t - t_o$), for all four isothermal crystallization temperatures studied. The continuous lines are linear fits, while the dashed vertical line indicates the time at which the value of the ordinate was taken for calculating the activation barrier of the crystallization process. The corresponding ordinate values are shown as an Arrhenius plot in the bottom inset, while the top inset shows the Arrhenius plot of the induction time t_o.

It may be observed that the induction time t_o decreases with increasing temperature, and that the crystallization rate increases with temperature. Both features are expected since higher temperature implies higher thermal energy and therefore higher probability that the crystal phase may nucleate and grow. Though nucleation and growth are independent processes, both processes are boosted by a temperature increase, as visible from the insets to Fig. 5.10. In principle, the induction time should correlate only with the nucleation rate, while the crystallization rate *K* depends both on

the nucleation rate and on the growth rate. The crystallization rate *K* is expected to display a simply-activated thermal behavior, that is, to scale as **[32]:**

$$L_n[K(T)] \sim -\frac{E_a}{k_B T} (7)$$

In this expression, k_BT is the thermal energy and E_a is the activation barrier for the crystallization process. The crystallization rates reported in Table 5.1 correspond to the intercept of the Avrami plots of Fig. 5.10, i.e. to the value of the fit function when the abscissa is zero because this extrapolated value is far from the experimental data points, it can be strongly affected by an error in the determination of the slope. For this reason, to study the temperature dependence of Ln(*K*) we have taken the value of the fit function at the time t^* given by $\mathrm{Ln}(t^* - t_o) = 3.329$ (marked by the dashed vertical line in Fig. 5.10), time at which experimental values are available for three out of the fours studied temperatures. If, as supported by of Fig. 5.10, the slope of all four Avrami plots is the same, then the vertical separation between them is independent of time (value of the abscissa), so that any value of the abscissa can be used to track the temperature dependence of the crystallization rate. The values thus obtained are shown as Arrhenius plot in the bottom inset to Fig. 5.10. The obtained points were fitted assuming a simply-activated behavior. The value of the activation energy extracted from the slope of such linear fit was E_a=115 ± 22 kJ.mol^{-1}. A similar value (but with a higher percent uncertainty) is obtained from the Arrhenius-law fit of the values of Ln(*K*) listed in Table 5.1. Also the induction time appears to follow an activated behavior, as visible in the top inset to Fig. 5.10, albeit with a different activation energy, as expected.

It may be observed in Table 5.1 that, while both t_o and *K* are clearly temperature-dependent, the value of *n* is basically constant for all studied temperatures. This is also visible from the very similar slopes of all four Avrami plots in Fig. 5.10. The Avramiexponent is indeed expected to have a fixedvalue because it depends only on the crystallite morphology and growth mechanism **[31]**, and these features are not expected to change in a relatively narrow temperature interval as the one studied here. It may be observed from Fig. 5.10 that for the temperature of 326 K, where

crystallization is quite fast, the agreement between the fewer experimental points available and the Avrami model is less than optimal, which is possibly due to the fact that at high crystalline volume fraction deviations from the Avrami law can occur dueto boundary effects **[33]**. If we exclude the value of *n* found for such temperature, then the value of the Avrami exponent for biclotymol is obtained as $n = 2.02 \pm 0.02$.

Avrami's original theory concerned homogeneous crystallization in 1, 2 or 3 dimensions, and predicted an integer value of *n* between 1 and 4 **[29,30]**. As visible in Fig. 5.9(a), the metastable Phase II grows by formation of needle-like crystallites, i.e., it displays a typically one-dimensional growth. Such long and thin crystallites appear to nucleate at different times after the induction time t_o (they display different length at different elapsed times) and to grow forming bundles **[10,11]**. The exponent $n = 2$ corresponds then to one-dimensional (needle-like) crystallization with a continuous, time-independent nucleation rate after the onset time to [**34**]. Biclotymol appears to be a textbook-like example of the integer Avrami law for 1D crystal nucleation and growth.

5.5.Conclusions

We have presented a dielectric spectroscopy study of the relaxation dynamics and crystallization kinetics in the supercooled amorphous phase of the pulmonary antiseptic biclotymol. This pharmaceutically active molecule is found to be a relatively fragile glass-former with fragility index m=86 ±13. The primary relaxation process is characterized by an asymmetric spectral lineshape and non-simply-activated temperature dependence. This collective relaxation freezes out at the glass transition temperature of T_g= 290±1 K. Also a secondary relaxation feature is observed near and below T_g. This secondary relaxation, which exhibits simply-activated thermal behavior with activation energy of 75.5±0.7 kJ.mol^{-1}, corresponds to an intramolecular dynamic process likely associated with hydrogen bonding. No clear precursor (Johari–Goldstein) relaxation could beobserved, which could explain the reported stability of amorphous biclotymol a few degrees above T_g, where the collective dynamics is almost frozen while the secondary relaxation is not. The crystallization mechanism is

one-dimensional, with a constant rate of nucleation and growth, leading to the formation of needle-like crystallites and to an Avrami exponent equal to 2, which is found to be independent of temperature. The activation barrier for crystallization is 115 ±22 $kJ.mol^{-1}$, a value similar to that of other low-mass organic molecules and active pharmacological ingredients. Our study shows that dielectric spectroscopy characterization is a valuable tool to investigate and understand the kinetic stability of amorphous pharmaceuticals.

Bibliography:

[1] P.Gupta, G.Chawla, A.Bansal, Physical Stability and Solubility Advantage from Amorphous Celecoxib: The Role of Thermodynamic Quantities and Molecular Mobility. Mol. Pharmaceutics- 1, 406−413 (2004)

[2] A.Serajuddin, Solid Dispersion of Poorly Water-Soluble Drugs: Early Promises, Subsequent Problems, and Recent Breakthroughs. J. Pharm. Sci.-88, 1058−1066 (1999)

[3] S.Bhardwaj, K.Arora, E.Kwong, A.Templeton, S.DClas, R.Suryanarayanan, Correlation between Molecular Mobility and Physical Stability of Amorphous Itraconazole, Mol. Pharmaceutics - 10, 694−700 (2013)

[4] D.Zhou, G.Zhang, D.Law,D.Grant, E.Schmitt, Physical Stability of Amorphous Pharmaceuticals: Importance of Configurational Thermodynamic Quantities and Molecular Mobility. J. Pharm. Sci.- 91, 1863–1872 (2002)

[5] J.Patterson, M.James, A.Forster, R.Lancaster, J.Butler, T.Rades, The Influence of Thermal and Mechanical Preparative Techniques on the Amorphous State of Four Poorly Soluble Compounds. J. Pharm. Sci.- 94, 1998–2012 (2005).

[6] L.Yu, Amorphous pharmaceutical solids: preparation, characterization and stabilization. Adv.Drug Deliv. Rev.- 48, 27–42 (2001)

[7] R.Capen, D.Christopher,P.Forenzo, C.Ireland,O.Liu,S.Lyapustina,J.O'Neill,N. Patterson, M.Quinlan, D.Sandell,J.Schwenke,W.Stroup, T.Tougas, On the Shelf Life of Pharmaceutical Products. AAPS PharmSciTech.- 13, 911–918 (2012)

[8] E.A.APogna, C.T.Rodriguez, G.Cerullo, C.Ferrante, J.V.Rodriguez, T.Scopigno, Probing equilibrium glass flow up to exapoise viscosities. Proc. Natl. Acad. Sci. U.S.A.- 112, 2331–2336 (2015)

[9] K.Adrjanowicz, K.Kaminski,Z.Wojnarowska, M.Dulski, L.Hawelek, S.Pawlus, M. Paluch, J. Phys. Chem. B.- 114, 6579–6593 (2010).

[10] B.Schammé, N.Couvrat,P.Malpeli, L.Delbreilh, V.Dupray, E.Dargent, G. Coquerel, Crystallization Kinetics and Molecular Mobility of an Amorphous Active Pharmaceutical Ingredient: a Case Study with Biclotymol. Int. J. Pharm.-490, 248−257. (2015)

[11] R.Ceolin, J.L.Tamarit, M.Barrio, D.O.Lopez, B.Nicolai,N.Veglio, M.A.Perrin, P. Espeau, Overall Monotropic Behavior of a Metastable Phase of Biclotymol,2,20-Methylenebis(4-Chloro-3-Methyl-Isopropylphenol), Inferred From Experimental and Topological Construction of the Related P-T State Diagram, J. Pharm. Sci.- 97, 3927–3941 (2008)

[12] K.Adrjanowicz, D.Zakowiecki, K.Kaminski,L.Hawelek, K.Grzybowska,M. Tarnacka ,M.Paluch, K.Cal, Molecular Dynamics in Supercooled Liquid and Glassy States of Antibiotics: Azithromycin, Clarithromycin and Roxithromycin Studied by Dielectric Spectroscopy.Advantages Given by the Amorphous State. Mol. Pharmaceutics- 9, 1748−1763. (2012)

[13] K.Kaminski, K.Adrjanowicz, Z.Wojnarowska,M.Dulski, R.Wrzalik, M. Paluch, E.Kaminska,A.Kasprzycka, Do Intermolecular Interactions Control Crystallization Abilities of Glass-Forming Liquids J. Phys. Chem. B- 115, 11537–11547 (2011)

[14] F.Kremer, A.Schönhals Broad Band Dielectric Spectroscopy, Springer, Berlin, Ch. 3 and 4 (2003)

[15] K.L.Ngai, M.Paluch, Classification of secondary relaxation in glass-formers based on dynamic properties. J. Chem. Phys.-120, 857–873. (2004)

[16] K.L.Ngai, Relation between some secondary relaxations and the α relaxations in glass-forming materials according to the coupling model. J. Chem. Phys.- 109, 6982–6994. (1998)

[17] G.P.Johari, M.Goldstein, Viscous Liquids and the Glass Transition. II. Secondary Relaxations in Glasses of Rigid Molecules. J. Chem. Phys.-53, 2372–2388 (1970).

[18] K.L.Ngai, Why the glass transition problem remains unsolved? J. Non-Cryst. Solids- 353, 709–718 (2007)

[19] F.Alvarez, A.Alegra,J.Colmenero, Relationship between the time-domain Kohlrausch-Williams-Watts and frequency-domain Havriliak-Negami relaxation functions. Phys. Rev. B–44, 7306–7312. (1991)

[20] S.Hensel-Bielowka, M. Paluch, K.L. Ngai, J. Chem. Phys.- 123, 014502 (2005)

[21] R.Macovez, E.Mitsari, M.Zachariah,M.Romanini, P.Zygouri, D.Gournis,J.Ll. Tamarit, Ultraslow Dynamics of Water in Organic Molecular Solids. J. Phys. Chem. C- 118, 4941−4950 (2014)

[22] R.Böhmer,K.Ngai, C.Angell, D.Plazek, Nonexponential relaxations in strong and fragile glass formers. J. Chem. Phys.- 99, 4201−4209 (1993).

[23] M.D.Ediger,P.Harrowell, L.Yu, Crystal Growth Kinetics Exhibit a Fragility-Dependent Decoupling from Viscosity. J. Chem. Phys.- 128, 034709–034714 (2008)

[24] K.Adrjanowicz,K.Kaminski,M.Paluch, K.L.Ngai,L.Yu, Study of dynamics and crystallization kinetics of 5-methyl-2-[(2-nitrophenyl)amino]-3-thiophenecarbonitrile at ambient and elevated pressure. J. Chem. Phys.- 136, 234509 (2012).

[25] R.Capen, D.Christopher, P.Forenzo, C.Ireland, O.Liu, S.Lyapustina, J.O'Neill,N. Patterson, M.Quinlan, D.Sandell, J.Schwenke, W.Stroup, T.Tougas, On the Shelf Life of Pharmaceutical Products. AAPS PharmSciTech.- 13, 911–918 (2012)

[26] M.Jiménez-Ruiz, A.T.Ezquerra, I.Sics, Fernández-Díaz.Crystallization of 2-propanol studied by neutron diffraction and dielectric spectroscopy in real-time. M. T. Appl. Phys. A-74 (Suppl. 1), S543−S545 (2002)

[27] A.Sanz,M.Jiménez-Ruiz, A.Nogales, D.MartínyMarero, T.A.Ezquerra, Hydrogen-Bond Network Breakage as a First Step to Isopropanol Crystallization. Phys. Rev. Lett.- 93, 015503 (2004).

[28] A.D'Amore, J.M.Kenny, L.Nicolais, V.Tucci, Dynamic-mechanical and dielectric characterization of PEEK crystallization.Polym. Eng. Sci.- 30, 314–320 (1990)

[29] M.Avrami, Kinetics of Phase Change. I. General Theory. J. Chem. Phys.- 7, 1103−1112 (1939)

[30] M.Avrami,Kinetics of Phase Change. II Transformation-Time Relations for Random Distribution of Nuclei. J. Chem. Phys.- 8, 212−224.(1940)

[31] B.Wunderlich, Macromolecular Physics. Crystal Nucleation, Growth, Annealing. Academic Press: London,- 2 (1976)

[32] J.Málek, Kinetic analysis of crystallization processes in amorphous materials Themochimica Acta- 355, 239−253 (2000).

[33] A.S.Schaafsma,H.Snijders, F.vanderWoude,J.W.Drijver, S.Radelaar, Amor-phous to crystalline transformation of Fe80B20. Phys. Rev. B- 20, 4423–4430 (1979)

[34] M.Çelikbilek, A.E.Ersundu, S.Aydın, Crystallization Kinetics of Amorphous Materials. In: Advances in crystallization processes- Ch. 6 (2012)

[35] P.Marsac, S.Shamblin, L.Taylor, Theoretical and Practical Approaches for Prediction of Drug-Polymer Miscibility and Solubility. Pharm. Res.-23, 2417−2426 (2006)

CHAPTER-6

Rotational relaxations in solid (1,1,2,2)Tetrachloroethane

6.1. Introduction

While conventional (atomic) solids are made of atomicconstituents with only translational degrees of freedom,so that their structure is totally determined by translationsymmetry and fundamental excitations are vibrational incharacter, in molecular solids, the constituent molecules possess also orientational (as well as internal) degrees offreedom, which leads to a richer variety of possible solid phases and to the existence of rotational excitations such as librations and orientational relaxations. A molecular solidcandisplay complete translational and rotational order, as ina molecular crystal, or complete roto-translational disorder, as in a molecular liquid. In between these two extremes,molecular solids also display phases (known as "mesophases") that have no counterpart in atomic solids: for example,phases in which all molecules have the same or similar orientation, but no translational order (liquid crystals), orphases in which the molecules average centres of mass occupy lattice positions while their orientations are disordered (orientationally disordered solids). Finally,molecules possessing distinct isomers may be present inthe same phase in different isomeric forms (conformationally disordered solids).Orientationally disordered (OD) phases are generally formed by relatively small globular molecules such as derivatives of methane**,[1–3]**neopentane**[4]**adamantine **[5]** or fullerene**,[6]** or by small linear ones such as ethane derivatives**[7–9]** and dinitriles**.[10]**OD solids exhibit many of the phenomenological features of glass formers, displaying in particular a co-operative rotational motion, called α relaxation, that undergoes a continuous, dramatic slow-down upon cooling**,[11,12]** leading in some cases toa glass-like transition associated with rotational freezing**.[13,14]**Contrary to structural glasses, which do not exhibit any long-range order, OD phases are characterized by a translationally ordered structure and can therefore be more thoroughly characterized with the help of

methods that exploit the translational symmetry such as Bragg diffraction, lattice models, or solid-state nuclear magnetic resonance spectroscopy. Evenmore importantly, since OD phases are generally formed by molecular species with a simple structure and low number of atoms, solid-state molecular simulations are computationally affordable and can be performed with a relatively large number of molecules. This advantage allows an exact identification of the cooperative and non-cooperative molecular motions taking place in an OD phase, as we show here for the case of a chemically very simple molecule, namely, (1,1,2,2) tetrachloroethane, $C_2H_2Cl_4$ (hereafter TCE).TCE is known to exist in three molecular conformers(gauche+, gauche−, and trans, two of which are shown in Figure 6.1) depending on the phase and to display a rich phase diagram depending on temperature, pressure, and thermal treatment**.[15,16]**

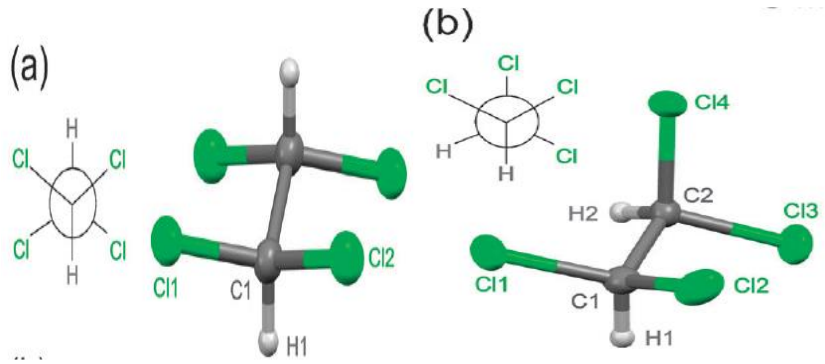

Figure (6.1): Scheme and molecular structure of the trans (a) and gauche$^+$(b) conformer of (1122) Tetracloroethane (after Ref. [15]).

1,1,2,2-Tetrachloroethane ($C_2H_2Cl_4$) is a chlorinated derivative of ethane (C_2H_6). It has the highest solvent power of any chlorinated hydrocarbon. It is widely used as a solvent and as an intermediate in the industrial production of tricholoethylene, tetracloroethylene and 1,2-dichloroethylene.It is chemically a very simple molecule. At room temperature, TCE is liquid and consists both of gaucheand trans isomers, with the gauche conformers being slightlymore stable than the trans one**.**

[17]Molecular reorientational dynamics were reported in the orthorhombic phase consisting only of gauche+ conformers, where a full assignment of the dynamics was not so far reported**. [18]19]** In this chapter, we focus on the orthorhombic phase (β phase), stable at ambient pressure. By employing temperature-dependent dielectric spectroscopy, we identify three different dipolar relaxation dynamics. Comparison with molecular dynamics simulations allows assigning each relaxation to a specific molecular reorientation in the solid matrix. We identify in particular a cooperative dipolar relaxation associated with a reorientational dynamics in which the initial and final molecular orientations are the same. We find that this cooperative motion has a non-cooperative precursor relaxation. We also observed a fast dynamics associated with molecular fluctuations involving the population of higher energy (non-equilibrium) orientations. These results show that mesophases of even simple molecules can exhibit very rich orientational dynamics, associated with low-dimensional motions

6.2. Differential scanning calorimetry (DSC)analysis

At ambient pressure, thermodynamically stable phase of TCE exist below 231K isorthorhombic (β phase) ($P2_12_12_1$, Z = 8, Z' = 2), with all moleculesin the gauche+ conformation.[**15,16**] A metastable transitionto the γ phase appears by heating the structural glass obtained by rapid cooling of the liquid,which can beobserved in a limited temperature range. This metastable phase γ was found to be monoclinic ($P2_1/c$) withZ = 8 molecules in the unit cell and $Z'= 2$ in the asymmetricunit, with both gauche+ and gauche− conformers coexistingin the asymmetric unit**.[16]**At ambient-pressure, phase transitions can easily be identified in scanning calorimetry, as shown in Figure 6.2.Finally, at high pressures (above0.5 GPa), the stable phase at room temperature is a monoclinicphase ($P2_1/c$, Z = 2, $Z'= 0.5$) in which all molecules are in the transconformation.

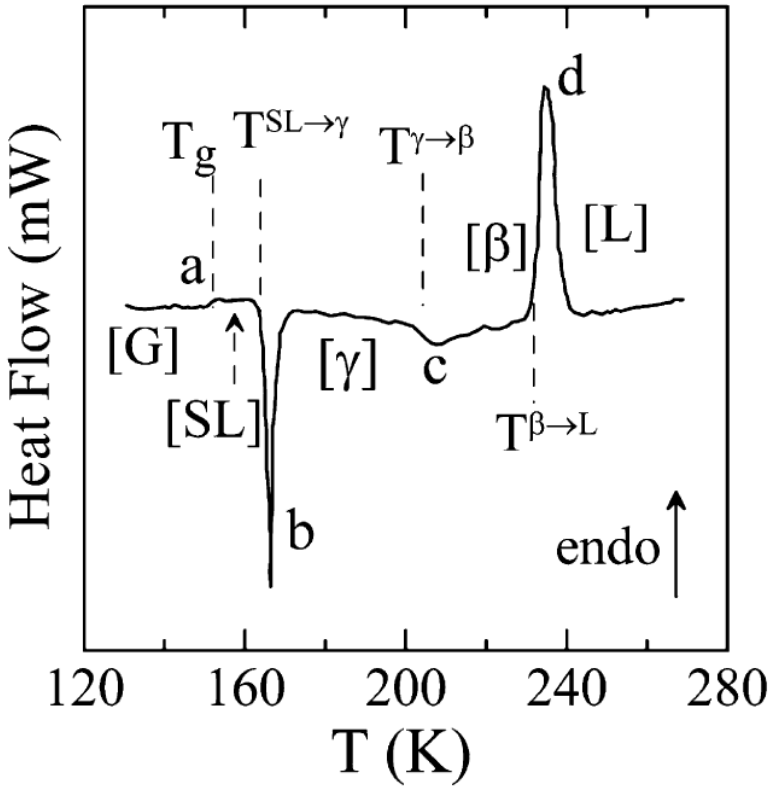

Figure (6.2): Differential scanning calorimetric curve recorded uponheating by 2 K min^{-1} the glass obtained from supercooledliquid. (a) glass transition temperature(Tg) from glass state to supercooled liquid$T^{G\rightarrow SL}$,(b) transition from supercooled liquid to solid phase (metastable) $T^{SL\rightarrow\gamma}$ (c) irreversible transition from metastable to stable phase $T^{\gamma\rightarrow\beta}$ (d) melting of phase β at $T^{\beta\rightarrow L}$.After Ref. [16].

6.3.Experimental Details

We performed temperature dependent dielectric spectroscopy experiments and Molecular dynamics simulation on TCE.

For dielectric measurements, liquid TCE was inserted inside the conventional parallel-platecapacitor by separating two plates with 50μm diameter spacers. Sample was placed in the sample holder which carefully inserted inside the cryostat where temperature is maintained by nitrogen flow. To obtainthe orthorhombic phase, the sample was cooled down to 130 K and then warmed up to 230 K (to avoid melting of the solid phase, see Figure 6.2).**[16]**The isothermal dielectric spectra was recoded always below thistemperature.

Molecular dynamics simulations of TCE were performed in the NVT ensemble by collaborators in Cordoba (Argentine). Rigid molecules were considered in gauche$^+$ configuration and intramolecular parameters were used from previously published X-ray diffraction data in Ref.**[16]**. The intermolecular interactions were described by Lennard-Jones (L-J) and Coulombic potentials**[22–25]** (see Ref. [**18**] for moredetails).NVT simulations were performed using the Gromacs v5.0.2 package,**[26]** using a leap-frog algorithm with a time step of 0.0005ps and a velocity rescale thermostat with a time constant of 2 ps. The experimental volume and the perfect crystalline structure determined by X-ray diffraction were used as initial configuration.**[15,16]** The system was formed by 800 molecules (6400 atoms), and some tests with a larger system of 6400 molecules (51200 atoms) were done in order to discard finite-size effects. Runs of 20000 ps were done, taking averages over the last 5000 ps. Some very large runs (300000 ps) were made for some temperatures in order to corroborate the shorter time results.

A couple of simulations were also carried out with non-rigid molecules in order to discard gauche-trans conformational jumps and to calculate the dynamic correlation between molecular orientations.A simulation was performed during 150000 ps for the largest system (6400 molecules). In these simulations, harmonic atom-atom forces, three-body harmonic angle potentials, and a four-body dihedral Ryckaert-Bellemans potential allowing torsion ofthe molecule around the C–C bond were included.**[27–29]**.We used this run in order to calculate the Kirkwood correlation factor.

6.4.Results and Discussions

6.4.1. Broad band dielectric spectroscopy results

Figure 6.3 shows the isothermal dielectric loss spectra ε``(f) of the orthorhombic phase(β phase) of TCE, displayed into two panel (6.3a and 6.3b) with two separate temperature ranges between 221.15Kto 145.15 K. At high temperature (Fig. 6.3(a)), the loss spectra exhibit a clear α process (reorientational dynamics) which is moving

towards high frequencyby increasing temperature as expected. At the highest temperature shown in this figure is 221.15 K, a background of dc conductivity coexists with α process. By plotting the dc conductivity spectra with respect to frequency (shown in the inset)for same temperature exhibits the dc plateau below roughly 1 Hz corresponding to the σ_{dc} value. A couple of loss spectra in figure (6.3a) also carry β process which is also displayed in (Fig. 6.3 (b)). The lower temperature spectra shown in figure 6.3(b) has an additional third feature labeled as γ. In this figure α loss is outside the depicted frequency range, so that the low-frequency background should be visible in the spectra which correspond to the high-frequency tail of such loss feature.

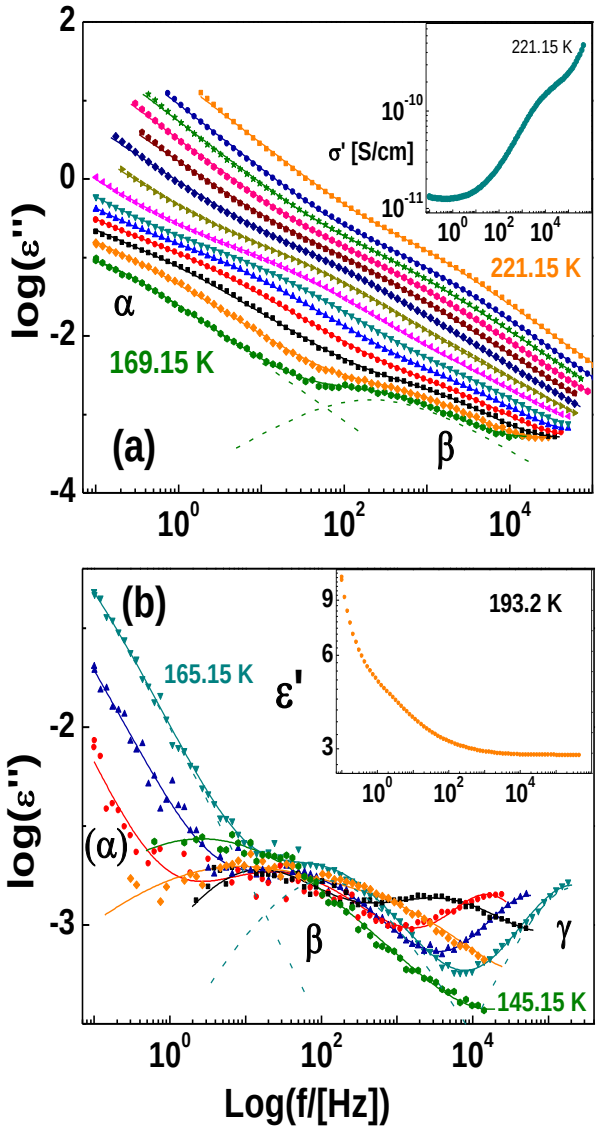

Figure(6.3): Dielectric loss spectra of orthorhombic TCE between 221.15 K and 169.15 K (a) and between 165.15 and 145.15 K (b), every 4 K, withcorresponding fits (continuous lines).Three molecular dynamic processes are visible, labeled, respectively, as α, β, and γ. Insets: logarithmic ac conductivityspectrumσ′(f) at 221.15 K (a) and permittivity spectrum ε′(f) at 193.2 K (b).

The real permittivity spectra ε′(f) (shown in the inset of Fig. 6.3(b) for the temperature of 193.2 K) are monotonically decreasing functions of frequency, as expected. At low frequency, instead of reaching a plateau value corresponding to the static permittivity ε_s, the spectra exhibit a steep increase with decreasing frequency (likely due to a conductivity orpolarization effect). Hence, the value of ε_s cannot be extracted directly from the real permittivity data. It is remarkable that a simple, rigid molecule like the gauche$^+$ conformer of TCE (Figure 6.1(b)) exhibits three distinct relaxation processes. In order to determine the origin of each relaxation process, we carried out a detailed quantitative analysis of spectra based on the fitting procedure detailed available in Chapter2. Each relaxation feature is modeled through a Cole-Cole function. The obtained characteristic times τ_α, τ_β, and τ_γ of the three relaxations are shown together as Arrhenius plots in Fig. 6.4. It may be observed that the temperature dependence of all three processes follows a simply activated (Arrhenius) behavior, given by

$$\tau = \tau_0 \, exp(E_a/k_B T) \qquad (1)$$

Here, the prefactor τ_0 is the value of the relaxation time in the limit of very high temperature, and E_a is the activation energy (energy barrier) for the process.**[30]**

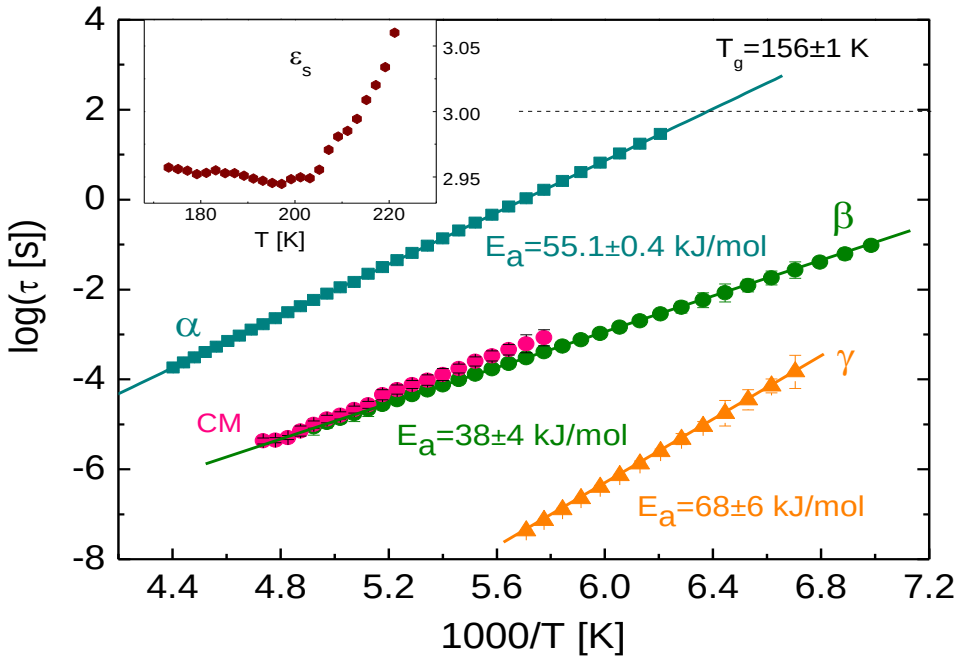

Figure (6.4): Arrhenius plot of the characteristic times of all three relaxationprocesses (α, β, and γ).Continuous lines are fits with the Arrhenius Eq. (1), and the dashed line indicatesthe glass transition temperature of α process. Filled circles (pink) with errorbars indicate the predicted relaxation time of the Johari-Goldstein precursor according to the Coupling Model (CM) (Eq. (2), see the text for more details).Inset: plot of the static permittivity ε_s as a function of temperature.

The fitting procedure also yields the dielectric strength (Δε) for each dynamic process. It may be observed from Fig. 6.3(a) that the strength of the α feature appears to increase slightly with increasing temperature. This is confirmed by ourfitting results; to better visualize such increase, in the inset to Fig. 6.4, we plot the static permittivity (ε_s) of solid TCE as a function of temperature. The value of ε_s was determined as $\varepsilon_s = \varepsilon_\infty + \Delta\varepsilon_\alpha + \Delta\varepsilon_\beta$, where $\Delta\varepsilon_\alpha$is the dielectric strength of the α, $\Delta\varepsilon_\beta$ is the strength of β and ε_∞ is the value of the real permittivity at frequency higher than the characteristic frequency of the β relaxation (and lower than the γ relaxation), where a plateau is visible in the ε´ spectra (see Fig. 6.5)

A graphical rationalization of our method to determine ε_s is shown in Figure (6.5).

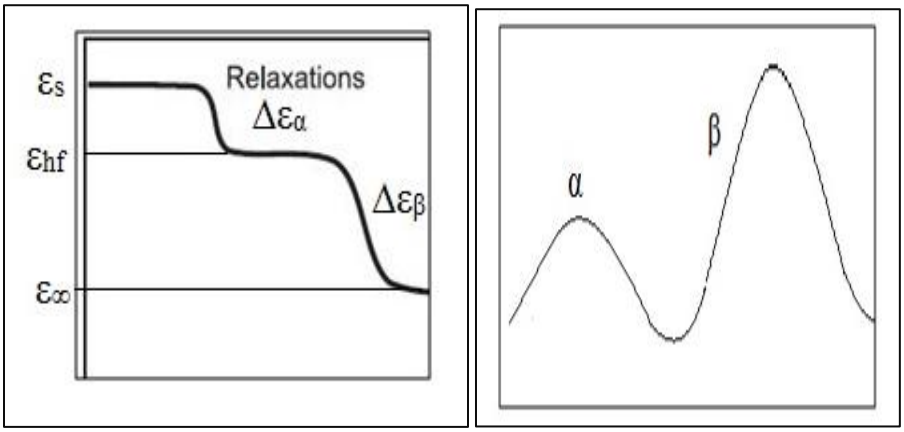

Figure (6.5):Schematic representation of the real (a)and imaginary (b) parts of the permittivity spectra when two relaxations are present in the experimental frequency window. In this cartoon, all conductivity contributions and all polarization effects other than orientational polarizability are absent. $\Delta\varepsilon_\alpha$ is the strength of α relaxation, equal to the difference$\varepsilon_s - \varepsilon_{hf}$, and $\Delta\varepsilon_\beta$ is the strength of β relaxation, equal to $\varepsilon_{hf} - \varepsilon_\infty$.

Given that $\Delta\varepsilon_\alpha$ is roughly two orders of magnitude higher than $\Delta\varepsilon_\beta$ and ε_∞ is basically constant, the temperature dependence of the static permittivity follows that of the dielectric strength of the primary relaxation.

It may be observed in the inset of Fig. 6.4 that ε_s initially decreases slowly with increasing temperature, but upon approaching the melting point at 231 K,**[15]**it exhibits a steep increase. The initial decrease is consistent with the general expectation that $\Delta\varepsilon_\alpha$ and ε_s decrease with increasing temperature because the alignment of mobile molecular dipoles with the applied field is hampered at high temperature by thermal motions. The steep increase close to the melting point, although inconsistent with this general trend, is however in agreement with the

results obtained in a similar system, namely, (1,1,2) trichloroethane, **[31]** where it was reported that the dynamic orientational disorder is more pronounced close to the melting while it is almost absent at lower temperature. TCE appears therefore to display a similar behavior, with more pronounced (dynamic) orientational disorder close to the melting point.

The Arrhenius parameters for the α relaxation obtained from the fit of the corresponding Arrhenius plot with Eq. (1) were E_a= 55.1±0.4 kJ/mol and log(τ_0/[s]) = −16.4 ± 0.2. The result for τ_0 is in the typical range of values for glass-forming materials.**[30]**The activation energy is somewhat higher than that reported for deuterated TCE (41 kJ.mol^{-1}).**[18]** The glass transition temperature was calculated as the temperature at which the Arrhenius Eq. (1) gave a value of τ_α equal to 100s. The obtained value, T_g = 156 ±1K, is close to the glass transition temperature of supercooled liquid TCE (153 K), as already pointed out in ref.**[18]** for deuterated TCE.

The characteristic times τ_α obtained by our fitting procedure matches roughly reported in a recent nuclear quadrupole resonance study on the orthorhombic phase of TCE.**[18]** This slowest relaxation process (α) corresponds to the cooperative motion associated with the glass-like freezing of the collective molecular motion (i.e., with a glassy transition).**[18]** The observation of the samerelaxation by means of dielectric spectroscopy implies that it is dipolar in character, i.e., it involves a change in the macroscopic polarization of the sample under the applied ac field. It is clear from Fig. 6.3(a) that the molecular motion corresponding to the α relaxation can be frozen without transition within an ordered crystalline phase, i.e., that a glassy state is reached.

Starting from the fitting parameters of the α relaxation feature, one may employ the so-called Coupling Model (CM)**[32]** to calculate the relaxation time τ_{CM} of the precursor relaxation (β relaxation) associated with the glass transition dynamics, i.e., the characteristic time of the (single-molecule) Johari-Goldstein

relaxation.**[33,34]** According to the CM, the relaxation time τ_{CM} of the precursor relaxation should be related with that of the primary process (τ_α) as:

$$Log(\tau_{CM}) = (1 - \beta_{KWW})\, log(t_c) + \beta_{KWW}\, log(\tau_\alpha) \qquad (2)$$

Here, t_c is a crossover time whose typical value is 2×10^{-12} s for both molecular and polymeric glass formers,**[32,35]** and β_{KWW} is the exponent of the stretched exponential function that describes the α spectral feature in the time domain. For the Cole-Cole exponent *d* of the function employed to fit the α feature (for more details see chapter2); the exponent is there indicated with the letter β, in analogy with the HN function, while here we use the letter *d* for clarity), the value of β_{KWW} can be accurately estimated as $\beta_{KWW} \cong d^{1/1.23}$.**[36,37]**The theoretical precursor time τ_{CM} calculated using Eq. (2) is shown in Fig. 6.3 together with the experimental values for all three relaxation times. It can be observed that τ_{CM} matches rather closely the experimental values for τ_β. Moreover, if the simply activated behaviors of both α and βrelaxations are extrapolated to high temperatures, they are observed to intersect at high temperature (~500 K), where both characteristic times are roughly equal and given by $\log(\tau_\alpha)\approx\log(\tau_\beta)\approx-11$. We can therefore conclude that the secondary β relaxation is the precursor relaxation associated with the primary relaxation.

Visual inspection of Fig. 6.3(b) reveals that the spectral position of the γ feature varies more rapidly with temperature than the β process. This is confirmed by the Arrhenius plot of Fig. 6.4, where it is observed that the γ relaxation has also higheractivation energy than the α process. Given that we already identified the β relaxation as the precursor of the primary relaxation, the γ process is not a precursor, single-molecule relaxation; moreover, it also cannot be an intramolecular relaxation, because the gauche$^+$ conformer is rigid and previous studies have already ruled out the existence of conformational fluctuations in the orthorhombic phase.**[15,16,18]**

6.4.2. Molecular simulations results

In order to identify the exact microscopic origin of theα andγ relaxations, we carried out detailed molecular dynamics simulations in this phase. The molecular structure of the gauche^{+} conformer present in orthorhombic TCE possesses a C_2 symmetry axis orthogonal to the C–C bond and midwaybetween the two carbon atoms. Due to the different electron affinity of hydrogen and chlorine species, the TCE molecule is dipolar, and by symmetry, its dipole moment is parallel to the C_2 axis (orthogonal to the C–C bond), oriented from thechlorine-rich to the hydrogen-rich region of the molecule. It was pointed out already inref.**[18]** that the only molecular dynamics present in orthorhombic TCE are two, namely, reorientational motions of the molecule between equivalent ground-state orientations (180^0 flips around the molecular symmetry axis) and between the ground-state orientation and a non-equilibrium orientation.

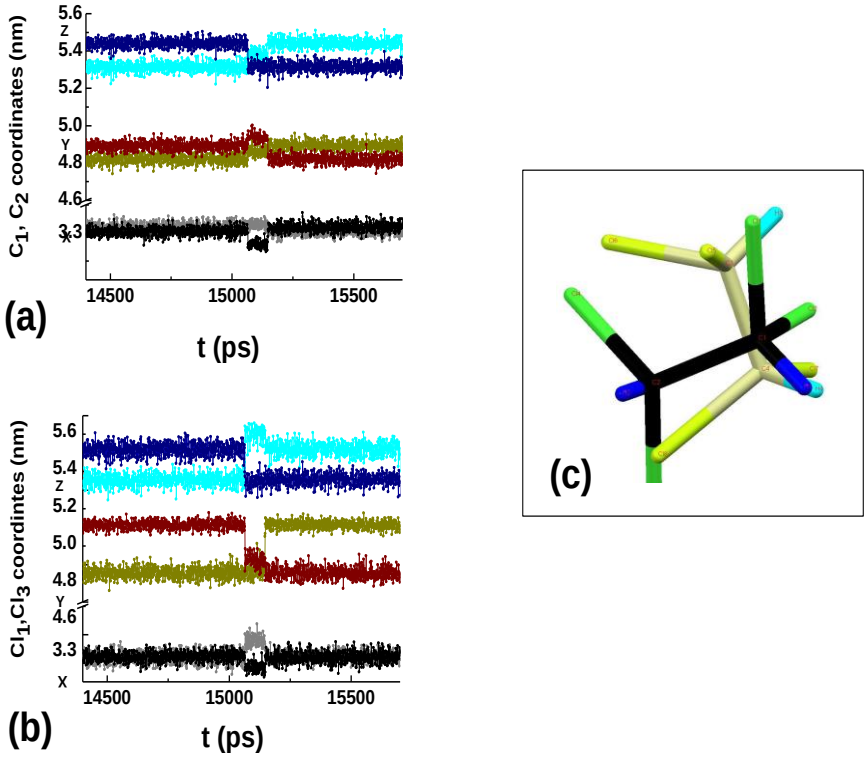

Figure (6.6):Carbon (a) and selected chlorine (b) coordinates of a TCE moleculeduring 1.5 ns of NVT molecular dynamics simulations covering the 180^0flipabout the molecular symmetry axis. (c) Relative orientation of the intermediatestate attained during such reorientational motion (yellow) with respect tothe initial/final state (black).

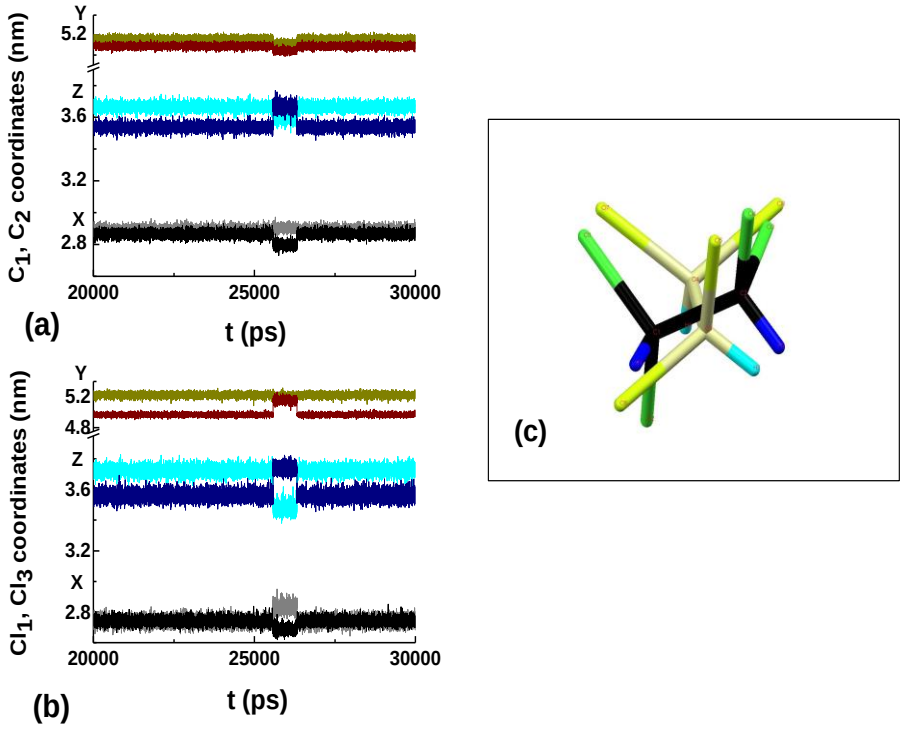

Figure (6.7): Carbon (a) and selected chlorine (b) coordinates of a TCE moleculeduring 10 ns of NVT molecular dynamics simulations covering a dynamictransition to and from a high-energy orientational state. (c) Relative orientationsof a TCE molecule in the high-energy orientation (yellow) as comparedto the ground-state orientation (black).

The first dynamic process is in fact a positional exchange of C, H, and Cl atoms in the molecule, associated with a 180^0 rotation about the molecular symmetry axis. This motion is depicted in Fig. 6.6, where the coordinates of two carbon (a) and two chlorine (b) atoms of a given molecule are shown during one and a half nanoseconds of simulation covering such a reorientation process. The initial and final coordinates show clearly the exchange between the two carbons and thetwo shown chlorine atoms. Although the initial and final states are identical (they correspond in fact to a rotation by 0^0 or 180^0 around the C_2 molecular symmetry axis), during the transition between the two states, the molecule passes through an intermediate state with a different direction of the symmetry axis, shown in Fig.

6.6(c). This entails that such dynamics is visible with dielectric spectroscopy (while a rigid rotation around the symmetry axis would not be). We notice that $180^{\mathbf{0}}$ rotations represent the typical dynamic motions of elongated molecules in the liquid phase (see, e.g., ref.**[38]** and references therein); here, however, the rotational dynamics occurs in the solid phase, where steric hindrance is enhanced.

The other dynamic process is the temporary population of a higher-energy state. The relative orientation of the initial (ground) and final (higher-energy) states is depicted in Fig. 6.7(c), while the other panels of Fig. 6.7 describe the positionsof the two carbons (a) and two chlorines (b) during 10 ns of simulation covering such a back-and-forth reorientation. It may be observed comparing Figs. 6.6(b) and 6.7(b) that the positions of the chlorine atoms in the intermediate step are different in the two dynamic processes. Since the possible molecular orientations in chloroethanes are determined to a large extent by the steric hindrance between the bulky chlorines atoms, **[31]** the two intermediate orientations shown in Figs. 6.6(c) and 6.7(c) correspond to states of different energy.Since a collective fluctuation involving a large population of molecules in the higher-energy state is energetically forbidden, we assign the γ process to the back-and-forth dynamics of Fig. 6.7(c), and the α relaxation to a cooperative reorientation involving the positional exchange of Fig. 6.6(c). This assignment is consistent with the observedactivation energies, as it is likely that a dynamic process between two states of different energy involves a higher energy barrier than a process between two equivalent states of same energy.

The β relaxation is therefore the precursor relaxation associated with the cooperative 180^0reorientational flips. The situation is reminiscent of the behavior of a solid phase of 2-adamantanone, which displays both a co-operative and a precursor relaxation associated with large-angle reorientational jumps.**[5]**However, contrary to the 2-adamantanone case, the initial and final states of the α relaxation are here indistinguishable. To the best of our knowledge, our findingis the firstexperimental observation by dielectric spectroscopy of a fixed angle reorientation where the initial and final states coincide. It is also the first time that a precursor relaxation is reported for such peculiar dynamics. This finding corroborates the idea that the Johari-Goldstein precursor relaxation is a fundamental

property of glass-forming materials, regardless of the type of disorder they display **[39]**(a Johari Goldstein precursor relaxation is also observed), for example, in molecular dynamics simulations of the 180^0 flips of elongated molecules in the liquid state [**38]**.It is interesting to analyze in more detail the static permittivity and dielectric strength of the α relaxation. The dielectric strength of a cooperative process can be written, according to the Kirkwood-Fröhlich equation, **[30]**as

$$\Delta\varepsilon = \varepsilon_s - \varepsilon_{hf} = \frac{g}{3\varepsilon_0}\frac{\varepsilon_s\,(\varepsilon_{hf}+2)}{3(2\varepsilon_s+\varepsilon_{hf})}\frac{\mu^2}{k_B T}\frac{N}{V} \qquad (3)$$

In this expression, ε_s is the static value of the permittivity, already discussed above, while ε_{hf} is the value of ε´ at a frequency just above that of the α relaxation (in fact, due to the Kramers–Kronig relation,**[30]** each relaxation loss corresponds to a separate step-like decrease in the real part of the permittivity). Of the other parameters appearing in Eq. (3), μ is the molecular dipole moment, N/V is the number density of dipoles, and g is the so-called Kirkwood correlation factor**[40,41]** describing the degreeof correlation between the relative orientations of nearest-neighbor dipoles during the reorientation dynamics. The Kirkwood factor can be calculated as

$$g = \frac{\vec{M}.\vec{M}}{N\mu^2} = \frac{\langle|\vec{M}|^2\rangle}{N\mu^2} \qquad (4)$$

Here,$\vec{M}$ is the total electric dipole moment vector of N molecules, and the angle brackets denote a time average. We determined the factor g starting from our simulation data. The total dipole moment,$|\vec{M}|$, was calculated for the whole set of molecules used in the simulation (6400), and the average was performed over a relatively large time span. Using the value of the dipole moment provided by oursimulation (μ = 2.1 D), the Kirkwood factor at 215 K is found to be equal to 0.06, which is quite low, indicating a largely antiparallel orientation of the molecular dipoles.

To compare this value with the experiment, we first determined the high-frequency value of the real permittivity, ε_{hf}, using the static one and the dielectric strength of the primary relaxation, as $\varepsilon_{hf} = \varepsilon_s - \Delta\varepsilon_\alpha$ (see Figure 6.5). This was necessary because it was not possible to reliably separate the contribution of the α and β relaxations to the ε' spectrum. It should be noted that the strength of the β process is two orders of magnitude smaller than α process, so that the contribution ofthe β process in any of the dielectric quantities in Eq. (3) is very small. To evaluate the other terms in Eq. (4), we used the reported value for the number density of molecules at 215 K, namely, $(1/149.3) \times 10^{30}$ molecules per cubic meter.**[15]** Using the value of μ given above and the experimental valueε_s =3.05 of the static permittivity of solid TCE at 215 K at ambient pressure (see inset to Fig. 6.3(b)), the experimental estimate of the Kirkwood correlation factor is found to be of the order of $g \approx 0.2$. Such value is similar to those reported for OD solids formed by adamantane derivatives. **[5,42]**

It should be observed that g is zero for a perfectly ordered solid with no net dipole moment; for example, $g = 0$ by symmetry for a perfectly ordered orthorhombic unit cell of TCE, due to the antiparallel alignment of neighboring dipole moments. The value of g (and thus indirectly the value of ε_s) therefore measures the correlation between the next-neighbor orientations of the dipole moments as they rearrange by the α dynamics, since the contribution due to the equilibrium structure vanishes. Eq. (3) is strictly valid only for an isotropic medium such as a supercooled liquid or a translationally ordered cubic phase, so that the experimental value of g can only represent a first approximation for an anisotropic medium such as orthorhombic TCE. It is observed nevertheless that the experimental estimate is of the same order of magnitude as that obtained by molecular dynamics simulation, both differing only by a factor of three. Regardless of its exact numerical value, the fact that g is close to zero not only confirms the cooperative nature of theα relaxation (as g=1 for a gas phase of non-interacting dipoles) but most importantly it implies the tendency of the molecular dipoles to maintain on average their antiparallel alignment during such reorientation process. The cooperative nature of the α process likely results both from steric interactions, which only allow specific relative molecular

orientations in a densely packedsolid, and from dipole-dipole interactions, which prevent the build-up of macroscopic dipole moments.

6.5.Conclusions

We investigated the dipolar dynamics in the orientationally disordered solid phase of a simple ethane derivative, namely, (1,1,2,2) tetrachloroethane, by means both of dielectric spectroscopy and molecular dynamic simulations. Unexpectedly, three distinct orientational dynamics are observed in the solid phase, all characterized by a simply activated temperature dependence. The slower (α) process is the cooperative rearrangement of molecules in which each molecule undergoes a rotation by 180^{0} around the molecular symmetry axis and simultaneously a double reorientation of such axis from aninitial direction to a roughly orthogonal one and then back to the original molecular orientation and position, in what could be termed a positional-exchange relaxation. The intermediate process (β_{JG}) is the Johari- Goldstein precursor relaxation of theα process, and its relaxation time can be accounted for by the Coupling Model.Finally, the fastest (γ) dynamics is a non-cooperative process that corresponds to the reorientation of a single molecule in a higher-energy orientation. The glassy transition temperature as determined by the freezing of the cooperative α motionsin dielectric spectroscopy is remarkably close to the glasstransition temperature of the supercooled liquid of the same compound; this is even more surprising if one considers that in the liquid two distinct isomeric forms of the molecule are present, while only one of them is present in the solid. The Kirkwood correlation factor (*g*) for the α relaxation indicates that the molecular dipoles maintain on average a strong antiparallel alignment during their collective reorientational motion, mimicking the equilibrium relative orientations in the unit cell. To the best of our knowledge, this is the first observation by dielectric spectroscopy of a fixed-angle reorientation where the initial and final states coincide, and of the existence of a Johari-Goldstein precursor associated with such a dynamics.

Bibliography:

[1] M.Zuriaga,L.C.Pardo, P.Lunkenheimer, J.Ll.Tamarit, N.Veglio, M.Barrio, F.J.Bermejo, and A.Loidl, Phys. Rev. Lett.103, 075701 (2009).

[2] L.C.Pardo, J.Ll.Tamarit, N.Veglio, F.J.Bermejo, and G.J.Cuello, Phys.Rev. B ,76, 134203 (2007).

[3] Sz.Pothoczki, A.Ottochian, M.Rovira-Esteva, L.C.Pardo, J.Ll.Tamarit,and G.J.Cuello, Phys. Rev. B 85, 014202 (2012).

[4] J.Reuter, D.Busing, J.Ll.Tamarit, and A.Wurflinger, J.Mater. Chem. 7, 41-46 (1997).

[5] M.Romanini, Ph.Negrier, J.Ll.Tamarit, S.Capaccioli, M.Barrio, L.C.Pardo, and D.Mondieig, Phys. Rev. B 85, 134201 (2012).

[6] R.Macovez, A.Goldoni, L.Petaccia, P.A.Bruhwiler, and P.Rudolf, Phys. Rev. Lett. 101, 236403 (2008).

[7] G.Vdovichenko, A.Krivchikov, O.Korolyuk, J.Ll.Tamarit, L.C.Pardo, M. Rovira-Esteva, F.J.Bermejo, M.Hassaine, and M.Ramos, J.Chem. Phys. 143, 084510 (2015).

[8] M.Rovira-Esteva, N.A.Murugan, L.C.Pardo, S.Busch, J.Ll.Tamarit, Sz. Pothoczki, G.J.Cuello, and F.J.Bermejo, Phys. Rev. B,84, 064202 (2011).

[9] Ph.Negrier, M.Barrio, J.Ll.Tamarit, and D.Mondieig, Cryst. Growth Des. 13, 782–791 (2013).

[10] M.Zachariah, M.Romanini, P.Tripathi, M.Barrio, J.Ll.Tamarit, and R.

Macovez, J. Phys. Chem. C 119, 27298–27306 (2015).

[11] R.Brand, P.Lunkenheimer, and A.Loidl, J. Chem. Phys. 116, 10386–10401 (2002).

[12] M.Romanini, J.C.Martinez-Garcia, J.Ll.Tamarit, S.J.Rzoska, M.Barrio, L.C.Pardo, and A.Drozd-Rzoska, J. Chem. Phys. 131, 184504 (2009).

[13] A.Criado, M.Jimenez-Ruiz, C.Cabrillo, F.J.Bermejo, R.Fernandez-Perea, H.E.Fischer, and F.R.Trouw, Phys. Rev. B 61, 12082–12093 (2000).

[14] M.Zachariah, M.Romanini, P.Tripathi, J.Ll.Tamarit, and R.Macovez, Phys. Chem. Chem. Phys. 17, 16053–16057 (2015).

[15] M.Bujak, D.Blaser, A.Katrusiak, and R.Boese, Chem. Commun. 47, 8769–8771 (2011).

[16] P.Negrier, M.Barrio, J.Ll.Tamarit, D.Mondieig, M.J.Zuriaga, and S.C.Perez, Cryst. Growth Des.13, 2143–2148 (2013).

[17] J.P.Zietlow, F.F.Cleveland, and A.G.Meister, J.Chem.Phys.,24,142–146 (1955)

[18] S.C.Perez, M.Zuriaga, P.Serra, A.Wolfenson, Ph.Negrier, and J.Ll.Tamarit, J. Chem. Phys. 143, 134502 (2015).

[19] M.Bujak and A.Katrusiak, Z.Kristallogr. 219, 669–674 (2004).

[20] K.S.Cole and R.H.Cole, J.Chem. Phys. 9, 341–352 (1941).

[21] K.S.Cole and R.H. Cole, J.Chem. Phys. 10, 98–105 (1942).

[22] C.Caleman, P.J.vanMaaren, M.Hong, J.S.Hub, L.T.Costa, and D. vanderSpoel, J. Chem. Theory Comput. 8, 61–74 (2012).

[23] J.Wang, R.M.Wolf, J.W.Caldwell, P.A.Kollman, and D.A.Case, J.Comput. Chem. 25, 1157–1174 (2004).

[24] W.L.Jorgensen and J.Tirado-Rives, Proc. Natl. Acad. Sci. U. S. A. 102, 6665–6670 (2005).

[25] D.vanderSpoel, P.J. vanMaaren, and C.Caleman, Bioinformatics 28,752–753 (2012).

[26] B.Hess, C.Kutzner, D.vanderSpoel, and E.Lindahl, J. Chem. Theory Comput. 4, 435–447 (2008).

[27] G.Allen, P.N.Brier, and G.Lane, Trans. Faraday Soc. 63, 824–832 (1967).

[28] R.J.Abraham and R.Stolevik, Chem. Phys. Lett. 77, 181–185 (1981).

[29] T.Rydland and R.Stolevik, J.Mol.Struct.: THEOCHEM 105, 157–168 (1983).

[30] F.Kremer and A.Schonhals, Broad Band Dielectric Spectroscopy (Springer, Berlin, 2003).

[31]M.Bujak,M.Podsiadlo, and A.Katrusiak, Chem.Commun.37,4439–4441 (2008)

[32] K.L.Ngai, J.Non-Cryst. Solids 353, 709–718 (2007).

[33] G.P.Johari and M.Goldstein, J.Chem. Phys. 53, 2372–2388 (1970).

[34] K.L.Ngai, J.Chem. Phys. 109, 6982–6994(1998).

[35] J.Colmenero, A.Arbe, G.Coddens, B.Frick, C.Mijangos, and H.Reinecke, Phys. Rev. Lett. 78, 1928–1931 (1997).

[36] F.Alvarez, A.Alegra, and J.Colmenero, Phys. Rev.B44, 7306–7312 (1991).

[37] F.Alvarez, A.Alegra, and J.Colmenero, Phys. Rev. B 47, 125–130 (1993).

[38] D.Fragiadakis and C.M. Roland, Phys. Rev. E 88, 042307 (2013).

[39] S.Capaccioli, M.Paluch, D.Prevosto, Li-MinWang, and K.L.Ngai, J. Chem. Phys. Lett. 3, 735–743 (2012).

[40] J.G.Kirkwood, J. Chem. Phys. 7, 9-11 (1939).

[41] H.Frohlich, Theory of Dielectrics (Oxford University Press, London, 1958).

[42] J.C.Martinez-Garcia, J.Ll.Tamarit, S.Capaccioli, M.Barrio, N.Veglio, and L.C.Pardo, J.Chem. Phys. 132, 164516 (2010).

CHAPTER 7

Dielectric Studies of Pure Ethanolamine and Ethanolamine Intercalated in Graphite Oxide

7.1. Introduction

Hydrogen (H) bonding is a peculiar type of intermolecular interaction. Contrary to most other non-covalent interactions, Hbonds involve sharing of molecular hydrogens and are highly directional. H-bonding is responsible for a number of important effects in condensed matter: it plays a fundamental role for the ferroelectricity of order-disorder ferroelectric materials, it is responsible for the unusual properties of water and for aqueous solvation, it is an important ingredient for molecular recognition (e.g. between DNA pairs, or in chemical sensors such as taste receptors) and it accounts for the large molecular dipole moments of biopolymers (as in DNA helices).**[1,2]**Extended hydrogen bond networks can also lead to a particular type of charge transport, known as proton exchange or Grotthus mechanism, which is for example responsible for the relatively high dc conductivities of ice, water, or phosphoric acid.

In view of the importance of H-bonding for electric and dielectric properties, we investigate here the dielectric response of a small H-bond forming molecule, ethanolamine (C_2H_7NO). While in water all H-bonds are of the same type, namely O–H···O bonds with a proton being partially shared between two homonuclear (O) moieties, ethanolamine (EAM, Figure 7.1(a)) possesses two different H-bonding groups, namely an amine group ($-NH_2$) and an hydroxyl group (-OH), and can therefore form a larger variety of H-bonds.

We study ethanolamine (EAM) both in its pure bulk form and when confined as two-dimensional layers inbetween graphene oxide (GO, Figure 7.1(b)) sheets, to study the possible effect of dimensionality on H-bond formation and dynamics.

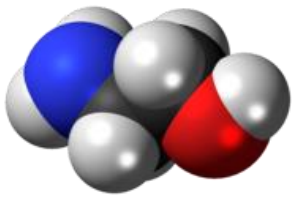

(a)

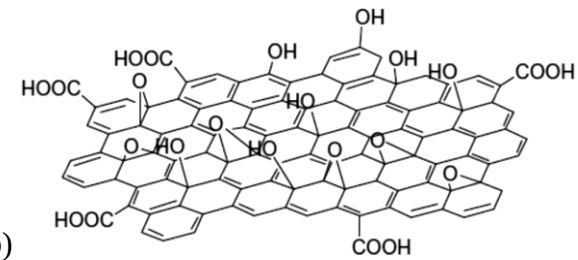

(b)

Figure (7.1): (a) the ethanolamine (EAM) molecule; (b) a graphene oxide (GO) sheet.

Ethanolamines (small molecules containing at least one hydroxyl group and one amine group) are widely used for production of emulsion paints and light detergents, and as chemical intermediates in plasticizers, corrosion inhibitors, rubber chemicals, lubricants and cutting fluids. Theyhave also wider applications in the pharmaceutical sector and as textile softening agents.

At room temperature, EAM is a highly polar liquid, with a dielectric constant of approximately 32, and an estimated average molecular dipole moment of 2.6 D. Similarly tothe case of chloroethanes (see Chapter 6), EAM displays different conformations depending on the phase. Compared to chloroethanes, however, the presence of hydrogen-bonding groups leads to stronger intermolecular interactions and thus to adifferent phase behaviour. For example, in the gas phase where intermolecular interactions are negligible, the stable form of EAM is a conformer with an intermolecular H-bond between the two polar groups and a dipole moment of only 2.27 D, shown in figure 7.2(a). Instead, in the stable solid phase, of monoclinic symmetry, the molecular conformation is much more open, with each molecule participating in 6 hydrogen bonds, both of the N–H···O and O–H···N types, as shown in Figure 7.2(b).**[3]**In the liquid, the local structure and the population of different conformers arestill debated.**[4, 5]**

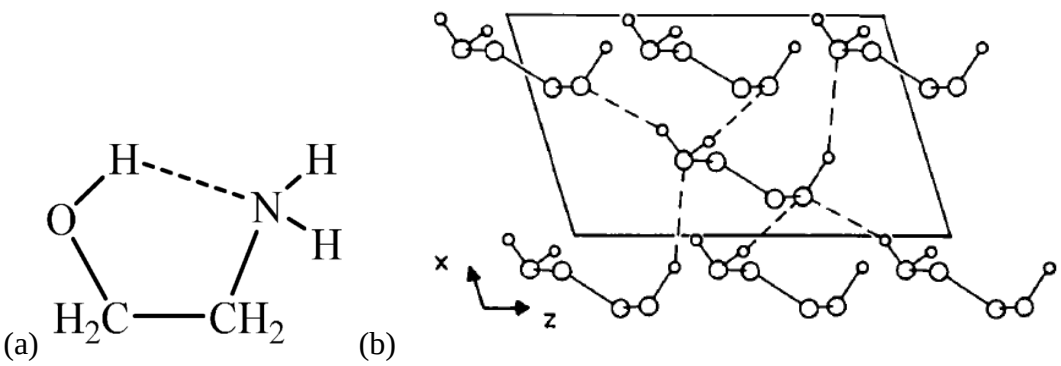

Figure (7.2): Hydrogen bonding in ethanolamine (EAM). (a) Intramolecular hydrogen bond in the EAM conformer stable in the gas phase. (b) The hydrogen-bonding motif in the stable crystal phase of EAM (after Ref. 3)

The frequency dependent dielectric behaviour of material provides information on conductivity and on the presence of molecular dynamic processes. The properties of ethanolamine, in this respect, have not so far been investigated by means of broadband dielectric spectroscopy nor

any other technique, and it is of interest to probe the relaxation behaviour of a system with more varied H-bonding motif with respect for example to ice, which displays a dielectric relaxation associated with the diffusion of H-bonding defects.**[6]**

7.2. Experimental Details

We carried out DSC, XRD and dielectric spectroscopy investigations onpure ethanolamine (EAM) both in its liquid and solid phases, as well as when intercalated inside graphene oxide sheets. In the solid form, we find that EAM displays a stable and a metastable crystal form. The dielectric relaxation spectra were measured over the frequency range of 10^{-1} Hz to 10^{9} Hz in the temperature range between 120 and 303 K. For the dielectric measurements, liquid ethanolamine (EAM) was placed at room temperature inside a home-made stainless steel parallel-plate capacitor especially designed for measuring liquid samples. The two plates were kept separated by needle-like cylindrical silica spacers of 50 μm diameter. The capacitor was then loaded in a nitrogen-gas cryostat for temperature control. Both low-frequency and high-frequency setups were used in this study. Dielectric relaxation losses were modelled as Havriliak-Negami functions (see Chapter 2).

The metastable crystalline form was obtained by fast-cooling the liquid at the fastest cooling rate available (10 K/min). The stable form was obtained either by slow cooling the liquid to just below the crystallization temperature, between 260 and 270 K depending on the cooling rate (the melting point of EAM is at 283 K), or by reheating the metastable phase to above 230 K (see subsection 7.4.1). For XRD measurements, liquid EAM was inserted into a Lindemann capillary and similar thermal treatment was applied to obtain the stable and metastable phases.

EAM intercalated inside graphene oxide (GO) was synthesized by intercalation chemistry techniques starting from pure EAM and pure graphite, by collaborators of the Layered and Nanoporous Materials Group of the University of Ioannina in Greece. Briefly, graphite was oxidized using the Staudenmeyer method and subsequently exfoliated by dissolving it in water. Hybrid nanocomposites membranes (flakes) were prepared by the solvent casting method.

In the procedure, the filler was directly added to the EAM solution (as purchased), ultrasonicated for 1 day, and stirred for another day at room temperature.After that, the dispersion was cast on a petri disk overnight to remove the solvents.The hybrid membranes were removed from the petri disk by immersing the glass plate in deionized water for several minutes. To reinforce the membrane, it was sandwiched and pressed between two Teflon plates

and placed in an oven at 420 K for about 15 min. All composite membranes produced by casting were subsequently treated by rinsing in: boiling HNO_3 solution (1 M) for 1 h to oxidize the organic impurities, 2) boiling H_2O_2 (3 vol%) for 1 h to remove all the organic impurities, 3) boiling deionized H_2O for 40 min three times, 4) boiling H_2 SO_4 (0.5 M) for 1 h to remove any metallic impurities, and again 5) boiling deionized H_2O for 40 min twice to remove excess acid. FollowingMacMillan et al. **[7]**, an additional purification procedure was performed to ensure the removal of paramagnetic contaminants. By this procedure membranes were soaked in ethylenediamine-tetraacetic acid (EDTA) solution (0.001 M) for 1 day followed by a thorough rinse. Then they were soaked in HCl (2 M) for 2 h followed by boiling in freshly distilled–deionized water to remove any residual acids, and the treatment with EDTA was repeated. Finally, rinsing in boiled deionized water was carried out three times to remove residual EDTA and the membranes were stored at room temperature in the fully hydrated state.The end productswere flakes of sub-millimetre thickness typical linear dimensions of several millimetres.

XRD measurements were carried out at the University of Ioannina to check successful intercalation of GO**[8]**. For BDS measurements, the largest flakes were selected and sandwiched between to stainless steel disks in a parallel plate configuration, and measured inside the same cryostat used for pure EAM samples.

7.3. DSC and XRD Results on pure EAM

Figure 7.3 shows the DSC thermograms acquired upon cooling liquid EAM and heating. Crystallization is observed at 250 K upon cooling. On heating a second exothermal process corresponding to a solid-solid transition is observed at approximately 220 K; the new crystal phase then melts at the melting point in the stable crystal form of EAM (280 K). These observations imply that, upon cooling, a metastable crystalline form of EAM is obtained. To verify this, we carried out a temperature-dependent XRD study.

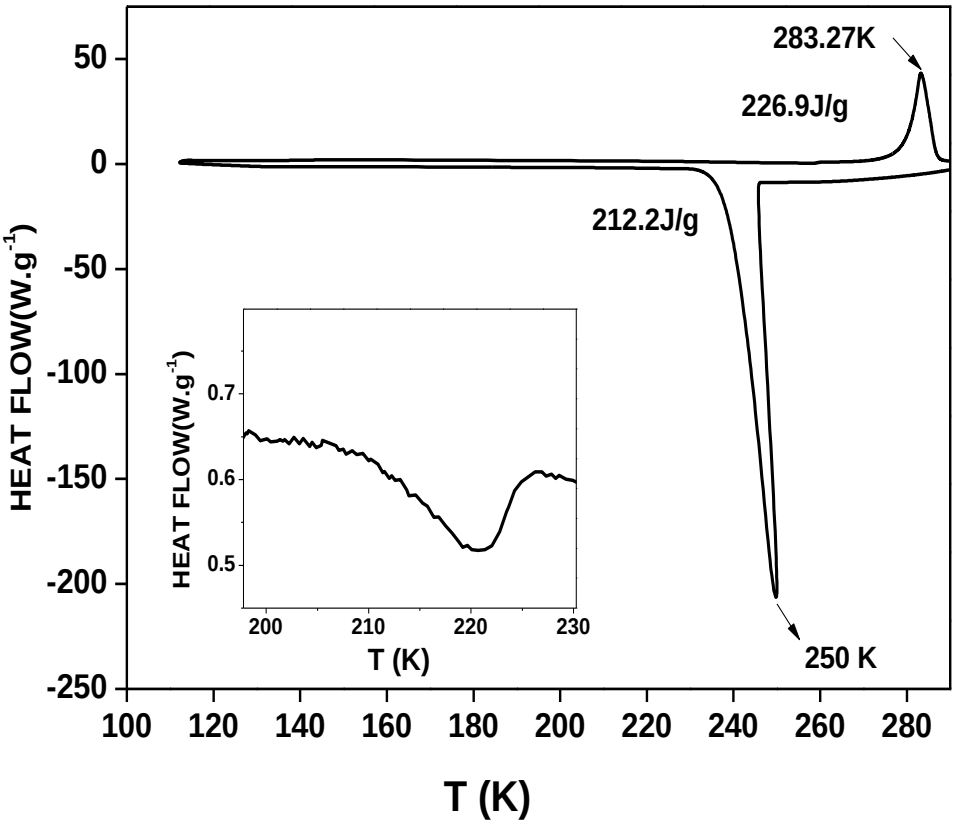

Figure (7.3): Calorimetry thermogram acquired upon cooling liquid EAM from room temperature at a rate of 10 K/min, and then upon heating. Inset: zoom-in of the heating thermogram to highlight the transitionfeature. An exothermic peak corresponding to crystallization of the liquid is observed at 250 K upon cooling. Upon heating, another exothermic feature, corresponding to a solid-solid transition is observed at around 220 K (see inset), well below the endothermic melting transition at 283 K.

Figure 7.4shows a series of diffraction patterns measured upon cooling liquid EAM to 210 K, then decreasing the temperature to 100 K, and then heating to 230 K. Every diffraction pattern was obtained after measuring during roughly one hour. The initial spectrum (blue) shows a totally different diffraction pattern than that corresponding to the stable phase.**[3]**This metastable structure is preserved upon further cooling to 100 K and then reheating to 210 K. In particular, the spectra measured at 150 K upon cooling and then heating (red and pink pattern, respectively), are virtually identical. Only the spectrum acquired upon re-heating at 230 K exhibits new diffraction peaks, which correspond to the stable phase (see below) and coexist, in this sample, with the ones of the metastable phase. The temperature of 230 K was chosen as it is only slightly above the onset of the solid-solid transitionobserved by DSC (see inset to Figure 7.3).

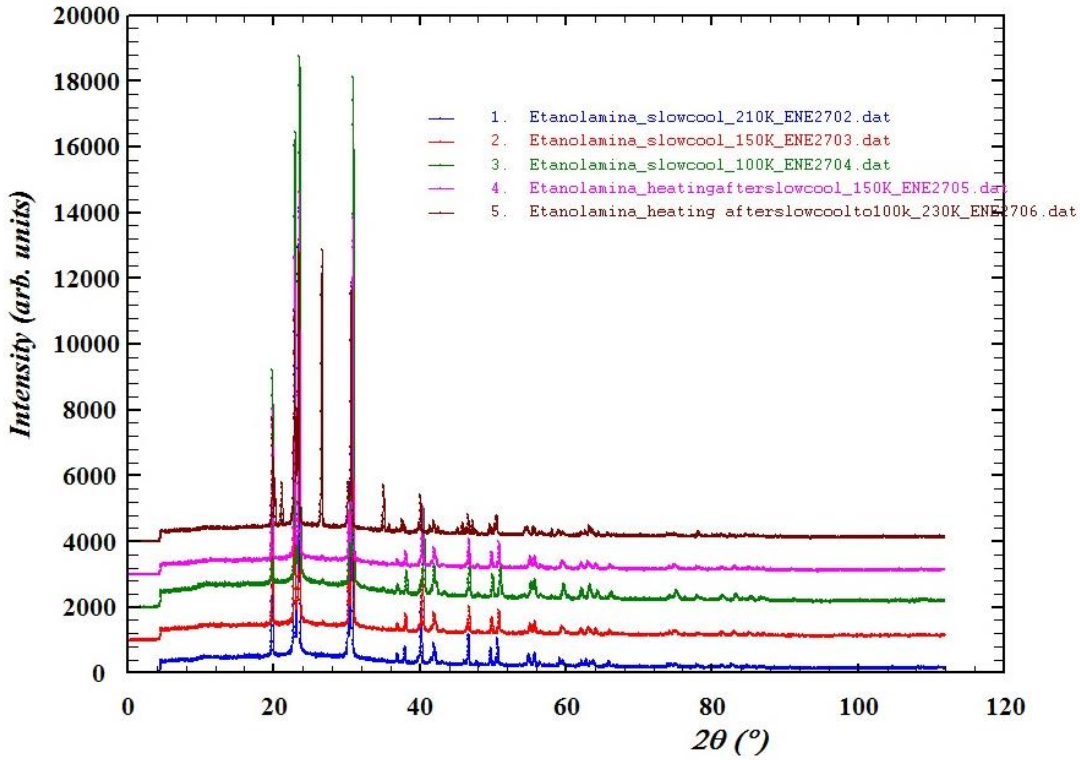

Figure (7.4): XRD patterns of the metastable solid phase of EAM, obtained by fast cooling the room-temperature liquid phase to 210 K. The series of patterns were acquired by performing a cool-heat cycle down to 100 K. Only the last spectrum, measured at 230 K after the cycle, shows the appearance of new peaks, corresponding to the stable crystal phase (see Figure 7.5)

Figure 7.5 shows a series of XRD spectra corresponding to initial cooling to 200 K to obtain the metastable phase, and then heating to 230 K and 270 K (i.e., just below the melting point). While the diffraction patterns of the metastable phase (Figure 7.4) are observed at first, again at 230 K the new diffraction peaks appear. At 270 K, the peaks of the metastable phase have disappeared, and the remaining peaks correspond to those of the stable crystallographic phase.**[7]**Anotherexperiment (not shown) showed that at 250 K the transformation from the metastable to the stable phase is already complete. The obtained phase is also observed to be stable upon further cooling down to 100 K (see Figure 7.5).

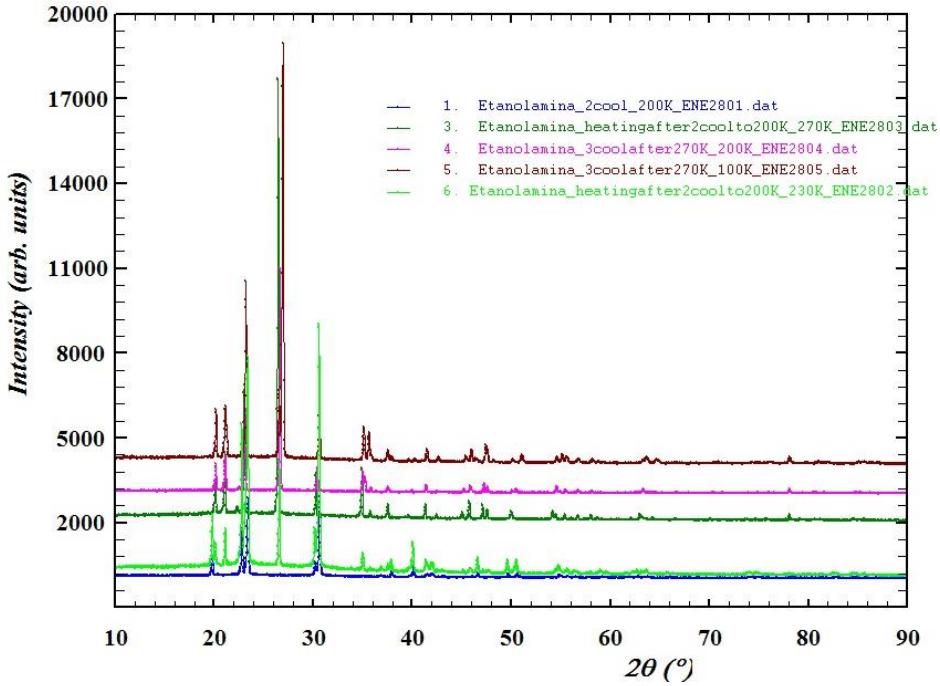

Figure (7.5): XRD patterns of the stable solid phase of EAM, obtained from the metastable phase by initial fast cooling to 200 K (blue pattern) and then heating to 270 K (dark green pattern). The phase is then stable down to at least 100 K (brown pattern).

Figure 7.6 shows the comparison between the diffraction patterns of the stable (red) and metastable (blue) phases at 100 K.Both phases have monoclinic symmetry, with different lattice parameters. In particular, the unit cell volume of the metastable phase is larger by a few cubic Angstroms with respect to that of the stable phase (different possible pattern matching solutions were found for the metastable phase, with volume of the unit cell larger by 1 to 3Åthan the stable one depending on the solution chosen).

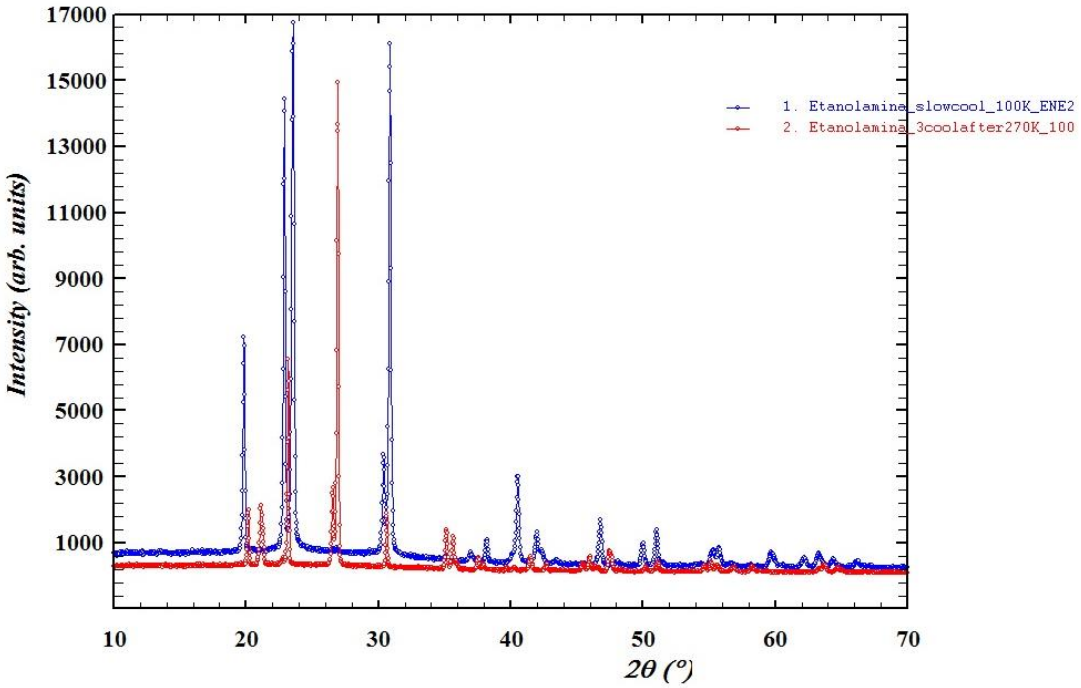

Figure (7.6): Comparison between XRD patterns of the stable (red) and metastable (blue) solid phases of EAM.

7.4. BDS Results on pure EAM

To study the metastable phase, liquid EAM was fast-cooled to 120 K. The stable phase was characterized by acquiring dielectric spectra while slow cooling from the liquid, or by cooling down from 270 K after transitionfrom the metastable phase. Both phases show a prominent relaxation feature in the temperature range above 120 K.

7.4.1.Phase behavior and dc conductivity of pure EAM

Figure 7.7 shows the loss spectra (upper panels) and dc conductivity spectra (lower panels) of a solid EAM sample obtained by fast cooling from the liquid phase to 120 K. Dielectric spectra were acquired every 2 K while warming the sample to above room temperature. Only the spectra in more significant temperature ranges are shown, both at low and high frequencies.

The low-frequency spectra clearly exhibit two major phase changes, visible as sudden jumps in the vertical scales of both permittivity and conductivity spectra. The first phase change is the solid-solid transition between the metastable phase obtained by quenching, and the stable phase. This transition occurs in the temperature range between 219 and 229 K, which

corresponds to the range observed by DSC (inset to Figure 7.3). The other phase change is the melting of the stable phase, which occurs between roughly 277 and 281 K, as expected.

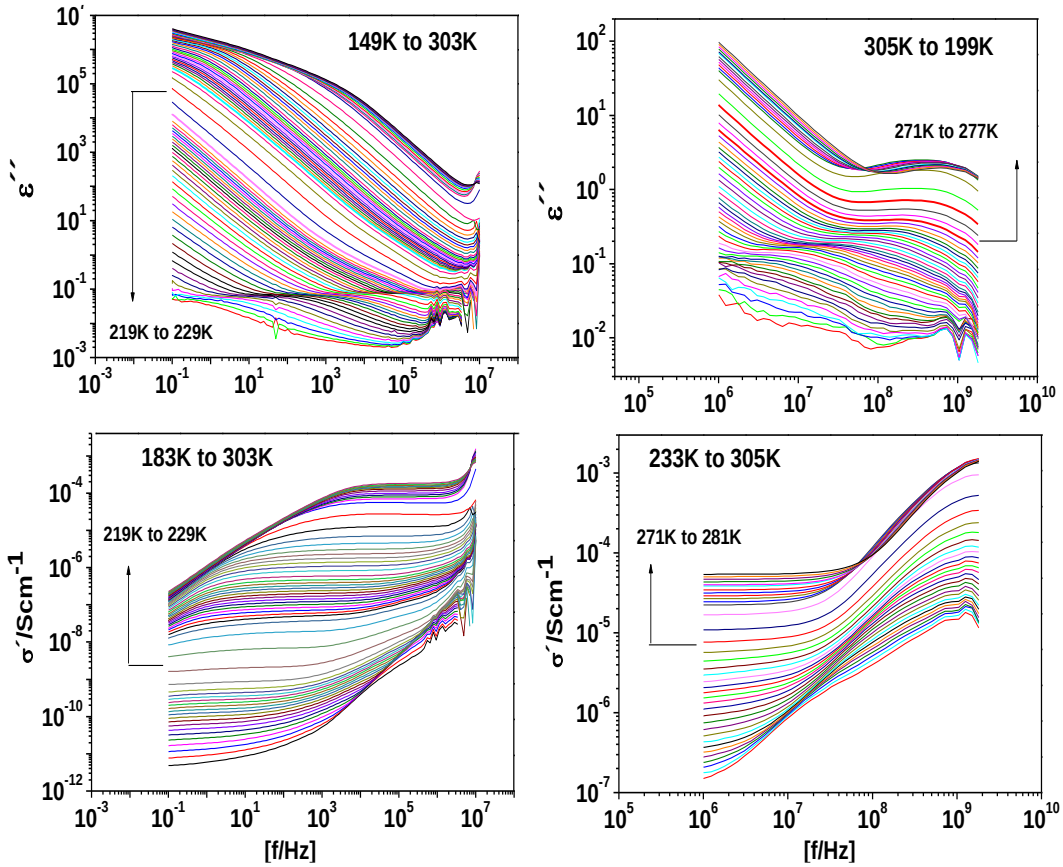

Figure (7.7): BDS spectra acquired across the transition between the metastable and stable crystal phases of EAM and upon melting of the latter phase, all measured upon heating every 2 Kboth with the low-frequency setup (left panels) and with the high-frequency setup (right panels). Both imaginary permittivity (upper panels) and real ac conductivity (lower panels) representations are shown.

Figures 7.8 and 7.9 show respectively the loss spectra and ac conductivity spectra of the stable phase with some spectra after the melting. In both figures, the data are shown at low and high frequencies, and both upon (slow) cooling and heating. In this case, only one transition is observed in the spectra, at the melting point.

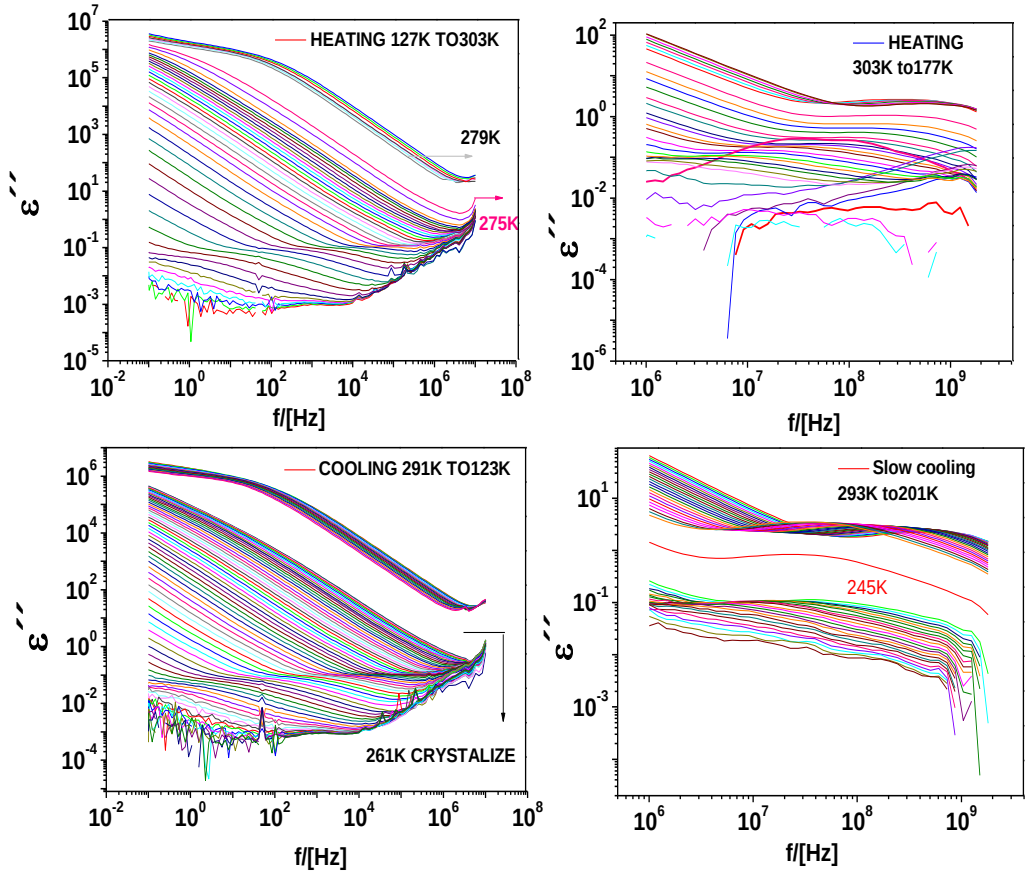

Figure (7.8): Loss spectra acquired on the stable crystal phase of EAM and across its melting. The spectra were measured every 2 K, both upon slow-cooling (lower panels) and upon heating (upper panels). Both the low-frequency setup (left panels) and with the high-frequency setup (right panels) were employed.

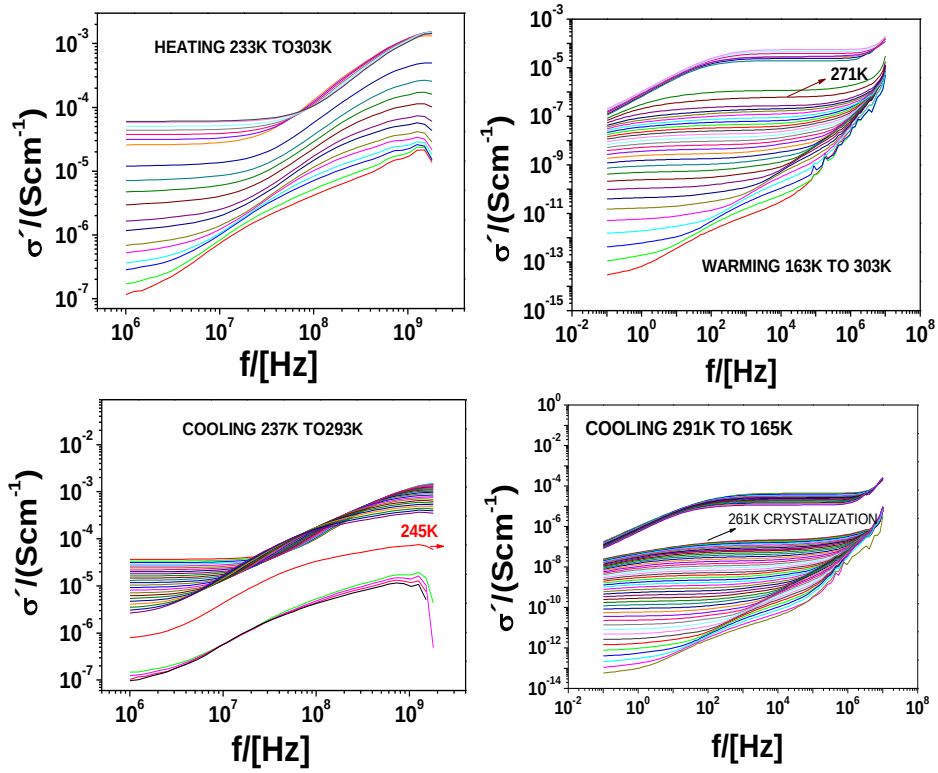

Figure (7.9): ac conductivity spectra corresponding to Figure 7.8.

Figure 7.10 shows the temperature-dependent dcconductivity values, as extracted from the spectra of Figure 7.9 and the lower left panel of Figure 7.7. The phase changes are clearly visible, as is the histeresis (a few tens of K) of the melting/crystallization transition of the stable crystallographic phase, which was also observed by DSC.

Interestingly, the dc conductivity Arrhenius plot exhibits a negative curvature (super-Arrhenius behavior) at low temperature, both in the metastable and stable solid phases. This negative curvature is a clear signature of ionic conduction in a disordered phase **[9,10]** which is an interesting finding for a solid phase, as not many solids behave as ionic conductors. The charge carriers may be small-ion or molecular impurities. It is not yet clear at this point whether such charge transport involves proton shuttling phenomena such as the Grotthus mechanism of ice.

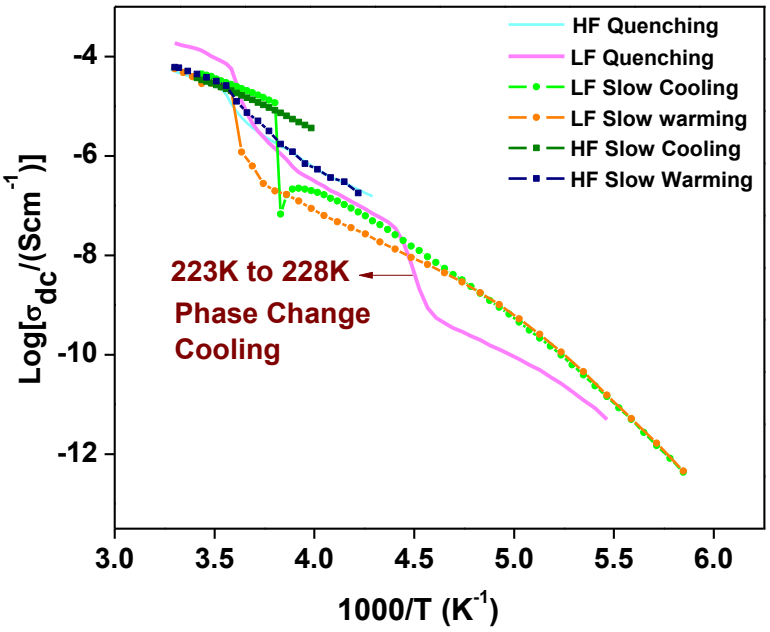

Figure (7.10): Arrhenius plot of the dc conductivity of the samples shown in Figure7.7 and7.9.

7.4.2. Dielectric losses in pure EAM

As visible in the upper panels of Figure 7.7 and in Figure 7.8, a clear relaxation loss is observed in both the metastable crystal phase, in the stable crystal phase, and even in the liquid phase at high frequency. In addition, in both solid phases a slower, weaker feature is also observed. The Arrhenius plot of the extracted relaxation times of these processes is shown in Figure 7.11.

Given the relatively low frequency and large width of the slow-frequency process, and its variability between different samples, we tentatively assign this feature to a conductivity effect. The more prominent relaxation at higher frequency deserves instead more attention. It can be seen in Figure 7.11 that such loss feature exhibits a quasi-continuous behavior as the phase changes from metastable crystal to stable crystal and even to liquid. This peculiar behavior of the main relaxation in EAM rules out both a conductivity origin (in fact, the conductivity varies by more than two decades across each transition), as well as an origin in terms of molecular dipolar motions: in fact, only a rototranslational relaxation can be expected in the liquid phase, while only pure rotational processes are in general expected in solid phases. Even in the rare cases where rototranslational diffusion occurs in the solid state [**9,10**] rotational motions are expected to display a dramatic change in characteristic time upon

melting; which is not the case here.Finally, it appears that the origin of the relaxation cannot be diffusion of H-bond defects as in ice, since also such process undergoes a dramatic acceleration upon melting(see Ref. **[6]** and references therein).

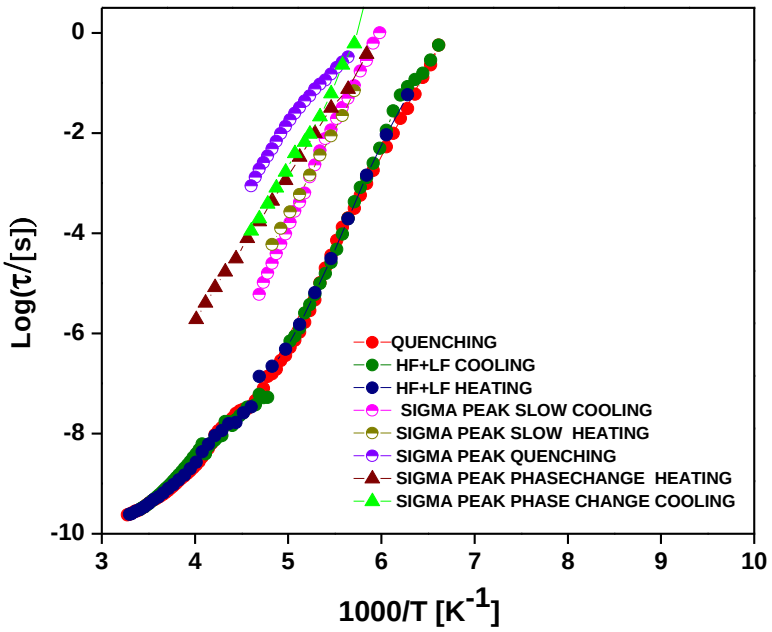

Figure (7.11): Arrhenius plot of the relaxation times of the dielectric losses visible in the samples shown in Figure 7.7 and 7.8.

From the Arrhenius plot of Figure 7.11, the freezing temperature of the high-frequency relaxation in EAM, that is, the estimated temperature at which the characteristic time of this process reaches 100 seconds, was estimated to be 140±4 K. It is worthwhile to mention that an enthalphy anomaly is observed in the low-temperature calorimetry thermogram of the metastable phase of EAM, as shown in Figure 7.12. The anomaly lies around 138 K, which matches approximately the freezing temperature obtained by BDS measurements (a slight difference between the two techniques might arise due to the different cooling/heating rates in each experiment).

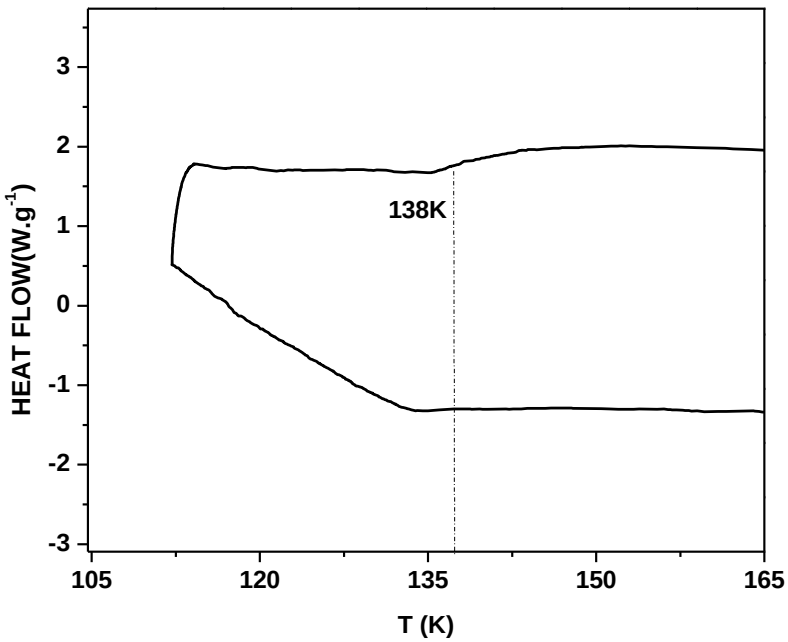

Figure (7.12): Calorimetrythermogram (on cooling, bottom part of the thermogram and heating, top part of the thermogram) acquired upon cooling liquid EAM from room temperature at a rate of 10 K/min.

Having ruled out several possible elementary interpretation of the observed dielectric relaxation, we propose an interpretation based on the H-bond network. In particular, the origin of the relaxation must be common to all studied phases. While the gas phase is characterized by intramolecular H-bonding, condensed EAM phases are characterized by inter-molecular bonding. Thermal energy in thesephases, and especially in the liquid phase, is sufficient to induce fluctuations in the molecular conformation of the EAM species and therefore in their H-bonding scheme. In view of this, we assign the main relaxation observed to fluctuations of the local dipole moments induced by rearrangements in the H-bonding motifs. They must be local fluctuations because the liquid state possesses no long range order. On the other hand, fluctuations present in the liquid state may survive in the solid phases, for examples at structural defects and grain boundaries. An exact microscopic identification of these H-bond fluctuations would require chemically sensititive, low-frequency techniques such as solid-state NMR spectroscopy.

7.5. BDS Results on pure EAM-intercalated GO

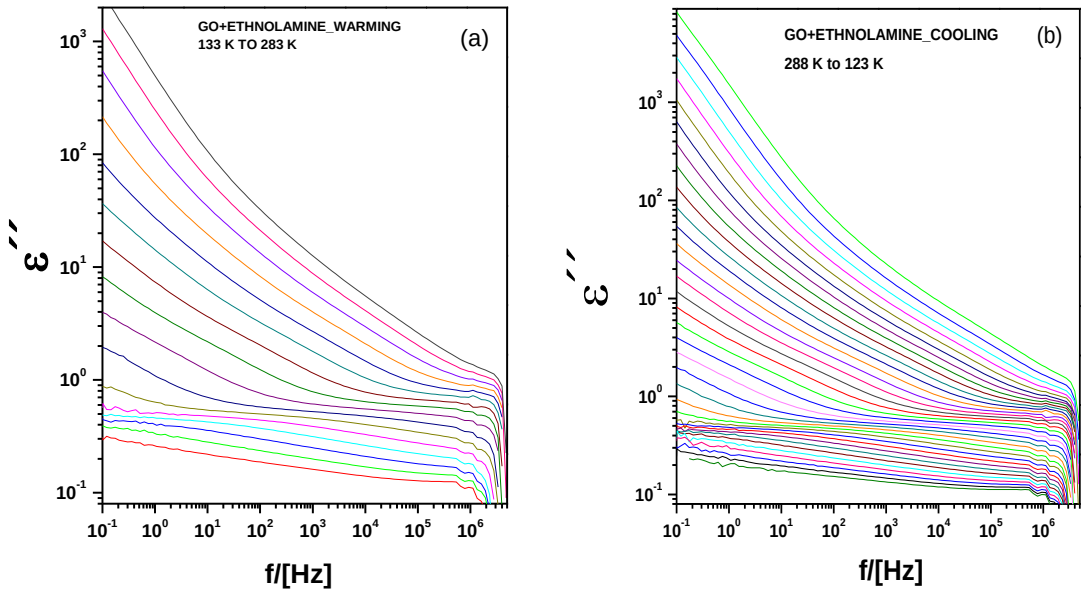

Figure (7.13): Permittivity spectra ofEAM-intercalated GO, both upon heating(a) and cooling (b)

Figure 7.13 shows the dielectric loss spectra of GO intercalated with ethanolamine, both upon heating(a) and cooling (b). A broad relaxation peak is observed, whose shape and frequency position is very different from that of water adsorbed on top of GO **[11]**, whereby we exclude that it can be due to water. Therelaxation time moves to higher frequencies as the temperature increases, as expected. The Arrhenius plot for the warm-up data is shown in Figure 7.14, together with that of pure EAM (stable phases). Due to the proximity of both relaxations and the fact that the main relaxation in pure EAM appears to be ubiquitous in all its phases, we assign the relaxation in EAM-intercalated GO to the same mechanism as in pure EAM, namely, to local dipolar fluctuations of the H-bond network.

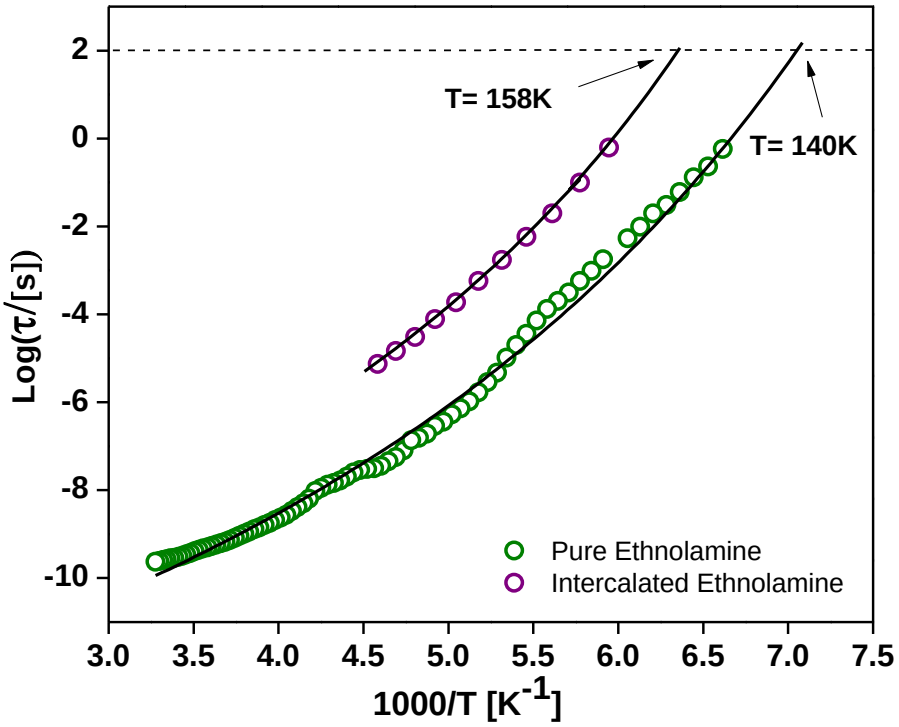

Figure (7.14): Arrhenius plot of the relaxation time of the dielectric loss observed in Figure 7.13(a) (EAM-intercalated GO upon heating). Continuous lines are fits with the VFT function. The extrapolated freezing temperature is also shown, as well as the comparison with pure EAM.

For the EAM-intercalated GO, the extrapolated freezing point of the main dielectric loss is approximately at 158K. The calculation of such freezing temperature is done using a fit of the experimental points with the VFT function.

The fact that the relaxation times and the freezing temperature of EAM intercalated inside GO are higher than those of pure EAM, indicates that molecular motions of ethanolamine are hindered when it is confined between GO layers, as one might expect. This is shown explicitly in Figure 7.15, where the loss spectra of pure ethanolamine and ethanolamine-intercalated GO are shown at the same measuring temperature for six distinct temperatures. It can be observed that the molecular motion is indeed slower for confined EAM. Also, the corresponding spectra are much broader, indicative of a wider distribution of relaxation time. This can easily be

rationalized, since while all ethanolamine molecules have the same molecular environment in bulk ethanolamine, this is not the case for intercalated GO, where ethanolamine can bind to different sidegroups or have distinct molecular environments (for example, it may be at different distances from the GO layers).

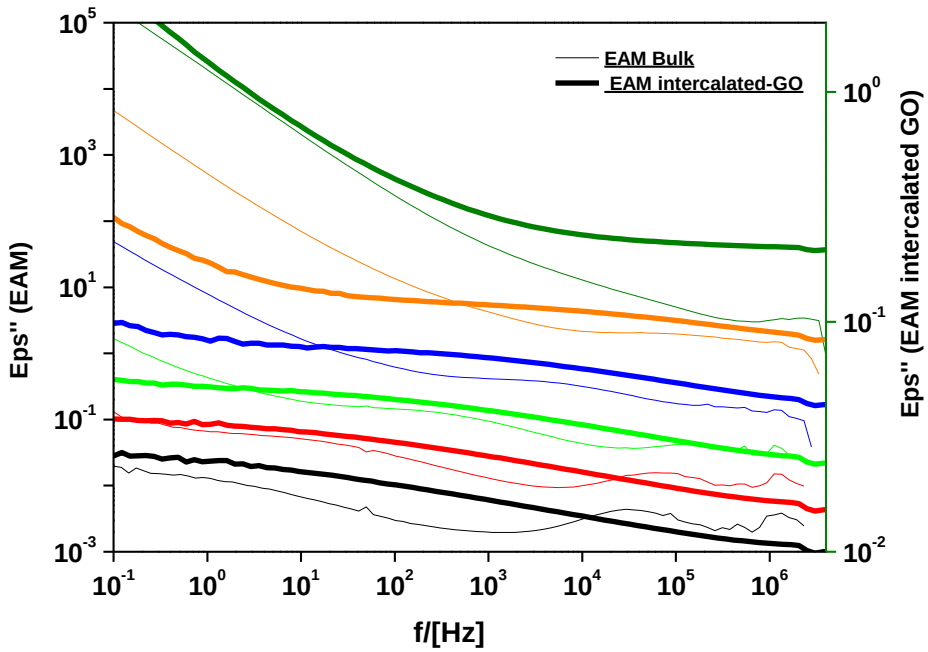

Figure (7.15): Comparison between theisothermal loss spectra of pure EAM (thin line) and those of EAM intercalated inside GO (thick line),for six different temperatures.

7.6. Conclusions

To summarize the information provided in this chapter, two solid phases have been observed in ethanolamine by means ofbroad band dielectric spectroscopy,XRD and DSC.Besides the stable crystallographic phase, a metastable phase is observedby fast cooling the liquid through the crystallization transition. By heating the metastable phase to above 230 K, this phase transform intothe thermodynamically stable phase, which then melts between277 and 281K. By cooling slowly, only the stable phase is formed. Both solid phases exhibit a dominant dc conductivity contribution from ionic charge carriers. While it is at present unclear whether these ions are protons or other small-ion impurities, the observation of ionic conductivity in solid phases is a quite interesting finding.

All phases of ethanolamine probed by dielectric spectroscopy, including notably the liquid phase, display a prominent dielectric loss, whose characteristic frequency does not vary substantially across phase transitions. This observation strongly suggest that this main relaxation is due to local fluctuations of the hydrogen bond network.The temperature dependence of the relaxation in the solid phases is sub-Arrhenius (VFT-like). The vitrification temperature of this process is found to be 140±4K by dielectric spectroscopy measurement; an anomaly is observed at138K in the DSCthermogram.Thesame relaxation process appears to be also presentwhen ethanolamine isintercalated between2Dsheets of graphene oxide (GO). Also in this case the temperature behaviouris VFT-like. Comparison of the isothermal dielectric spectra at the same temperature and of the extrapolated vitrification temperatures indicates lower dynamics in intercalated (confined) ethanolamine, due to bonding to the grapheme oxide sheets. The relaxation is broader in 2D ethanolamine, indicating a wider distribution ofrelaxation times.

Bibliography:

[1]M. Huang, J.Yu,X. Ma, Polymer Degradation and Stability 90,501-507,(2005)

[2]P.B.Undre, P.W. Khirade, S.B.Jagdale, S.N.Helambe, S.C.Mehrotra, Lithuanian Journal of Physics, Vol. 51, No. 2, pp. 147–154,(2011)

[3]D. Mootz, D. Brodalla, M. Wiebke, ActaCryst. C45,754-757, (1989)

[4]E.F.daSilva,T.Kuznetsova, B.Kvamme, K.M. MerzJr.J. Phys. Chem. B,111,3695-3703, (2007)

[5] Y.V. Novakovskaya, M.N. Rodnikova,Struct.Chem. 26,177–187,(2015)

[6] I.Popov, A.Puzenko, A.Khamzin, Y.Feldman,Phys.Chem.Chem.Phys.,17,1489-1497,(2015)

[7] B.MacMillan, A.R.Sharp, R.L.Armstrong ,Polymer, 40,2471– 2480, (1999)

[8]A.Enotiadis,K.Angjeli, N.Baldino, I.Nicotera ,Small, 8, 3338–3349, (2012)

[9]M.Zachariah, M.Romanini, P.Tripathi,J.Ll.Tamarit, R.Macovez, Phys. Chem. Chem. Phys.,17,16053-16057,(2015)

[10] M.Zachariah, M.Romanini, P.Tripathi, M.Barrio,J.Ll.Tamarit, R.Macovez,J. Phys. Chem. C, 119, 27298-27306, (2015)

[11] SilvinaCerveny,FabienneBarroso-Bujans, Angel Alegrıa,and Juan Colmenero,J. Phys. Chem. C 114, 2604–2612,(2010)

CONCLUSIONS

In this thesis dielectric spectroscopy is used to investigate the dynamic behaviour of molecules from completely disordered system to low-disorder system. One of the main goals of the thesis is elucidating possible dimensionality effects in low-dimensional structuressuch as thin films and organic molecules intercalated between parallel graphite oxide layers, in order to study differences in the interfacial properties of materials with respect to bulk samples. Dielectric spectroscopy is a powerful tool to investigate how a particular molecular system behaves dynamically at distinct temperatures and frequencies, as well as to study conduction properties.

The thin-film form of materials is an interesting topicfor fundamental research, and is moreover required for various applications. To study materials in film form, we implemented silicon-based interdigital electrode devices which carry two set ofplanar comb like fingers (having opposite polarity during the experiments) working as equivalent capacitor plates to measure dielectric properties of thin films. For this purpose, calibration of the devices is a crucial step, which was performed by using glycerol as reference material.

We studied both organic and hybrid organic-inorganic films, and compared the results with those that we obtained on their bulk counterpart. We analyse rhodamine films deposited by two different procedures starting from rhodamine 6G chloride powder. The first strategy consisted in dissolving the powder in alcohol to achieve solution-deposited films by immobilization; the second strategy was vapour deposition in vacuum. The first films are ionic and ordered, while vacuum-deposited films actually consists of a different,neutral molecule (rhodamine19) due to decomposition of rhodamine 6G chloride upon sublimation. Both types of films display variable-range hopping electronic charge transport, and a conductivity-induced space-charge relaxation which fullfills the Barton–Nakajima–Namikawa (BNN) condition.

In addition, solution deposited rhodamine 6G chloride films display a dipolar relaxation, likely associated to the relatively fast dynamics of an intramolecular dipole moment associated with thecharged molecular nitrogen and the chlorine counter-ion, and which is also present in the polycrystalline powder measured by sandwiching it between two metallic plates.

We also performed studies on film of cadmium iodide covalently attached to ethylamine (CdI_2EA). These hybrid films were deposited by the Langmuir-Blodgett process, for which it was necessary to link the CdI_2EA species to a surfactant molecule. The resulting films had thicknesses of 17 to 31nm. The bulk CdI_2EAmaterial has a solid-to-solid transition at 313K, as observed by dielectric spectroscopy and by calorimetry, while in the Langmuir-Blodgett films the same transition was observed 5K higher in temperature. While both films and bulk displayed a space-charge relaxation verifying the BNN condition, as expected in a hybrid material, the films also displayed anotherdielectric relaxation dynamics athigher frequency. We assign suchrelaxation to the re-orientational motion of the constituent molecules, present only in the films either due to their different chemical composition or to their looser structure.

A completely different low-dimensionality effect is studied in the chapter of the thesis dedicated tobiclotymol, an antisepticdrug which is unstable in its amorphous (supercooled liquid and glass) forms.The main objective was to study the crystallization kinetics, which should display characteristic low-dimensional features due to the fact that supercooledbiclotymol crystallizes into a metastable phase made of one-dimensional needle-like crystallites. By applying dielectric spectroscopy,we probe the moleculardynamics, namely the so-called α relaxation,which is the collective motion of molecules whose freezing is directly connected to the glass transition,and a secondary process (β) whichis likely an intramolecularmotion likely affecting an intramolecularhydrogen bond. The crystallization kinetics was studied at four different temperatures in supercooled liquid state. At all temperatures

crystallization follows the Avrami law with an exponent nearly equal to 2, which indeed confirms the low-dimensional character of the crystallites, as it corresponds to constant (time-independent) nucleation rate and one-dimensional growth of the crystallites.

The last two chapters of this thesis deal with two small molecules that are both ethanederivatives (with distinct side groups replacing some of the hydrogen atoms). The two derivatives are tetrachloroethane, where four hydrogens (two on each side of the molecule) are replaced by chlorine atoms, andethanolamine, with a hydroxyl and an amine groups on different carbons.Both molecules displaya rich solid-state phase diagram with both stable and metastable solid phases. Ethanolamine displays hydrogen bonding while chloroethane does not.

We performed dielectric studies on the stable orthorhombic phase of tetrachloroethane, and observed the existence ofthree distinct relaxation processes at different temperature and frequency. These are: a co-operative α relaxation which has a glass transition temperature of 156 K, close to that ofsupercooledliquid tetracloroethane;a β relaxation which is the single-molecule precursor of the α process and followsthe predictions of the so-called Coupling Model;a γ relaxation which has higher activation energy compared tothe αprocess. In order to identify the exact nature of the α and γ processes, we performed molecular dynamics simulationsand found that thephase exhibits two distinct dynamic processes, both involving a reorientational jump to an intermediate state and then a jump to an orientation equivalent to the initial one.The difference between the two processes is that the γ relaxation is a non-cooperative, back and forth dynamicsbetween the ground-state orientation and a non-equilibrium one, while the α relaxation is a cooperativemotion where the intermediate state is close in energy to the initial and final ones.

In theethanolamine case, we have discovered the existence, besides the stable crystallographic phase, also of a metastable solid phase with different crystal

structure. The metastable phase is obtained by cooling rapidly across the liquid-to-solid crystallization transition. By applying dielectric spectroscopy to all three phases,a very prominent relaxation process is observed in all three. The characteristic frequency of this relaxation dynamics is not dramatically affected by the phase changes. We assign this ubiquitousrelaxation to local fluctuations of the dipole moments associated with intramolecular and inter-molecularhydrogen bondsinvolving the hydroxyl and amine groups.Another weak relaxation feature isobserved in both solid phases, which could be assigned due to a conductivity space-charge effect.

In order to studypossible confinement effects on the hydrogen-bond dynamics of the ethanolamine molecules, we intercalatedthem between graphite oxide sheets. By dielectric spectroscopywe observed a broad relaxation feature whose frequency position was comparable to that of bulk ethanolamine. The relaxation was slower in the two-dimensional material intercalated inside graphite oxide, which we interpret as a confinement or interfacial effect on the dipolar fluctuation of the hydrogen-bond network.

Complementary experiments (with different techniques than dielectric spectroscopy) are required to reach a full understanding of the dielectric processin this simple molecule.

LIST OF PUBLICATIONS

- Pragya Tripathi, Javier Gonzalo-Ruiz, Efstratia Mitsari, Manesh Zachariah, Michela Romanini, Josep Lluis Tamarit, F. Xavier Muñoz, and Roberto Macovez Silicon-Chip-Based Dielectric Spectroscopy for Conductivity and Molecular Dynamics Studies of Organic Films , J. Phys. Chem. Lett., 5, 2796 − 2801,(2014)

- Pragya Tripathi, Michela Romanini, Josep LluisTamarit, Roberto Macovez, Collective relaxation dynamics and crystallization kinetics of the amorphous Biclotymol antiseptic International Journal of Pharmaceutics,495,420–427,(2015)

- P.Tripathi, E.Mitsari, M.Romanini, P.Serra, J.Ll.Tamarit, M. Zuriaga, and R. Macovez, Orientational relaxations in solid (1,1,2,2) tetrachloroethane, J. Chem. Phys.,144,164505,(2016)

ACKNOWLEDGEMENT

Firstly and more sincerely I would like to thank to my Supervisor Dr. Roberto Macovez whose scientific guidance and fruitful discussions helped me to acquire fundamental research ability and extent my knowledge towards this interesting subject. His continuous support and motivation always promotes me to keep on going. He gave insightful suggestions and kind guidance over many occasions. I am grateful for sharing his time in plenty of interesting and inspiring discussions, allow me to benefit from his broad experience and knowledge.

It's an honor to Thanks to Professor Dr. Josep Lluis Tamarit who gives me an opportunity to make a part of GCM group and also for teaching fundamentals of thermodynamics.

Thanks to Professor Dr. Maria Barrio for her valuable knowledge on X-Ray Diffraction experiments and love.

Certainly I would like to thank to my Parents for incredible believe and unconditional love. Without their support this thesis and all my accomplishments in life would not be possible. Thanks to Sunny, Sona and Anshu who always stand by my side in my hard times.

Lastly I would like to thank to all my friends of India who has been watching my journey from far away and friends of Barcelona with whom I shared beautiful moments.

Thanks to every person who has been a part of this fascinating experience.

Thanks

PRAGYA TRIPATHI